Search for Weakly-interacting Long-lived Particles in Proton-Proton Collisions at $\sqrt{s} = 7$ TeV with the ATLAS Detector

Daniel Wayne Ventura

A dissertation submitted in partial fulfillment of
the requirements for the degree of

Doctor of Philosophy

University of Washington

2012

Reading Committee:

Henry Lubatti, Chair

Gordon Watts

Matthew Strassler

Program Authorized to Offer Degree:
Physics

University of Washington

Abstract

Search for Weakly-interacting Long-lived Particles in Proton-Proton Collisions at $\sqrt{s}$ = 7 TeV with the ATLAS Detector

Daniel Wayne Ventura

Chair of the Supervisory Committee:
Professor Henry Lubatti
Physics

A search for the decay of a light Higgs boson to a pair of weakly-interacting, long-lived particles in 1.94 fb^{-1} of proton-proton collisions at $\sqrt{(}s)$ = 7 TeV recorded in 2011 by the ATLAS detector is presented. The strategy requires that one of the long-lived particles decay inside the muon spectrometer. The second long-lived particle is required to decay after the pixel detector in the inner detector and before the middle plane of the muon spectrometer. No excess of events is observed above the expected background and limits on the Higgs boson production and branching ratio to weakly-interacting, long-lived particles are derived as a function of the particle proper decay length.

TABLE OF CONTENTS

Page

List of Figures iii

List of Tables xii

Introduction 1

Chapter 1: Theoretical Background 3
- 1.1 The Standard Model 3
- 1.2 Hidden Valley Models 9
- 1.3 Proton-Proton Collisions 11

Chapter 2: Experimental Apparatus 16
- 2.1 The Large Hadron Collider 16
- 2.2 The ATLAS Detector 19
- 2.3 Inner Detector 22
- 2.4 Calorimetry 24
- 2.5 Muon Spectrometer 27
- 2.6 Luminosity Detectors 33
- 2.7 Trigger System 35

Chapter 3: Reconstruction 38
- 3.1 Track Reconstruction 38
- 3.2 Primary Vertex Reconstruction 39
- 3.3 Photon Reconstruction 40
- 3.4 Electron Reconstruction 41
- 3.5 Muon Reconstruction 42
- 3.6 Jet Reconstruction 43
- 3.7 τ-lepton Reconstruction 46
- 3.8 Missing Energy 46
- 3.9 Luminosity Measurement 47

Chapter 4: Simulation of Hidden Valley Signal Samples 50
4.1 Note on the PYTHIA Simulation 52
4.2 Detector Simulation 54

Chapter 5: Signatures of Displaced Decays and Dedicated Trigger Algorithms 55
5.1 Decays in the Muon Spectrometer 56
5.2 Decays in the Hadronic Calorimeter 69
5.3 Decays in the Inner Detector and Electromagnetic Calorimeter 78
5.4 Expected Number of Triggered Events 83

Chapter 6: Vertex Finding in the Muon Spectrometer 85
6.1 Hadrons and Photons in the Muon Spectrometer 85
6.2 Hidden Valley Decays in the Muon Spectrometer 87
6.3 Track Finding and Momentum Reconstruction 90
6.4 Vertex Finding 100
6.5 Good Vertex Criteria 110
6.6 Data Monte Carlo Scale Factor 114
6.7 Vertex Finding Efficiency and Expected Number of Events 121

Chapter 7: Analysis 124
7.1 Overlapping Signatures 124
7.2 Two Vertices in the Muon Spectrometer 125
7.3 Events that have a Jet with No Reconstructed Tracks 130

Chapter 8: Results and Conclusion 139

Bibliography 141

LIST OF FIGURES

Figure Number — Page

1.1 The three generations of matter and the gauge bosons 4
1.2 Four production mechanisms for the Higgs boson. 12
1.3 Next-to-leading order parton distribution functions for a momentum transfer of 10 GeV^2 (Left) and 10,000 GeV^2 (Right) [15]. 13
1.4 Feynman diagram of a proton-proton collision resulting in a hard scattering producing a Z-boson and Initial State Radiation. 13
1.5 The general structure of a proton-proton collision, showing the hard scatter in the blue circle and the Underlying Event (UE) in the yellow circle. A complex web of gluons can be seen connecting the partons is shown. 14

2.1 The CERN accelerator complex. 17
2.2 Schematic of the LHC ring showing the four interaction points. 18
2.3 Three dimensional view of the ATLAS detector. 19
2.4 Interactions of several typical particles with the ATLAS detector subsystems. . . . 21
2.5 The ATLAS Inner Detector. 22
2.6 The ATLAS calorimeters. 24
2.7 The layout of an electromagnetic calorimeter module. The granularity in each of the three layers is shown. 25
2.8 Profile of the ATLAS muon spectrometer. The barrel MDT chambers are shown in light blue, the endcap MDT chambers are dark blue. In both the barrel and endcap, the trigger chambers are shown in purple. 27
2.9 Left: The field integral, $\int B dl$, from the innermost to the outermost MDT layer in one octant of the MS, as a function of the pseudorapidity. Right: Magnetic field map in the transition region between the barrel and endcap. The coordinate system is rotated by $\phi = \frac{\pi}{8}$ with respect to the ATLAS coordinate system. 28
2.10 The amount of material in units of radiation lengths (X_0) traversed by muons after passing through the calorimeters, as a function of η and ϕ. Some of the more distinctive features include the barrel toroid at $\phi = 22.5^\circ$ and the endcap toroid at $\phi = 0^\circ$ and 45° for $|\eta| \geq 1.4$. 29
2.11 The ATLAS muon spectrometer. The barrel MDT chambers are shown in light blue, the endcap MDT chambers are dark blue. The RPC chambers are shown in purple. 30

2.12 A muon traversing a BIS chamber. The drift circles are shown in light purple and the muon is shown as the dark purple line. 31

2.13 TGC structure showing the anode wires, graphite cathodes, G-10 layers and a pick-up strip, orthogonal to the wires. 34

2.14 The schema of the Level 1 muon trigger. The RPC/TGC are arranged in three stations (RPC1,RPC2 and RPC3 or TGC1, TGC2 and TGC3). The low p_{T} trigger uses RPC1 and RPC2 in the barrel and TGC3 and TGC2 in the endcap. The high p_{T} trigger uses all three stations: RPC1,RPC2 and RPC3 in the barrel or TGC1,TGC2 and TGC3 in the endcap. 36

4.1 Higgs decay to Hidden Valley π_v. 50

4.2 Left: The p_z of the Higgs boson in the signal Monte Carlos. Right: The p_{T} of the Higgs boson in the signal Monte Carlos. 51

4.3 $\Delta\phi$ between the two π_v's in each of the four signal Monte Carlos. 52

4.4 Left: The β of π_v's produced in the barrel region, $\mid \eta \mid < 1$. Right: The β of π_v's produced in the endcap region, $1 < \mid \eta \mid < 2.5$. 52

4.5 Left: The boost, γ, of π_v's produced in the barrel region, $\mid \eta \mid < 1$. Right: The boost, γ, of π_v's produced in the endcap region, $1 < \mid \eta \mid < 2.5$. 53

4.6 Charged hadron (Left) and π^0 (Right) multiplicity in π_v decays to $b\bar{b}$ pairs. Only those particles with $p_{\mathrm{T}} \geq$1GeV are counted. 53

4.7 p_{T} distribution of MC truth charged particles from π_v decays 54

5.1 Probability for a π_v to decay in each of the detector regions as a function of the π_v proper lifetime for each of the four signal monte carlos. Top Left: m_h = 120 GeV, m_{π_v} = 20 GeV, Top Right: m_h = 120 GeV, m_{π_v} = 40 GeV, Bottom Left: m_h = 140 GeV, m_{π_v} = 20 GeV, Bottom Right:m_h = 140 GeV, m_{π_v} = 40 GeV 56

5.2 Event display from Monte Carlo showing a π_v decay in the barrel muon spectrometer. Reconstructed inner detector tracks are shown in black, energy deposits in the hadronic calorimeter are shown in red and energy in the electromagnetic calorimeter are shown in green. MDT hits are shown as blue points, and the location of the Level 1 muon RoI's are shown by the blue bars located outside the spectrometer. . 57

5.3 The total number of RoI's found in events with a π_v decaying inside the barrel muon spectrometer. 58

5.4 Average number of Level 1 muon RoI's in cone of ΔR = 0.4 around the π_v line of flight as a function of the π_v radial decay distance. 59

5.5 Fraction of RoI Clusters accepted in signal events as a function of ΔR between the center of the RoI Cluster and jets (Left) and tracks (Right). 59

5.6 Schematic diagram of the Hidden Valley Muon RoI Cluster trigger. The ovals and diamonds represent the Feature Extraction and Hypothesis algorithms, respectively. 60

5.7 The Δt for a π_v decaying in the muon spectrometer as a function of the π_v proper lifetime for each of the four signal Monte Carlos. Top Left: m_h = 120 GeV, m_{π_v} = 20 GeV, Top Right: m_h = 120 GeV, m_{π_v} = 40 GeV, Bottom Left: m_h = 140 GeV, m_{π_v} = 20 GeV, Bottom Right:m_h = 140 GeV, m_{π_v} = 40 GeV 62

5.8 Efficiency of correctly associating the low p_T muon trigger with the correct bunch crossing as a function of the signal delay; one unit of time shift corresponds to 3.125 ns (From [54]). 63

5.9 Probability that π_v's decaying in the muon spectrometer produce a trigger associated with the correct bunch crossing as a function of the π_v proper lifetime. 64

5.10 The fraction of π_v's which result in jets traversing two adjacent sectors (measured at the trigger plane) of the muon spectrometer, as a function of the π_v radial decay position. 64

5.11 Efficiency for the Muon RoI Cluster trigger as a function of the π_v decay position, for decays in the barrel ($| \eta | < 1$) 65

5.12 Location, in (η,ϕ), of the RoI Cluster for all RoI Clusters in 1.94 fb^{-1} of 2011 Data. 66

5.13 The number of Level 1 muon RoI's, from punch-through jets, contained in the Muon RoI Cluster for both Data and Monte Carlo. 67

5.14 E_T distribution for Level 2 jets at the EM-scale. 68

5.15 The number of jets, found by Level 2 jet reconstruction, with $E_T > 35$ GeV and $| \eta | < 1.7$. Jets with $| \eta | > 1.7$ are beyond the range in which jets could spoil the isolation requirements of the RoI Cluster trigger. 69

5.16 Event display of a showing typical signatures of a π_v decaying inside the barrel hadronic calorimeter. Energy deposits in the hadronic calorimeter are shown in red and energy in the electromagnetic calorimeter are shown in green. Right: Longitudinal view, Left: Transverse view 70

5.17 Lego plot of the energy deposition in the calorimeter cells around the jet axis (0,0,0) for π_v's decaying in the hadronic calorimeter. 71

5.18 Mean value of $\log_{10}(E_{HAD}/E_{EM})$ for all jets in the barrel calorimeter coming from π_v decays as a function of the π_v radial decay distance. 71

5.19 Distribution of $\log_{10}(E_{HAD}/E_{EM})$ for all jets in the barrel region ($| \eta | < 1.4$) inside of Level 1 tau RoI's 72

5.20 Number of tracks reconstructed using the Level 2 tracking algorithm SiTrack with $p_T > 1$ GeV in a region of ($\Delta\eta \times \Delta\phi$) of (0.2×0.2) around the jet axis, for jets with $\log_{10}(E_{HAD}/E_{EM}) \geq 1$ 73

5.21 Schematic diagram of the algorithms used in the Calorimeter Ratio Trigger. The ovals and diamonds represent the Feature Extraction and Hypothesis algorithms, respectively. 73

5.22 The Δt for a π_v decaying in the hadronic calorimeter as a function of the π_v proper lifetime for each of the four signal Monte Carlos. Top Left: m_h = 120 GeV, m_{π_v} = 20 GeV, Top Right: m_h = 120 GeV, m_{π_v} = 40 GeV, Bottom Left: m_h = 140 GeV, m_{π_v} = 20 GeV, Bottom Right:m_h = 140 GeV, m_{π_v} = 40 GeV 74

5.23 Fraction of π_v's that decay in the hadronic calorimeter with a delay of $\Delta t \leq 3$ ns as a function of the π_v proper lifetime 75

5.24 Efficiency for the Calorimeter Ratio trigger as a function of the π_v decay position for decays in the barrel, $|\eta| < 1.4$, (Left) and endcap, $1.4 \leq |\eta| < 2.5$ (Right). . . . 76

5.25 Event display showing a beam halo muon which has bremsstrahlunged inside of the hadronic calorimeter and caused the event to pass the Calorimeter Ratio trigger. The two purple lines are reconstructed muon segments and the yellow boxes represent energy deposited in the hadronic calorimeter. 76

5.26 Calorimeter cell timing for cells traversed by beam halo muons in events that pass the Calorimeter Ratio trigger. Time t=0 ns corresponds to the expected arrival time of a particle produced at the IP during the bunch crossing. 77

5.27 Event displays of two different events with a π_v decaying inside the TRT. TRT drift circles are shown in blue, reconstructed tracks are shown in red, and energy deposits in the electromagnetic calorimeter are shown in green. 79

5.28 Number of reconstructed tracks with $p_T > 1$ GeV associated with each Level 2 jet using the SiTrack tracking algorithm in a $(\Delta\eta \times \Delta\phi)$ region of (0.2×0.2) around the jet axis. 80

5.29 Left: Number of jets present in events where both π_v's decay inside the calorimeter volume. Right: E_T of the jets present in events where both π_v's decay inside the calorimeter volume. 80

5.30 Schematic diagram of the Hidden Valley Trackless Jet plus Muon trigger. The ovals and diamonds represent the Feature Extraction and Hypothesis algorithms, respectively. 82

5.31 Efficiency for the Trackless Jet plus Muon trigger as a function of the π_v decay position for decays in the barrel, $|\eta| < 1.4$, (Left) and endcap, $1.4 < |\eta| < 2.5$, (Right) 82

5.32 p_T of muons produced in the decay of π_v's. 83

5.33 The expected fraction of $h^0 \rightarrow \pi_v\pi_v$ that pass one of the Hidden Valley triggers as a function of the π_v proper lifetime for each of the four signal samples. The Error bands represent the 1 σ uncertainty for the total fraction accepted. Top Left: m_h = 120 GeV, m_{π_v} = 20 GeV, Top Right: m_h = 120 GeV, m_{π_v} = 40 GeV, Bottom Left: m_h = 140 GeV, m_{π_v} = 20 GeV, Bottom Right:m_h = 140 GeV, m_{π_v} = 40 GeV 84

6.1 Event display showing the Monte Carlo truth tracks from a π_v decay in the MS barrel and the simulated MDT hits. 86

6.2 MDT hit multiplicity from single charged pions simulation in the MS barrel. In black, pions that pass through the 3 muon stations. In red, pions that pass through the 3 muon stations plus the magnet coil. 87

6.3 MDT hit multiplicity from single π^0 simulation in the MS barrel. In black, π^0 's that pass through the 3 muon stations in the large sectors. In red, π^0 's that pass through the 3 muon stations in the small sector plus the magnet coil. 88

6.4 Left: Total number of MDT hits per event and Right: Total number of RPC hits per event in signal events where the π_v decays in the barrel region ($\mid \eta \mid \leq 0.8$) 89

6.5 Fraction of MDT hits contained in a cone of size ΔR around the π_v line of flight, as a function of ΔR. 89

6.6 Fraction of MDT hits per multilayer (ML) as a function of ΔR between the center of the MDT chamber and the RoI cluster (η,ϕ) in events with a π_v decaying in the barrel muon spectrometer. 90

6.7 The number of segments reconstructed by Moore (Left) and MuonBoy (Right) in events with a π_v decaying in the muon spectrometer. 91

6.8 χ^2 probability for the reconstructed segments by Moore (Left) and MuonBoy (Right). 91

6.9 Total number of reconstructed single multilayer segments per π_v decay per event . . 92

6.10 Definition of Δb and $\Delta\alpha$ between a pair of segments from the same tracklet in the two MDT multilayers 93

6.11 Left $\Delta\alpha$ and Right Δb, measured in the middle MDT station, for 1 TeV $\pi^{\pm}$ simulated sample. The $\Delta\alpha$ distribution has a width of 4.33 mrad, and the Δb distribution has a width of 1.01 mm. 94

6.12 Δb as a function of the polar angle between the tracklet and the MDT chamber, measured using the $1 < p_{\mathrm{T}} < 3$ GeV $\pi^{\pm}$ sample. 94

6.13 $\Delta\alpha$ projection (Left) and Δb projection (Right) for a simulated sample of $\pi^{\pm}$ with $1 < p_{\mathrm{T}} < 3$ GeV and $\mid \eta \mid \leq 0.8$. The Δb distribution has a width of 1.05 mm. The flat tails in the Δb distribution are due to multiple solutions to the segment finder, giving segments which are randomly oriented with respect to the true tracklet direction. 95

6.14 Δb vs $\Delta\alpha$ from a $\pi^{\pm}$ simulated sample with $1 < p_{\mathrm{T}} < 3$ GeV and $\mid \eta \mid \leq 0.8$, measured inside of the BML chamber 95

6.15 Fraction of segments found with respect to the standard Moore segment finding algorithm. For both algorithms, the segments are required to be made from at least 6 MDT hits and have a χ^2 probability greater than 5%. 96

6.16 Left: bi-dimensional plot of $\Delta\alpha$ vs 1/p from a $\pi^{\pm}$ simulated sample with $1 < p_{\mathrm{T}} < 10$ GeV and $\mid \eta \mid < 0.8$; Right: the profile histogram of $\Delta\alpha$ vs 1/p. The error bars represents the width of the $\Delta\alpha$ distribution for each bin 97

6.17 $\Delta\alpha$ from Toy Monte Carlo (red) compared with the full simulation results for a simulated sample of single pions of p_T = 1.5 GeV (Left) and p_T = 5.5 GeV (Right). 98

6.18 Charge identification efficiency for single pions in the BML chambers vs momentum. 99

6.19 $\Delta\alpha$ vs Δb from signal events for segments in the barrel region ($\mid \eta \mid < 1$) 100

6.20 Left: Total number of reconstructed single chamber tracklets per event. Right: Number of reconstructed tracklets with a momentum measurement for events with a π_v decaying in the barrel spectrometer. 100

6.21 Δb from signal events for segments in the barrel region ($\mid \eta \mid < 1$) that satisfy the criteria $\mid \Delta\alpha \mid < 70$ mrad. 101

6.22 Left: Total number of RPC-phi hits for events with a π_v decay in the barrel and Right: The number of RPC-eta hits for same events 101

6.23 Event displaying showing the MC truth (top) and reconstructed (bottom) tracklets and vertex position for a π_v decaying just beyond the hadronic calorimeter. The reconstructed vertex position is shown by the red circle. 102

6.24 Angular difference between the π_v true line of flight in θ and the reconstructed line of flight in θ. 104

6.25 Angular difference between the π_v true line of flight in ϕ and the reconstructed line of flight in ϕ, for two different methods, average position of the single chamber tracklets (black) and average ϕ of the RPC/TGC hits (red). 104

6.26 Uncertainty in the z-position of tracklets as a function of the extrapolation distance 105

6.27 Left:χ^2 probability for each vertex region. Right:Number of tracklets associated to each vertex region. 106

6.28 Position of the reconstructed vertex relative to the π_v true decay position. Top Left: m_h = 120 GeV, m_{π_v} = 20 GeV, Top Right: m_h = 120 GeV, m_{π_v} = 40 GeV, Bottom Left: m_h = 140 GeV, m_{π_v} = 20 GeV, Bottom Right:m_h = 140 GeV, m_{π_v} = 40 GeV . 106

6.29 Left:Difference between the z-coordinate of the reconstructed vertex and π_v true decay position, for decays in the barrel muon spectrometer. Right:Difference between the R-coordinate of the reconstructed vertex and π_v true decay position. 107

6.30 Position of the found vertices in the ATLAS global coordinate system, (R,z), in π_v Monte Carlo events. Black points show the vertices reconstructed in the barrel and the Red squares show those reconstructed in the endcap. Top Left: m_h = 120 GeV, m_{π_v} = 20 GeV, Top Right: m_h = 120 GeV, m_{π_v} = 40 GeV, Bottom Left: m_h = 140 GeV, m_{π_v} = 20 GeV, Bottom Right:m_h = 140 GeV, m_{π_v} = 40 GeV 108

6.31 Position of the found vertices in the ATLAS global coordinate system, (η,ϕ), in π_v Monte Carlo events. Black points show the vertices reconstructed in the barrel and the Red squares show those reconstructed in the endcap. Top Left: m_h = 120 GeV, m_{π_v} = 20 GeV, Top Right: m_h = 120 GeV, m_{π_v} = 40 GeV, Bottom Left: m_h = 140 GeV, m_{π_v} = 20 GeV, Bottom Right:m_h = 140 GeV, m_{π_v} = 40 GeV 109

6.32 Angular difference between the π_v true line of flight and the reconstructed line of flight. Left: θ line of flight, Right: ϕ line of flight. 110
6.33 Difference between the R-coordinate of the reconstructed vertex and π_v true decay position. 110
6.34 Left: Number of MDT hits in a cone of $\Delta R < 0.6$ around the reconstructed vertex. Right: Number of RPC (or TGC) hits in a cone of $\Delta R < 0.6$ around the reconstructed vertex. 111
6.35 Left: The η position of the reconstructed, good vertices found in data. Right: The ϕ position of the reconstructed, good vertices found in data. 113
6.36 Left: The η position of the reconstructed, good vertices found in each of the four Monte Carlo signal samples. Right: The ϕ position of the reconstructed, good vertices found in each of the four Monte Carlo signal samples. 113
6.37 The position, in RZ, of the reconstructed vertices from 1.94 fb^{-1} of 2011 Data. . . 114
6.38 The total number of MDT hits contained in a cone of $\Delta R = 0.6$, centered around the jet axis, for punch-through jets in Data and QCD Monte Carlo. 115
6.39 Average occupancy of MDT multilayer as a function of ΔR between the center of the MDT chamber and the jet axis for the MC QCD sample and average occupancy of MDT multilayer as a function of ΔR between the center of the MDT chamber and the π_v line of flight. 116
6.40 Distribution of Δb for all combinations of single multilayer segments found in punch-through jets from data (data points) and MC π_v decays in the muon spectrometer (histogram). 116
6.41 The total number of tracks reconstructed by the specialized tracking algorithm. Left: Tracks from punch-through jets. Right: Tracks from signal Monte Carlo with a π_v decay inside the spectrometer. 117
6.42 The total momentum of the reconstructed tracks. Left: Tracks from punch-through jets. Right: Tracks from signal Monte Carlo with a π_v decay inside the spectrometer. 117
6.43 The angle, α, the of the reconstructed tracks in the local chamber reference frame (see Figure 6.10). Left: Tracks from punch-through jets. Right: Tracks from π_v decays in the muon spectrometer. 118
6.44 The scale factor (the ratio of data to Monte Carlo) for the fraction of punch-through jets that produce a vertex in the muon spectrometer. 120
6.45 ΔR between the axis of the punch-through jet and the position of the reconstructed vertex. 120
6.46 Efficiency for reconstructing a vertex for π_v decays in the barrel muon spectrometer for events that pass the RoI Cluster trigger (Left) and events that do not pass the RoI Cluster trigger (Right) as a function of the radial decay position of the π_v. 121
6.47 Efficiency for reconstructing a vertex for a π_v decaying in the endcap muon spectrometer as a function of the z decay position of the π_v. 122

6.48 The expected number of $h^0 \rightarrow \pi_v\pi_v$ that pass one of the Hidden Valley triggers and have a reconstructed vertex in the muon spectrometer as a function of the π_v proper lifetime for each of the four signal samples, assuming a dataset of 1 fb^{-1} . The Error bands represent the 1 σ uncertainty for the number of events. Top Left: m_h = 120 GeV, m_{π_v} = 20 GeV, Top Right: m_h = 120 GeV, m_{π_v} = 40 GeV, Bottom Left: m_h = 140 GeV, m_{π_v} = 20 GeV, Bottom Right:m_h = 140 GeV, m_{π_v} = 40 GeV 123

7.1 Expected number of events with a reconstructed MS vertex and a π_v decay in one of four regions of the detector. Each curve shows the number of events as a function of the π_v's proper lifetime where one π_v is reconstructed as a MS vertex and the second one decays in the inner detector (ID decay), or decays after the tracking system (ECal decay), or decays after the LAr calorimeter (HCal decay) or decays in the muon spectrometer. Top Left: m_h = 120 GeV, m_{π_v} = 20 GeV, Top Right: m_h = 120 GeV, m_{π_v} = 40 GeV, Bottom Left: m_h = 140 GeV, m_{π_v} = 20 GeV, Bottom Right:m_h = 140 GeV, m_{π_v} = 40 GeV 125

7.2 Expected yields for a two-object analysis for each of the four models. Each curve shows the number of events as a function of the π_v's proper lifetime where both π_v's are reconstructed as MS vertices. Top Left: m_h = 120 GeV, m_{π_v} = 20 GeV, Top Right: m_h = 120 GeV, m_{π_v} = 40 GeV, Bottom Left: m_h = 140 GeV, m_{π_v} = 20 GeV, Bottom Right:m_h = 140 GeV, m_{π_v} = 40 GeV 129

7.3 The observed limits for the search for $h^0 \rightarrow \pi_v\pi_v$. The dashed horizontal line represents the 100% branching fraction for this decay channel. Left: Limits for m_{h^0} = 120 GeV. Right: Limits for m_{h^0} = 140 GeV 130

7.4 Fraction of π_v's that produce a jet with $| \eta | < 1$ and zero reconstructed tracks as a function of the π_v radial decay position. 131

7.5 Left: Total missing energy in MC signal events with one π_v decay occurring inside the barrel muon spectrometer and the second π_v decay occurring before the end of the hadronic calorimeter. Right: $\Delta\phi$ between the MET direction and the reconstructed MS vertex position. 132

7.6 Left: The total missing energy in data events with a vertex in the barrel MS. Right: $\Delta\phi$ between the MET direction and the reconstructed MS vertex position. 132

7.7 The efficiency to reconstruct a good MS vertex including the missing energy requirement for π_v's in the barrel ($| \eta | < 1$) region. 133

7.8 The probability that a QCD jet has no reconstructed tracks as a function of the jet p_T, for jets with $| \eta | < 1$. 134

7.9 The ratio of the number of measured to expected events containing a jet with no reconstructed jets for the photon plus jet control sample, as a function of the run number. 135

7.10 Expected yields for a two-object analysis for each of the four models. Each curve shows the number of events as a function of the π_v's proper lifetime where one π_v is reconstructed as an MS vertex and the second π_v is reconstructed as jet with no reconstructed tracks. Top Left: m_h = 120 GeV, m_{π_v} = 20 GeV, Top Right: m_h = 120 GeV, m_{π_v} = 40 GeV, Bottom Left: m_h = 140 GeV, m_{π_v} = 20 GeV, Bottom Right:m_h = 140 GeV, m_{π_v} = 40 GeV 138

7.11 The observed limits for the search for $h^0 \rightarrow \pi_v\pi_v$. The dashed horizontal line represents the 100% branching fraction for this decay channel. Left: Limits for m_{h^0} = 120 GeV. Right: Limits for m_{h^0} = 140 GeV 138

8.1 The observed limits for the search for $h^0 \rightarrow \pi_v\pi_v$. The dashed horizontal line represents 100% branching ratio for this decay channel. Left: The search for a vertex in the MS plus a jet with no reconstructed tracks. Right: The search for two vertices in the muon spectrometer. 139

LIST OF TABLES

Table Number		Page
1.1	The quantum numbers of the quarks and leptons. Note that ν and l represent any of the three generations of leptons, while u and d represent any of the up or down-type quarks, respectively.	7
2.1	The dimensions of the ID subsystems.	22
2.2	The location in R and the space between multilayers for the MDT barrel chambers.	31
4.1	Hidden Valley signal Monte Carlo parameters.	51
6.1	Number of punch-through (PT) jets that have a reconstructed vertex in the muon spectrometer for data and Monte Carlo.	119
6.2	Fraction of punch-through jets that have a reconstructed vertex in the muon spectrometer for each of the MDT selections.	119
7.1	The number of events and probabilities needed to compute the background to events having two vertices in the muon spectrometer.	127
7.2	List of the systematic uncertainties.	128
7.3	Expected number of background events and measured number of events for the two muon vertex channel. The expected background uncertainty contains the full systematic uncertainties.	129
7.4	List of the systematic uncertainties.	137
8.1	The excluded proper decay lengths ($c\tau$), at 95% CL, of the π_v for each of the signal samples, assuming 100% branching ratio for the channel $h^0 \rightarrow \pi_v\pi_v$.	140

ACKNOWLEDGMENTS

I am thankful to all of my professors throughout my academic career for their support and guidance. I would especially like to thank my adviser, Henry Lubatti, for standing by me and guiding me through this PhD. Thanks to the entire Hidden Valley working group, particularly Gordon Watts and Matt Strassler whose advice proved to be invaluable. To Guido Ciapetti, without your ideas and collaboration, the tracking and vertexing would not have worked. To Takashi Nakajima, thank you for showing me the beauty of physics and (unknowingly) setting me down this path.

Thanks to all of my friends for keeping me going and teaching me italian. To *The Dudes*, thank you for your excellence in quizzing and all of the free beer that it brought us.

To my family, thank you for your love, support and encouragement. Without all you, this would not have been possible.

INTRODUCTION

High-energy physics seeks to understand the fundamental constituents from which the universe is built. A particle is referred to as "fundamental" if there is no known substructure to the particle, that is it cannot be understood as a bound state of other particles. All of the known fundamental particles are described within the theoretical construct known as the Standard Model (SM).

The Standard Model describes the interactions of the known fundamental particles through the electromagnetic, weak and strong forces. The electromagnetic force is responsible for the interactions of charged particles and electromagnetic radiation. The weak force is transmitted by the W and Z bosons and is responsible for nuclear β-decay. The strong force is responsible for binding quarks together to form hadrons (protons, neutrons, etc.) and binding protons and neutrons together to form atoms. Through the work of Sheldon Glashow, Steven Weinberg and Abdus Salam, the electromagnetic and weak forces were seen to be two sides of the same electroweak theory. Later, Murray Gell-Mann and George Zweig proposed the quark model to describe the "particle zoo"[1]. This description of the strong interactions, together with the electroweak theory, formed the basis of the Standard Model.

Symmetries of the Standard Model prevent explicit mass terms to be present in the Lagrangian; however, it is experimentally known that particles have mass. The masses of all the fundamental particles can be explained via electroweak symmetry breaking through the Higgs mechanism. The Higgs mechanism predicts the presence of an additional Higgs boson, which has yet to be experimentally observed. Stringent limits have been placed on the allowed Higgs mass range by LEP (for low mass Higgs) and by ATLAS and CMS (for high mass Higgs). Combined, these experiments limit the Standard Model Higgs boson to be in the mass range [115.5, 127 GeV]. However, the presence of new physics can alter the decay of the Higgs boson, severely weakening these constraints. If

[1]The particle zoo refers to the multitude of hadrons which were known to exist in the early 1970's.

the Higgs boson exists, then it can provide a mechanism for producing new particles which are only weakly-coupled to the Standard Model. These new particles can naturally have long lifetimes and travel several meters before decaying to visible (Standard Model) particles. The analysis presented in this thesis searches for events with a Higgs decaying to two long-lived particles, each of which decay within the volume of the ATLAS detector. Novel trigger and reconstruction techniques are developed and employed to identify events with long-lived particles decaying inside of the ATLAS muon spectrometer.

Chapter 1 gives an overview of the Standard Model, the Higgs mechanism and shows that the Higgs boson can be used as a portal to new physics with potentially striking signatures. Chapter 2 describes the Large Hadron Collider and the ATLAS experiment. Chapter 3 discusses the techniques used to reconstruct the data collected during a pp collision. Chapter 4 discusses the simulation of long-lived particles and gives the model parameters used in this search. Chapter 5 describes the new trigger algorithms which were developed to trigger on events with highly displaced vertices in the ATLAS detector. Chapter 6 details the specialized reconstruction techniques which are used to identify vertices from displaced decays inside the ATLAS muon spectrometer. Chapter 7 presents the analyses that are used to search for pair-produced long-lived particles. Finally, Chapter 8 reports the results of the searches and provides limits as a function of the long-lived particle proper lifetime.

Chapter 1

THEORETICAL BACKGROUND

1.1 The Standard Model

There are four fundamental forces: gravity, electromagnetism (EM), the strong force and the weak force. Of these four forces, the latter three are incorporated into a single theoretical framework, the Standard Model (SM). The Standard Model is a relativistic Quantum Field Theory (QFT) based on the gauge group $SU(3)\times SU(2)\times U(1)_Y$. Particles in the Standard Model are divided into two categories: fermions and bosons. The fermions (spin 1/2) comprise the matter in the universe while the gauge bosons (spin 1) mediate the interactions between them.

1.1.1 Quarks and Leptons

Fundamental fermions are divided into two categories: quarks and leptons. There are three known generations, or families, of each. Figure 1.1 shows the three generations of quarks (in purple) and leptons (in green). Each generation of lepton contains one charged particle and its corresponding neutrino. The charged leptons have electric charge -1 (+1) for the (anti)particle while the neutrinos all have zero electric charge. The lightest charged lepton is the electron (e^-), followed by the muon (μ^-) and the tau-lepton (τ^-). There are six flavors of quarks with each generation containing an "up" type quark (q = +2/3) and a "down" type quark (q = -1/3). The up-type quarks are the up (u), charm (c) and top (t) while the down-type quarks are the down (d), strange (s) and bottom (b), for the first, second and third generation, respectively. Both the quarks and charged leptons experience the EM and weak forces and the quarks additionally experience the strong force. The neutrinos do not have electric charge and only experience the weak force.

1.1.2 Quantum Chromodynamics

Quantum Chromodynamics (QCD) [1, 2, 3] is the gauge theory that describes the strong interactions of the quarks and gluons and is the SU(3) component of the SM gauge group. The quarks

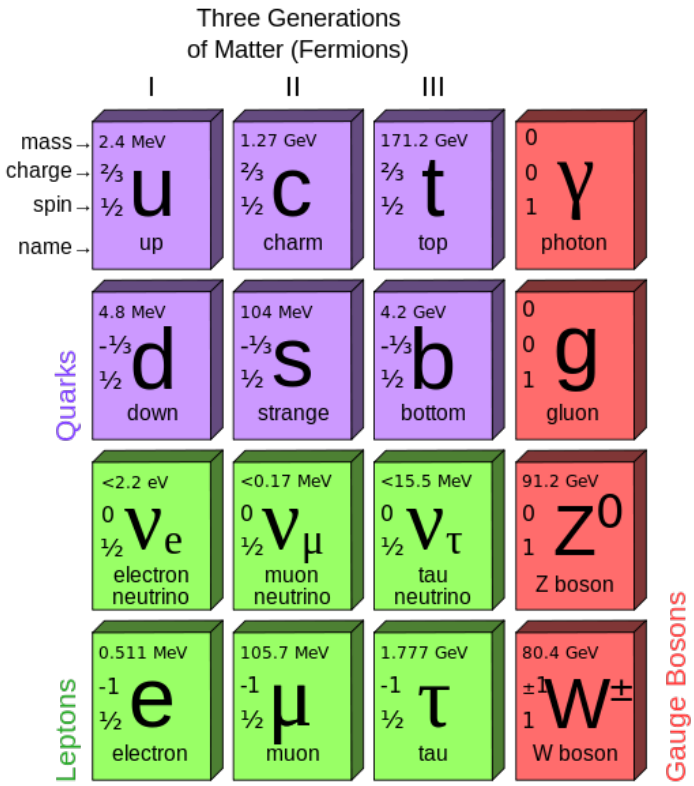

Figure 1.1: The three generations of matter and the gauge bosons

transform as complex three-component vectors according to the fundamental representation of the SU(3) gauge group. Corresponding to this gauge group, there are three color charges, "red", "green" and "blue" and the eight gauge bosons associated with the strong interaction, the massless gluons, carry one unit of color charge and one of anticolor charge. "Rotations" under the SU(3) symmetry, change the quark's color charge. QCD exhibits confinement which prevents isolated color charges from existing and instead requires that all colored objects be grouped into color singlets. The potential between a quark and antiquark can be shown to have a Coulomb part at short distances and a linearly increasing term at long distances [1]:

$$V_{q\bar{q}} \sim \frac{\alpha(r)}{r} + \ldots + \sigma r \tag{1.1}$$

This makes it clear that it is energetically impossible to separate a $q\bar{q}$ pair. Any attempt to separate the quark pair will lead to a large amount of energy being stored in the gluon field and it becomes

energetically favorable to create a second quark-antiquark pair which screen the color charge and minimize the energy stored in the field. This process continues until the energy stored in the gluon fields is not sufficient to create another $q\bar{q}$ pair, at which point all of the quarks are arranged into color neutral bound states. This process of creating hadrons from quarks is referred to as *hadronization* and leads to the creation of several collimated hadrons from the initial quark.

A second important feature of QCD is asymptotic freedom. Because both quarks and gluons carry color charge, they both take part in "vacuum polarization". Vacuum polarization leads to a modification of the effective field seen by the quarks and introduces a dependence on the momentum transfer (Q) between quarks. The presence of virtual quarks increase the coupling strength with increasing Q; however, the gluons decrease the coupling strength with increasing Q. The result is a "running" coupling:

$$\alpha_s(Q) \sim \frac{1}{log(Q/\Lambda_{QCD})} \tag{1.2}$$

where Λ_{QCD} is the momentum scale at which α_s becomes strong as Q^2 is decreased, experimentally, $\Lambda_{QCD} \approx 200$ MeV. Therefore, in interactions with $Q^2 \gg \Lambda^2_{QCD}$, the quarks inside a proton act like free quarks. This implies that in a high energy collision, only a single parton from each proton takes part in the hard scattering process, independent of the other "spectator" partons.

1.1.3 Electroweak Unification

Quantum Electrodynamics (QED) [4, 5] describes the interaction of particles via the exchange of photons. Photons couple to all particles with electric charge with a coupling constant of $g_e = \sqrt{4\pi\alpha}$, where α is the fine structure constant ($\alpha \approx \frac{1}{137}$).

Unlike the other forces, the weak force is mediated by massive gauge bosons, the W and Z. The neutral current involves the Z boson which couples to all particles except the photon (because the Z is neutral) and the gluon (because the Z does not carry color charge). The charged current involves the W boson which couples to every particle except the gluon (because like the Z, the W does not carry color charge). The charged current can change a charged lepton into its neutrino partner or change a quark's flavor from up-type to down-type or vice versa. At leading order, in the Standard

Model, fermions can only change flavor via the charged current as there are no Flavor Changing Neutral Currents (FCNC) allowed.

In the 1960's, Glashow, Wienberg and Salam recognized that electromagnetism and the weak force were two manifestations of the same force, the Electroweak (EW) force [4, 5, 6]. The structural differences between the electromagnetic and weak interactions seems to preclude this unification, with the EM interaction being completely vectoral (γ^μ)[1] while the weak interactions combines vector and axial components ($\gamma^\mu(1-\gamma^5)$)[2]. This difference in the interactions can be resolved by associating the (1-γ^5) matrix with the particle spinor. This results in particles having two "chiral" states: left-handed particles which participate in weak interactions and right-handed particles which do not participate. Organizing the particles in this manner results in the formation of an SU(2) doublet of left-handed particles and an SU(2) singlet for right-handed particles. In order to incorporate the EM interactions, an additional U(1) symmetry is required. Then the full symmetry of the electroweak force is SU(2)×U(1)$_Y$, where the SU(2) refers to "weak isospin" and the U(1) is the "weak hypercharge". A particle's electric charge is related to the particles quantum numbers under the gauge groups by the relation:

$$Q = T_3 + Y \tag{1.3}$$

where T_3 is the third component of the weak isospin and Y is the weak hypercharge. The quantum numbers of the fundamental fermions are listed in Table 1.1. In each generation, the left-handed up- and down-type quarks (or lepton and neutrino) form an isospin doublet, distinguished by T_3. Transformations under the SU(2) symmetry "rotate" up-type quarks into down-type (or leptons into neutrinos). Both the right- and left-handed fermions transform under the U(1) gauge symmetry, which corresponds to local changes in the complex phase of the fermion fields.

If the gauge bosons corresponding to the weak force were massless, then the SU(2)×U(1)$_Y$ would be an exact symmetry of nature; however, it is known that the weak bosons have mass, which implies that this symmetry must be broken by nature.

---

[1] The γ^μ matrices are 4×4 Dirac matrices satisfying the anti-commutation relations $\{\gamma^\mu,\gamma^\nu\} = 2g^{\mu\nu}$, where $g^{\mu\nu}$ is the metric tensor.

[2] $\gamma^5 = i\gamma^0\gamma^1\gamma^2\gamma^3$

Particle	Y	T	T_3	Q
ν_L	-1/2	1/2	1/2	0
l_L^-	-1/2	1/2	-1/2	-1
l_R^-	-1	0	0	-1
u_L	1/6	1/2	1/2	2/3
d_L	1/6	1/2	-1/2	-1/3
u_R	2/3	0	0	2/3
d_R	-1/3	0	0	-1/3

Table 1.1: The quantum numbers of the quarks and leptons. Note that ν and l represent any of the three generations of leptons, while u and d represent any of the up or down-type quarks, respectively.

1.1.4 The Higgs Mechanism

The Englert-Brout-Higgs-Garlnik-Hagen-Kibble mechanism [7, 8, 9], more commonly referred to as the Higgs mechanism, spontaneously breaks the Electroweak ($SU(2)\times U(1)_Y$) symmetry by the introduction of the "Higgs" field, (ϕ). The Higgs field is a doublet under SU(2) and is charged under $U(1)_Y$, which means the component with $T_3 = +1/2$ will have a positive electric charge while the second component is neutral.

$$\phi = \begin{pmatrix} \phi^+ \\ \phi^0 \end{pmatrix} \tag{1.4}$$

The Lagrangian for the Higgs field [4, 5] can be written as:

$$\mathscr{L}_{Higgs} = (D_\mu \phi)^\dagger) D^\mu \phi + \mu^2 \phi^\dagger \phi - \lambda (\phi^\dagger \phi)^2 \tag{1.5}$$

$$D_\mu = \partial_\mu - igA_\mu^a \tau^a - ig' y_\phi B_\mu, \qquad y_\phi = 1/2 \tag{1.6}$$

where A_μ^a and B_μ are the SU(2) and $U(1)_Y$ gauge bosons, respectively.

In order to break the Electroweak symmetry while preserving the $U(1)_{EM}$, the minimum of the potential must not be located at zero, but rather have a Vacuum Expectation Value (VEV) for the

neutral component of the Higgs field of:

$$\phi_v \;=\; \begin{pmatrix} 0 \\ \mu/\sqrt{2\lambda} \end{pmatrix} \;\equiv\; \begin{pmatrix} 0 \\ v/\sqrt{2} \end{pmatrix} \tag{1.7}$$

In the unitary gauge, the Higgs field can be written as the VEV plus the field, h, as:

$$\phi \;=\; \begin{pmatrix} 0 \\ \frac{v}{\sqrt{2}} \end{pmatrix} + \begin{pmatrix} 0 \\ \frac{h}{\sqrt{2}} \end{pmatrix} \tag{1.8}$$

By substituting this form of ϕ into Equation 1.6 and diagonalizing the mass matrix, three massive vector bosons, one massless boson and the Higgs boson are produced. The three massive vector bosons correspond to the $W^{\pm}$ and Z while the massless boson is the photon. The masses of the W and Z can be written in terms of the gauge couplings g of SU(2) and g′ of $U(1)_Y$ and the Higgs VEV, v, as:

$$m_W \;=\; \frac{gv}{2}, \quad m_Z \;=\; \frac{\sqrt{g^2+g'^2}}{2}v \tag{1.9}$$

The Higgs boson mass is given by $m_{h^0} = \sqrt{\lambda/2}v$, where λ is the Higgs self coupling parameter from Equation 1.6. The VEV can be measured experimentally as v≈246 GeV; however, λ is unknown making the Higgs mass a free parameter.

While the vector bosons gain a mass through electroweak symmetry breaking, the fermions acquire mass through Yukawa interactions with the Higgs field. The Yukawa interactions link the right and left-handed fermions with the Higgs field as follows (for the electron):

$$\Delta\mathscr{L}_e \;=\; -\lambda_e \overline{E}_L \cdot \phi e_R \;+\; h.c. \tag{1.10}$$

where the indices of the SU(2) doublets E_L and ϕ are contracted. The new parameter, λ_e, is the dimensionless Yukawa coupling constant. Replacing ϕ in equation 1.10 with the form in equation 1.8:

$$\Delta\mathscr{L}_e \;=\; -\frac{v}{\sqrt{2}}\lambda_e \bar{e}_L e_R \;-\; \frac{1}{\sqrt{2}}\lambda_e \overline{E}_L \cdot h e_R \;+\; h.c. \tag{1.11}$$

The first term in equation 1.11 is the mass term for the electron which has a mass set by the Higgs VEV and scaled by the Yukawa coupling constant:

$$m_e \;=\; \frac{1}{\sqrt{2}}\lambda_e v \tag{1.12}$$

The second term in equation 1.11 allows the Higgs to couple to electrons with a coupling proportional to the electron mass.

1.1.5 The Higgs Boson

While the Higgs mechanism provides an elegant way to break electroweak symmetry and give masses to both the gauge bosons and fundamental fermions alike, to date, no experimental evidence has been found to prove the existence of the Higgs. Combined results from LEP [10], the Tevatron [11, 12] and the LHC [13, 14] have narrowed the allowed mass range for the Higgs boson to 115.5 - 127 GeV at the 95% confidence level. These analyses have been performed assuming a Standard Model like Higgs which has couplings only to the known fermions. Section 1.2.1 shows that the addition of new physics can alter the Higgs decay modes and effectively nullify or weaken the experimental constraints.

1.2 Hidden Valley Models

A number of extensions to the Standard Model (SM) predict particles that are neutral, weakly-interacting and have long decay lengths. These long-lived particles occur in many models: gauge-mediated Supersymmetry (SUSY) extensions of the Minimal Supersymmetric Standard Model (MSSM) [17], MSSM with R-parity violation [18], inelastic dark matter [19] and Hidden Valley (HV) scenarios [20, 21, 22]. In order to study the signatures of long-lived particles in the ATLAS detector, a hidden valley scenario has been chosen. The HV scenario provides a generic class of models containing long-lived particles, and serves as an excellent benchmark for studying displaced decays.

Hidden Valley models are a general class of models in which a hidden sector ("v-sector") is added to the Standard Model. All of the SM particles are neutral under the v-sector gauge group and likewise, the v-sector particles ("v-particles") are neutral under the SM gauge group. Therefore, SM and v-particles can only interact through "communicator particles" which can be any neutral particle or combination of particles which are charged under both the SM and the v-sector gauge group. Experimental constraints, such as electroweak precision measurements [23], require that the communicator particles be as of yet undiscovered in order for v-particles to be produced in abundance at the LHC.

The v-sector can be any field theory which leads to multiparticle production; however, only those models in which the new v-particles decay back to SM particles with reasonable branching fractions and lifetimes are experimentally interesting. Because the v-particles do not couple directly to the SM, the decay of the v-particles must occur via one of the communicator particles, which depending on the mass of the communicator and its couplings, can result in long lifetimes for the lightest v-particles.

1.2.1 Higgs decay to Two Long-lived Particles

The Higgs may serve as a window into the v-sector as it may produced in abundance at the LHC and can have substantial branching fraction to v-particles [21]. A light Higgs boson has a small width, due to the small Yukawa coupling to the b-quark. Its decays can easily be altered by the addition of a new interaction, which can add a new decay mode with a large branching fraction. These new decay modes can naturally arise with a branching fraction between a few percent up to 100%, thus reducing the branching fractions to the SM particles ($\gamma\gamma$, $b\bar{b}$, etc). This can significantly impact the searches for a SM-like Higgs and allow for such a particle to exist within the mass regions which have been excluded by the traditional analyses [24].

In order to study HV events, a QCD-like v-sector consisting of a confining gauge group, a U(1) and scalar field ϕ is chosen, consistent with the model presented in [20]. The U(1) is spontaneously broken by ϕ acquiring a non-zero VEV (similar to the Higgs mechanism). This yields a Z$'$ with mass of a few TeV and gives masses to the fundamental v-fermions.

The SM and v-sector can then communicate either through the Z$'$ or via mixing between the Higgs and ϕ [20, 21]. This Higgs mixing gives rise to the Higgs decay mode h$\rightarrow Q_v\overline{Q}_v$, where the Q_v are v-quarks. The Q_v then hadronize according to the dynamics of the v-sector, producing v-hadrons. For a low mass Higgs, this hadronization process typically yields two v-pions ("π_v's"), the v-sector equivalent of the SM pion.

Once produced, the π_v can decay to SM particles by coupling through either the Z$'$ or the Higgs.

In analogy with the SM pion, the pseudoscalar π_v decays predominately to heavy fermions due to helicity suppression. For π_v masses larger than $2m_b$, the π_v branching ratios are $\sim$85:5:2:8 for $b\bar{b}$, $c\bar{c}$, gg and $\tau^+\tau^-$, respectively. Other models where the π_v is replaced by another weakly-interacting, long-lived scalar or pseudoscalar were noted in [21, 25].

Due to the variety of models which predict the Higgs boson decaying to long-lived, weakly-interacting particles, the process $h\rightarrow \pi_v\pi_v$ has been characterized by the physical parameters: m_{h^0}, m_{π_v}, τ_{π_v} and BR($h\rightarrow \pi_v\pi_v$). This characterization decouples the search from the precise choice of the physics in the hidden sector.

1.2.2 Higgs Production

The Higgs boson can be produced in several ways in pp collisions. Figure 1.2 shows the four production modes with the largest cross sections. The largest cross section is gluon fusion, in which two gluons produce a Higgs boson via an intermediate top-quark loop. The other three production mechanisms have much smaller cross sections, typically 1-2 orders of magnitude less than the gluon fusion cross section [26]. Because of the large cross section, it is advantageous to search for Higgses produced via gluon fusion; however, as shown in Chapter 5, this production channel poses challenges to the ATLAS trigger system.

1.3 Proton-Proton Collisions

The collision of any pair of protons is a random event and the resultant interaction cannot be predicted. However, it is possible to know the relative probability for different processes to occur. This is done by calculating the "cross section", σ, for each process of interest. Cross sections are measured in units of barns, b, with 1 b = $10^{-28}m^2$. Most interesting physics process have cross sections on the order of picobarns (pb), 10^{-12} b, while the total proton-proton cross section is $\sim$100 mb. A majority of this cross section comes from elastic scattering, $pp \rightarrow pp$, and "minimum bias" collisions. Minimum bias collisions are those which involve a large enough momentum transfer to create several particles which enter the acceptance region of the detectors, but do not produce any high energy particles.

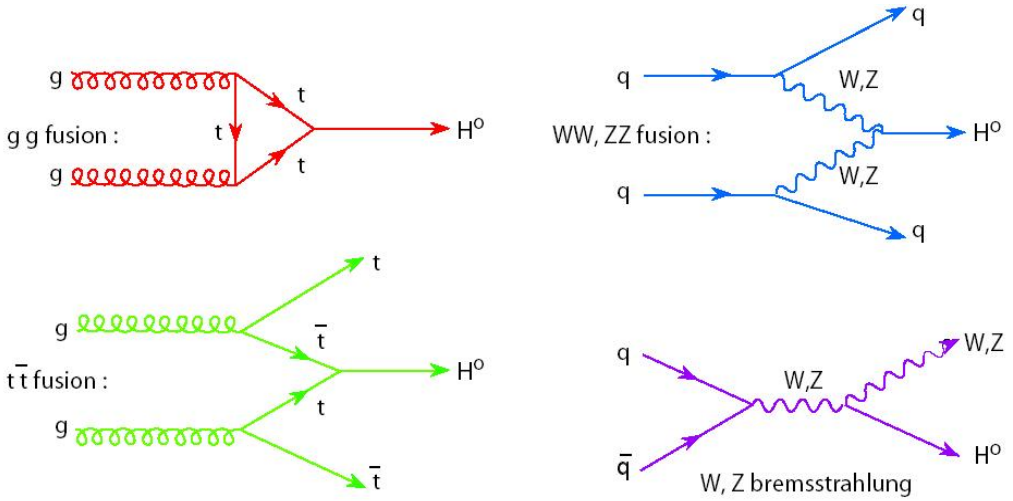

Figure 1.2: Four production mechanisms for the Higgs boson.

1.3.1 Parton Distribution Functions

In "hard"(large Q^2) proton-proton high-energy collisions, the scattering process involves the partonic constituents of the proton. Therefore, to predict the cross-sections for any process, a set of Parton Distribution Functions (PDFs) [15, 16] are required. The PDFs, $f_a(x)$, describe the structure of the proton and give the probability that a parton, a, has a fraction, x, of the proton's total momentum. Figure 1.3 shows two PDFs, at scales of $Q^2 = 10$ GeV^2 and $Q^2 = 10^4$ GeV^2. As can be seen, a non-negligible fraction of the proton's momentum is carried by gluons and virtual ("sea") quarks. Sea quarks are formed when a gluon from the hadron's color field splits to form a quark antiquark pair. These sea quarks typically annihilate each other and produce a gluon; however they still carry a fraction of the proton momentum and can take part in the hard scatter. In order to calculate the physically observable cross section, it is necessary to convolute the PDF with the hard scattering cross section.

1.3.2 Anatomy of a Collision

Figure 1.4 shows a Feynman diagram of a hard scatter event with a Z-boson being produced. However, the hard scatter between two partons is not the only process that occurs during a pp collision. There are many other processes which occur in a pp collision including: hadronization,

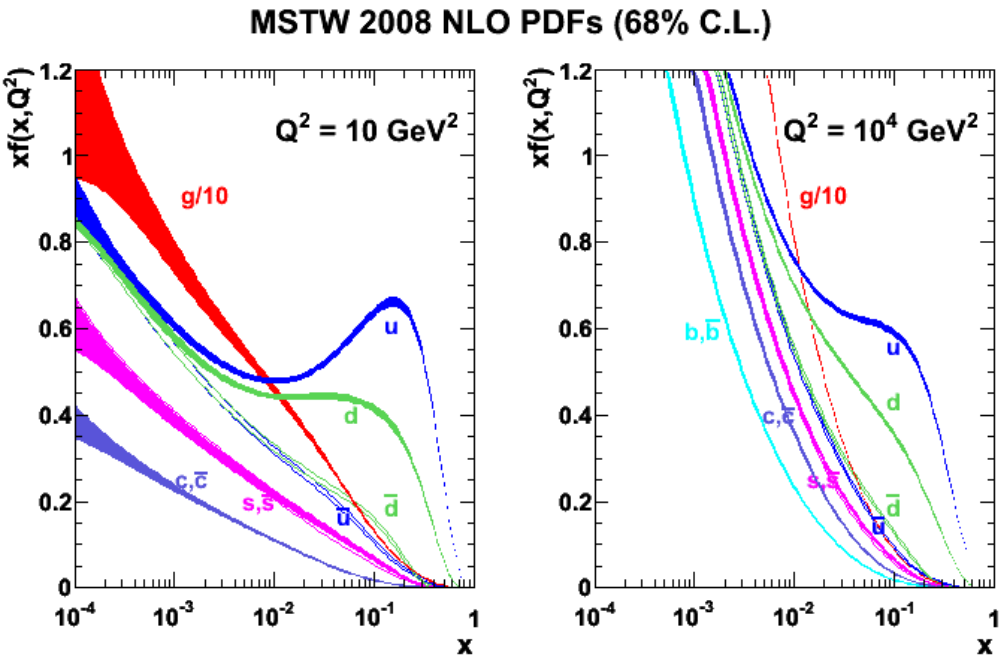

Figure 1.3: Next-to-leading order parton distribution functions for a momentum transfer of 10 GeV^2 (Left) and 10,000 GeV^2 (Right) [15].

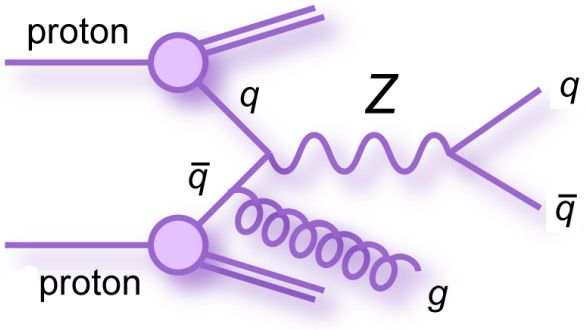

Figure 1.4: Feynman diagram of a proton-proton collision resulting in a hard scattering producing a Z-boson and Initial State Radiation.

Initial and Final State Radiation (ISR and FSR), Multiple Parton Interactions (MPI) and the Under-

lying Event (UE). A more "relatistic" diagram of pp collision is shown in Figure 1.5 [2]. The hard scatter process and subsequent hadronization of colored partons is shown in the blue circle and the underlying event is shown in the yellow circle.

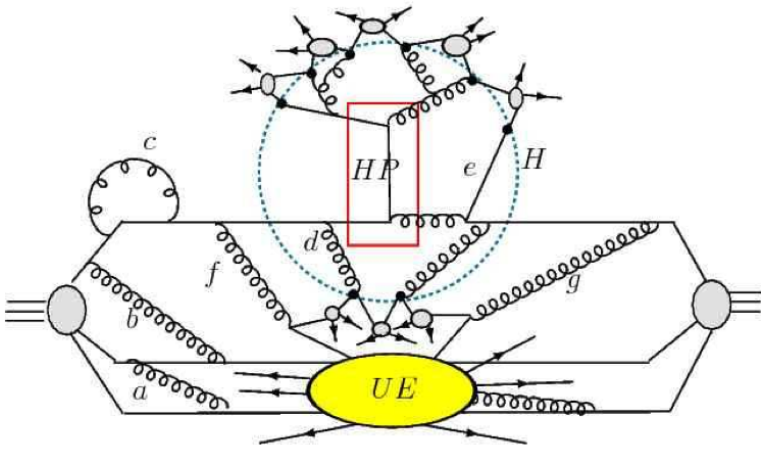

Figure 1.5: The general structure of a proton-proton collision, showing the hard scatter in the blue circle and the Underlying Event (UE) in the yellow circle. A complex web of gluons can be seen connecting the partons is shown.

Hadronization and Jet formation

Quarks and gluons which are produced as a result of the hard scatter (or particle decay) undergo hadronization due to confinement. This is the result of a non-perturbative feature of QCD that does not allow color-charged particles to exist freely. Instead, all color-charged particles are required to form color-neutral bound states. When a parton pair is created, they form a color (gluon) field connecting the partons. As the partons move apart, more energy is stored in the color field until the field has enough energy to create a quark anti-quark pair from the vacuum. The process continues in this fashion until there is not enough energy in the color field to create new quark pairs, and all of the existing quarks are grouped into color neutral hadrons. This hadronization process has the effect of creating a "jet" of hadrons, each travelling in the general direction of the initial parton.

Initial and Final State Radiation

Initial state radiation occurs when a parton radiates either a gluon or photon before participating in the hard scatter, while final state radiation occurs when the final state partons (the products of the hard scatter) radiate either a gluon or photon. Partons are continuously emitting soft, collinear gluon radiation which forms some of the softer particles in the jets. However, a parton can also radiate an energetic gluon, as seen in Figure 1.4, which results in an additional jet being formed.

Multiple Particle Interactions

Multiple particle interactions occur when more than one pair of partons interact during a collision. This generally leads to a collision containing one hard scatter and a second soft scattering event. As a result of the additional soft scatter, the pp collision appears to be a minimum bias event plus the hard scatter.

Underlying Event and Beam Remnant

The underlying event is defined as all of the activity of a single pp collision which is not part of the hard scattering process. When the protons collide, a parton from each proton takes part in the collision and is either annihilated or scattered out of the proton. This means the proton loses a colored constituent and is thus colored itself and a color field is formed surrounding the collision region. As the color field evolves, hadrons are produced and tend to follow the beam.

The beam remnant refers to the portion of the proton which did not take part in the hard scatter. The proton remnants are scattered at small angles with respect to the beam line as the remnant (typically) carries most of the proton momentum.

Chapter 2

EXPERIMENTAL APPARATUS

2.1 The Large Hadron Collider

The Large Hadron Collider (LHC) [27, 28, 29] is a proton-proton collider located at CERN, in the outskirts of Geneva, Switzerland. The LHC was constructed in the same tunnel as the former Large Electron-Positron (LEP) collider, and is $\sim$27 km in circumference and located approximately 100 m underground. The LHC accelerates two counter-rotating beams of protons and collides them head on at four points, each housing one of the LHC experiments, along the ring.

2.1.1 The CERN Accelerator Complex

The CERN accelerator complex (Figure 2.1) is a succession of accelerators culminating in the LHC. Protons are produced using a duoplasmatron to strip the electrons from hydrogen atoms. These protons are then formed into bunches and injected into the LINear ACcelerator (LINAC) where they are accelerated and injected into the Proton Synchrotron booster. Each bunch of protons contains $\sim 1 \times 10^{11}$ protons and is a few centimeters in length. Once in the booster, the protons are accelerated to an energy of 1.4 GeV. From the booster, the protons are transferred to the Proton Synchrotron (PS), where the protons are further accelerated to 25 GeV. From the PS, the protons are injected to the Super Proton Synchrotron (SPS), where the proton beams reach an energy of 450 GeV. Finally, the beam enters the LHC which accelerates the protons to the energy of 3.5 TeV.

2.1.2 The LHC

When completely filled, the LHC is designed to hold up to 2808 proton bunches per beam, with an inter-bunch spacing of 25 ns. During the 2011 data taking period, LHC operated with a larger space between bunches (50 ns spacing instead of 25 ns), which resulted in a maximum of 1380 bunches.

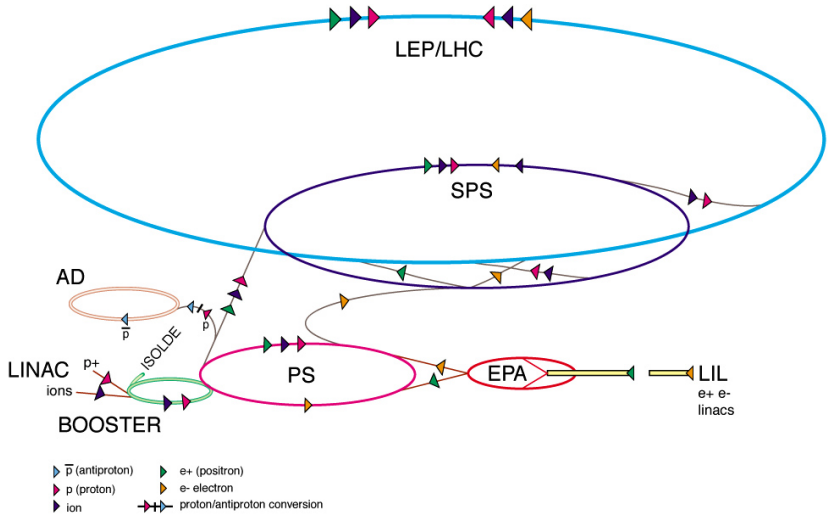

Figure 2.1: The CERN accelerator complex.

The LHC is segmented into eight sectors, each containing a straight section and an arc, as shown in Figure 2.2. The straight sections are approximately 528 m in length and are used for variety of purposes. Collisions occur in the straight sections at Points 1, 2, 5 and 8, where the ATLAS, ALICE, CMS and LHCb experiments are located, respectively. The beam is accelerated using the Radio-Frequency (RF) cavities located in the straight section at Point 4, while Points 3 and 7 contain beam collimation systems which shape and clean the beam. The straight section in Point 6 is used as the beam dump, where the beams are removed from the LHC and ”dumped” into a graphite target to dissipate the beam’s energy.

The arcs are built using a total of 1232 superconducting dipole magnets which keep the beams in the (nearly) circular orbit. Each of the dipole magnets is capable of generating a magnetic field of up to 8 T. Additionally, there are 392 quadrapole magnets, located in the straight sections, which serve to focus the beam.

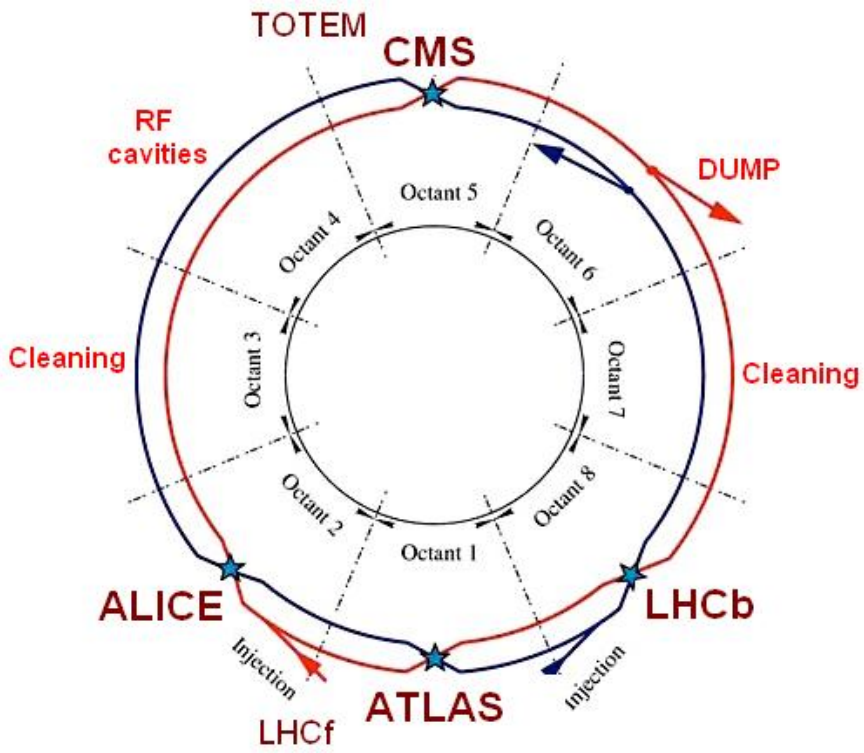

Figure 2.2: Schematic of the LHC ring showing the four interaction points.

2.1.3 Luminosity

The total number of events, N, for a given process is directly proportional to the process cross-section (σ) and the integrated luminosity ($\mathscr{L}$).

$$N = \mathscr{L}\sigma \tag{2.1}$$

The cross-section for a process depends on the center-of-mass energy and the type of particles participating in the collision (e.g. proton-proton or e^+e^-). The luminosity, on the other hand, is dependant upon the properties of the colliding beam and therefore, is time dependant. The instantaneous luminosity (L) [29] can be defined as:

$$L = \frac{N_b^2 n_b f_r \gamma_r}{4\pi\varepsilon_n\beta^*}F \tag{2.2}$$

where N_b is the number of protons per bunch, n_b is the number of colliding bunches, f_r is the rotation frequency, γ_r is the relativistic gamma factor, ε_n is the normalized transverse beam emittance[1], β^* is the beta function[2] at the collision point, and F is a geometric factor which accounts for the beam crossing angles. The instantaneous luminosity is measured in units of $cm^{-2}s^{-1}$.

2.2 The ATLAS Detector

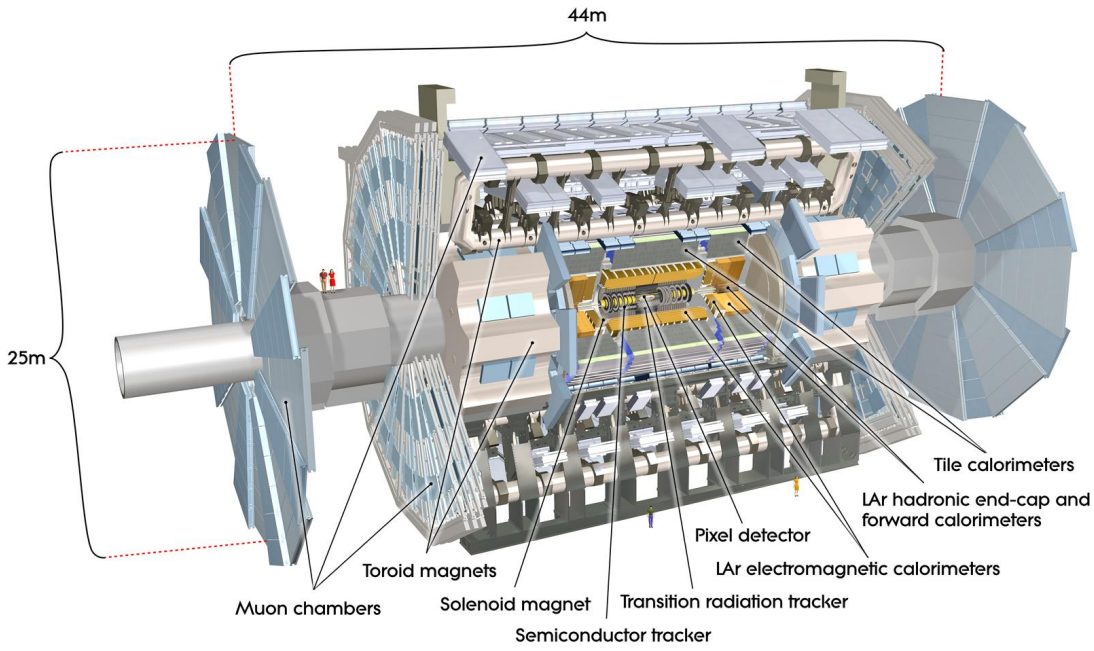

Figure 2.3: Three dimensional view of the ATLAS detector.

2.2.1 ATLAS Overview

ATLAS (A Toroidal LHC ApparatuS) is a multipurpose detector designed to measure particles produced in proton-proton collisions [30, 31]. A cutaway diagram of the detector highlighting all of

[1]The transverse emittance is a measure of the beam size and particle divirgences in the transverse (xy) plane.

[2]The beta function measures how focused the beam is, with small β corresponding to highly focused beam.

the different subsystems is shown in Figure 2.3.

At the center of the detector, closest to the Interaction Point (IP) is the inner detector. The inner detector measures the trajectories of the charged particles created in the pp interactions. The inner detector is immersed in a 2 T magnetic field which is produced by a super conducting solenoidal magnet. The curvature of the particle trajectory is used to measure the particles momentum.

Surrounding the inner detector is the calorimeter. The calorimeter is composed of two pieces, the electromagnetic and hadronic calorimeters. The calorimeters measure the energy of both the charged and neutral particles created from the pp collision.

The muon spectrometer forms the outer shell of ATLAS. The muon spectrometer is designed to measure charged particles, typically muons, which escape the calorimeter. Three toroidal magnets generate an average field of $\sim$0.5 T in the spectrometer.

Figure 2.4 shows how some typical particles interact with the different subsystems of the ATLAS detector. The charged particles are bent by the magnetic field in the ID and are measured by the inner detector. The muon is a minimum ionizing particle and escapes the calorimeters before being measured in the muon spectrometer. The electron and photon both deposit their energy in the electromagnetic calorimeter, while the proton and neutron penetrate the deeper into the calorimeters and deposit energy in the hadronic calorimeter. Neutrinos (or other weakly-interacting particles) escape the detector without interacting and are invisible to the detector.

2.2.2 ATLAS Coordinate System

ATLAS uses a right-handed coordinate system with its origin at the nominal interaction point (IP) in the center of the detector and the z-axis coinciding with the beam pipe. The x-axis points from the IP to the center of the LHC ring, and the y-axis points upward. Cylindrical coordinates (R,ϕ) are used in the transverse plane, with ϕ being the azimuthal angle around the beam pipe. The pseudorapidity

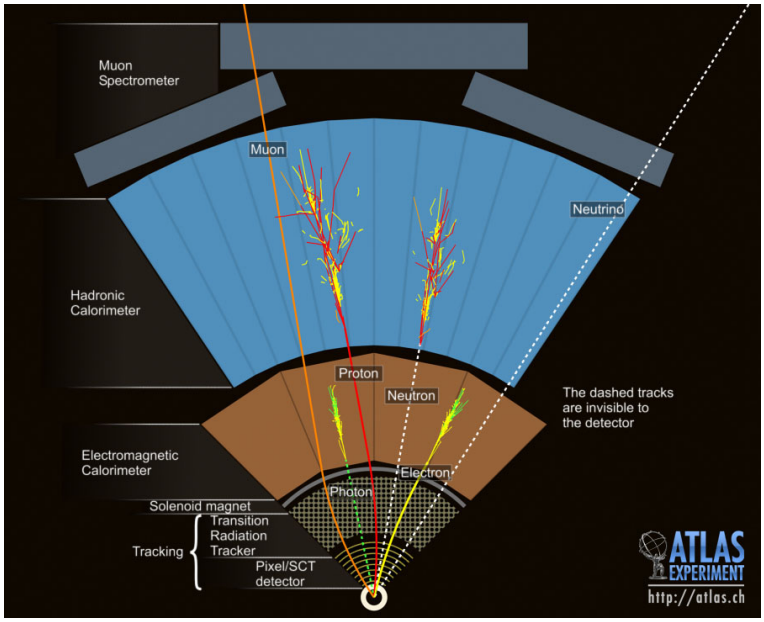

Figure 2.4: Interactions of several typical particles with the ATLAS detector subsystems.

(η) is defined in terms of the polar angle θ as:

$$\eta = \text{-ln}(\tan\frac{\theta}{2}) \tag{2.3}$$

The pseudorapidity is the massless limit of the of the rapidity (y):

$$\text{y} = \frac{1}{2} ln(\frac{E + p_z}{E - p_z}) \tag{2.4}$$

which is invariant under boosts in the z-direction. Most particles which are directly measured have m/|p| $\ll$ 1, therefore, the pseudorapidity is approximately invariant under boosts along the z-axis. The angle between two particles can be measured using η and ϕ as:

$$\Delta R = \sqrt{\Delta\eta^2 + \Delta\phi^2} \tag{2.5}$$

Therefore, ΔR is also approximately invariant under boosts along the z-direction.

ATLAS uses natural units with the speed of light, c, set equal to one. In this unit system, energy, momentum and mass are all measured in GeV. Additionally, particle proper lifetimes, τ, and proper decay lengths, cτ, are both measured in terms of distance.

2.3 Inner Detector

The Inner Detector (ID) covers the region $| \eta | \leq 2.5$ and is immersed in a 2 T solenoidal magnetic field. The ID is comprised of three different tracking technologies: pixel detectors, silicon microstrips (SCT), and a Transition Radiation Tracker (TRT). The general layout of these detector elements is shown in Figure 2.5 and the positions of the barrel and endcap detectors are given in Table 2.1.

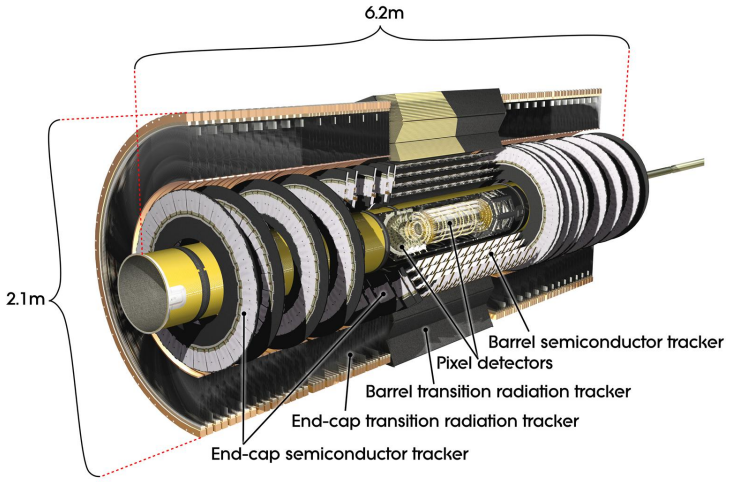

Figure 2.5: The ATLAS Inner Detector.

Detector Element	Radial extension (cm)	Length (cm)
Pixel, barrel	$5.05 < R < 12.25$	$0 < \|z\| < 40.05$
Pixel, endcap	$8.88 < R < 14.96$	$49.5 < \|z\| < 65.0$
SCT, barrel	$29.9 < R < 51.4$	$0 < \|z\| < 74.9$
SCT, endcap	$27.5 < R < 56.0$	$83.9 < \|z\| < 273.5$
TRT, barrel	$56.3 < R < 106.6$	$0 < \|z\| < 71.2$
TRT, endcap	$64.4 < R < 100.4$	$84.8 < \|z\| < 271.0$

Table 2.1: The dimensions of the ID subsystems.

2.3.1 Pixel Detector

The pixel detector consists of three layers arranged in concentric cylinders, in the barrel, and three disks arranged perpendicular to the beam line, in each endcap region. The individual pixels are identical throughout the detector and have a minimum pixel size of 50×400 μm. The elements are arranged such that a charged particle will typically cross three pixel layers, providing a very accurate measurement of the track near the IP.

2.3.2 Semiconductor Tracker

The SemiConductor Tracker (SCT) is comprised of silicon microstrips. In the barrel, the SCT has four tracking layers, each with a set of stereo strips. The stereo strips are arranged with one strip aligned with the z-axis and the other strip offset by 40 mrad. This configuration allows for the measurement of four space points (R,ϕ,z) for a typical charged particle crossing the barrel SCT. In the endcap, there are 9 disks (per endcap), with one set of strips running radially and the stereo pair offset by 40 mrad.

2.3.3 Transition Radiation Tracker

The TRT is constructed of straw-tubes with a diameter of 4 mm. The straws are filled with a Xe-based gas mixture and have a central wire, held at 1560 V, for collecting ionization electrons. The TRT barrel contains up to 73 layers of straws and the endcap contains 160 straw planes. A typical charged particle, which crosses the TRT, will have 36 TRT measurements. The TRT straws are $\sim$71 cm (37 cm) in length in the barrel (endcap), which means that each straw tube can only measure two coordinates: (R,ϕ) in the barrel or (z,ϕ) in the endcap.

In addition to measuring position, the TRT also provides particle identification. Fibers (foils) are interleaved with the straw tubes in the barrel (endcap) which provide transition radiation for electron identification. The transition radiation is identified by the higher amount of charge collected in the straw and are referred to as "high-threshold" hits. A typical electron, with $|\mathrm{p}| \geq 2$ GeV will leave seven to ten high-threshold hits which can be used in conjunction with other (calorimeter based) variables to identify the track as belonging to an electron.

2.4 Calorimetry

A cutaway diagram, showing the ATLAS calorimeters is shown in Figure 2.6. The calorimeter has three parts, the electromagnetic, hadronic and forward calorimeters. The Electromagnetic Calorimeter (ECal) measures the energy of the photons and electrons in the region $|\eta| < 3.2$. The Hadronic Calorimeter (HCal) surrounds the ECal and measures the energy of the hadrons ($\pi^{\pm}$,p,...) and also covers the region $|\eta| < 3.2$. The Forward Calorimeter (FCal) has courser granularity and covers the range $3.1 < |\eta| < 4.9$.

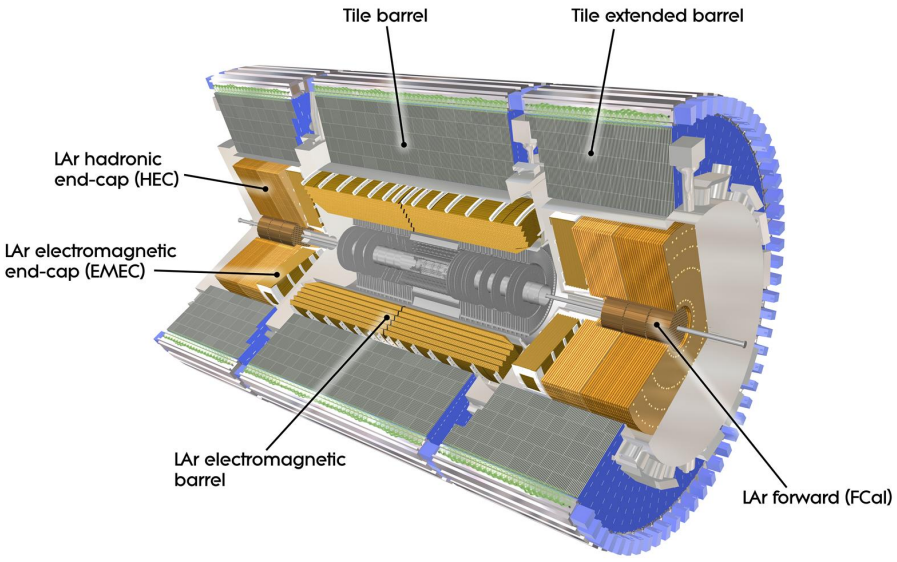

Figure 2.6: The ATLAS calorimeters.

2.4.1 The Electromagnetic Calorimeter

The ECal is divided into the barrel ($|\eta| < 1.475$) and two endcaps ($1.375 < |\eta| < 3.2$). The calorimeter is a lead-liquid argon detector with accordion shaped kapton electrodes and lead absorber plates, as shown in Figure 2.7. The accordion geometry provides complete ϕ symmetry without azimuthal cracks. The thickness of the lead absorber plates varies as a function of η, keeping the average number radiation lengths constant, in order to optimize the energy resolution. In the

region devoted to precision physics, $|\eta| < 2.5$, the calorimeter is segmented into three longitudinal layers. The first of these layers has fine granularity to accurately measure the position of photons and electrons. In the endcap, the calorimeter is segmented into two longitudinal layers and has a coarser granularity than the central region.

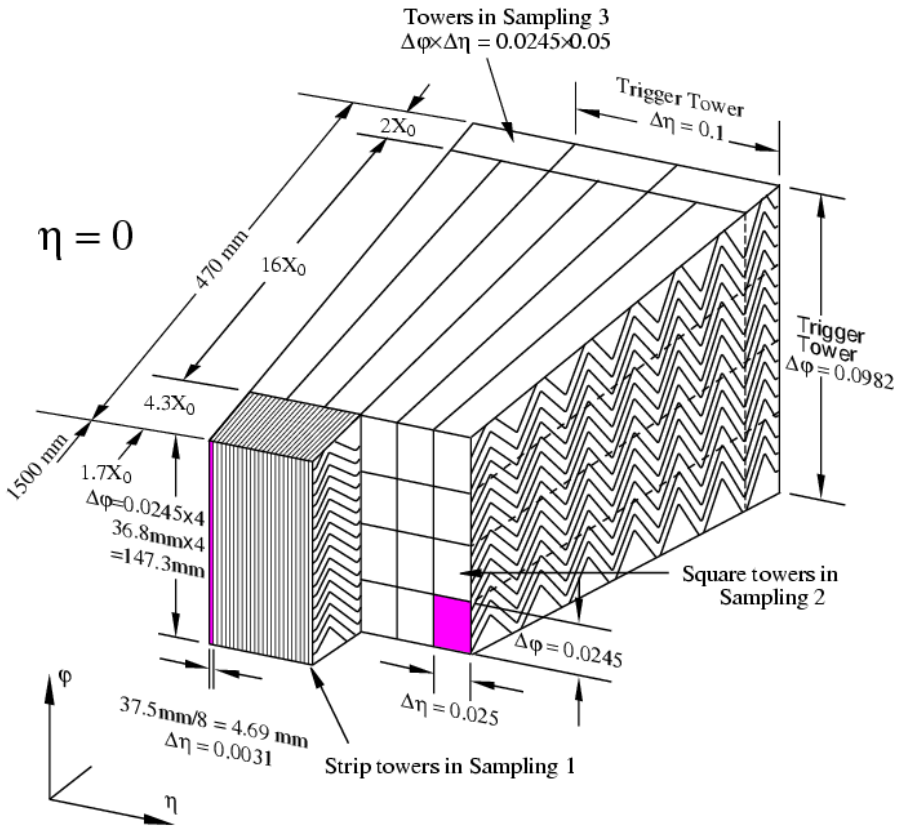

Figure 2.7: The layout of an electromagnetic calorimeter module. The granularity in each of the three layers is shown.

In total, the ECal contains more than 24 (26) radiation lengths (X_0)[3] in the barrel (endcap) regions. In the barrel, the material in the ECal amounts to more than 2.3 hadronic interaction lengths

[3]A radiation length is the mean distance over which a high-energy electron loses all but 1/*e* of its energy.

(λ)[4], which implies that hadrons will start to shower inside the ECal. Thus, the ECal measures all energy from all types of particles (except neutrinos) and low energy hadrons may not completely penetrate the ECal and thereby leave little or no energy in HCal.

2.4.2 The Hadronic Calorimeter

The HCal is comprised of two separate technologies: the tile calorimeter and the hadronic endcap calorimeter.

The Tile Calorimeter

In the barrel, the HCal is constructed using scintillating tiles interleaved with iron absorber. The barrel HCal is placed directly outside the ECal, as shown in Figure 2.6. The barrel region covers $|\eta| < 1$ and the two extended barrels cover the range $0.8 < |\eta| < 1.7$. Radially, the calorimeter extends from 2.28 m to 4.25 m and is longitudinally segmented into three sampling layers. Each sampling layer has a granularity of 0.1×0.1 in $\Delta\eta \times \Delta\phi$. When combined with the ECal, there are a total of 11 λ at $\eta = 0$.

The Hadronic Endcap Calorimeter

The Hadronic Endcap Calorimeter (HEC) consists of two wheels per endcap and is located behind the endcap ECal. The HEC extends from $|\eta| = 1.5$ to $|\eta| = 3.2$. The wheels are constructed from copper plates with liquid argon (LAr) as the sensitive medium. Each wheel is divided into two longitudinal segments which yields a total of four sampling layers per endcap. The HEC granularity is $\Delta\eta \times \Delta\phi = 0.1 \times 0.1$ for $|\eta| < 2.5$ and 0.2×0.2 for $2.5 < |\eta| < 3.2$.

2.4.3 The Forward Calorimeter

The FCal covers the region from $|\eta| = 3.1$ to 4.9 and is comprised of three modules using LAr as the sensitive medium. The innermost module uses a copper absorber and is optimized for electromagnetic measurements. The outer two modules use a tungsten absorber and are designed to

[4] A hadronic interaction length is the mean distance travelled by a hadron before undergoing an inelastic hadronic interaction.

measure the energy from hadronic interactions.

2.5 Muon Spectrometer

The Muon Spectrometer (MS) forms the outermost portion of ATLAS and is designed to measure charged particles which escape the calorimeters. The MS provides momentum measurements for $|\eta| \leq 2.7$ and provides trigger capability out to $|\eta| \leq 2.4$. The precision tracking measurements are made by the Monitored Drift Tubes (MDT's) and Cathode Strip Chambers (CSC's) and the trigger system is comprised of Resistive Plate Chambers (RPC's) and Thin Gap Chambers (TGC's). The spectrometer consists of two portions: the barrel and the endcap, as shown in Figure 2.8. In the barrel, the chambers are arranged in three concentric cylinders, or stations, located at radii of R$\sim$5 m, 7.5 m, and 10 m. In the endcap, the chambers form three wheels with their faces perpendicular to the z-axis and are located at |z|$\sim$7.4 m, 14 m, and 21.5 m.

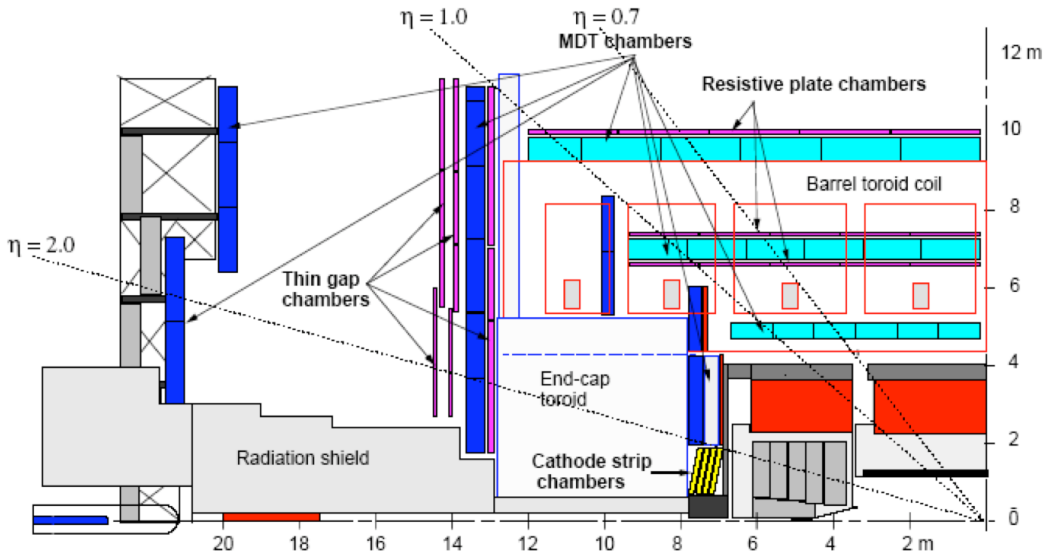

Figure 2.8: Profile of the ATLAS muon spectrometer. The barrel MDT chambers are shown in light blue, the endcap MDT chambers are dark blue. In both the barrel and endcap, the trigger chambers are shown in purple.

A system of three superconducting toroids (one barrel toroid and two endcap toroids) provide the magnetic field for the muon spectrometer. The barrel toroid is 25 m in length along the z-axis,

and extends from R = 4.7 m to 10 m in radius. The two endcap toroids are inserted into the barrel toroid and are 5 m in length. The endcap toroids have an inner bore of 1.65 m and an outer diameter of 10.7 m. The resulting magnetic field is shown in Figure 2.9 as a function of η (Left) and in the transition region as a function of ϕ (Right).

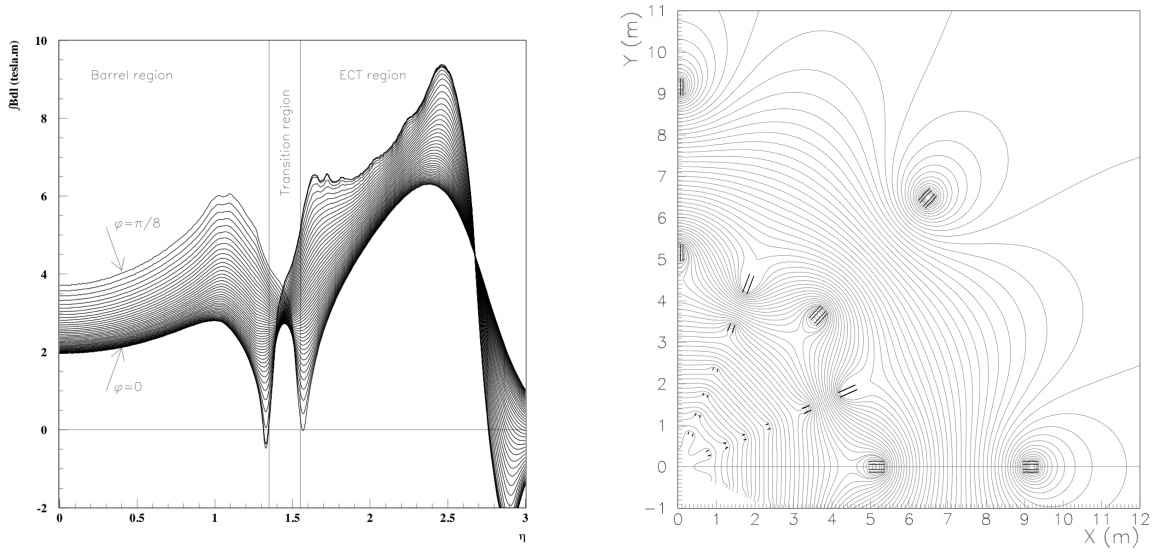

Figure 2.9: Left: The field integral, $\int \mathrm{B}dl$, from the innermost to the outermost MDT layer in one octant of the MS, as a function of the pseudorapidity. Right: Magnetic field map in the transition region between the barrel and endcap. The coordinate system is rotated by $\phi = \frac{\pi}{8}$ with respect to the ATLAS coordinate system.

The muon spectrometer is an "air core" toroid to minimize the amount of material traversed by particles in the MS. However, there is a non-negligible amount of material present in the form of support structures, magnet coils and muon chambers. Figure 2.10 shows the total number of radiation lengths due to the material in the MS. Over a wide range of acceptance in the barrel MS, the total amount of material traverse is $\sim$1.3 X_0.

2.5.1 Monitored Drift Tubes

In the barrel, the MDT chambers are placed around the eight superconducting coils which form the toroid magnet, as shown in Figure 2.11. In the endcap, MDT chambers are located either before or

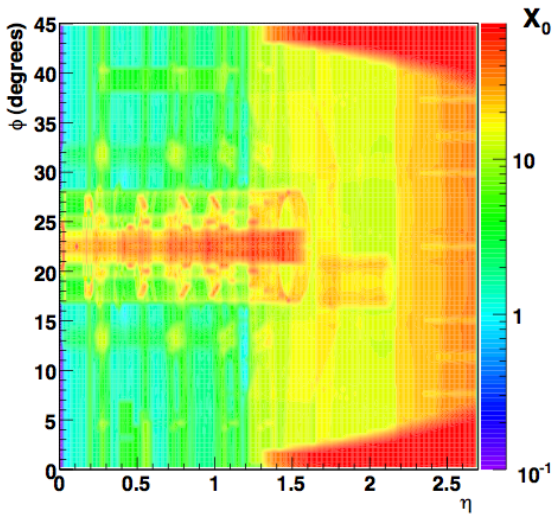

Figure 2.10: The amount of material in units of radiation lengths (X_0) traversed by muons after passing through the calorimeters, as a function of η and ϕ. Some of the more distinctive features include the barrel toroid at $\phi = 22.5^\circ$ and the endcap toroid at $\phi = 0^\circ$ and 45° for $|\eta| \geq 1.4$.

after the endcap toroid; therefore, all the endcap chambers are located outside of the magnetic field region.

The chambers are divided into two types, depending on their position in phi. Those chambers which are located in between the magnet coils are referred to as large sectors, while those next to the magnet coil are small sectors. The chamber naming scheme uses a three letter acronym (ex. BIL, EMS) to specify a chamber type. The first letter (B or E) refers to Barrel or Endcap chambers, respectively. The second letter specifies the layer (Inner, Middle or Outer) and the third letter refers to the sector (Large or Small).

The MDT chambers are built from two multilayers which are separated by up to $\sim$31 cm, see Table 2.2. Each multilayer consists of three or four layers of drift tubes. The individual drift tubes are 30 mm in diameter and have a length of $\sim$2-5 m depending on the chamber, see Table 2.2. The tubes contain an Ar/CO_2 gas mixture (93/7) at 3 bar which produces ionization electrons as charged particles cross the tube. These electrons are then collected at a central wire which is held at a poten-

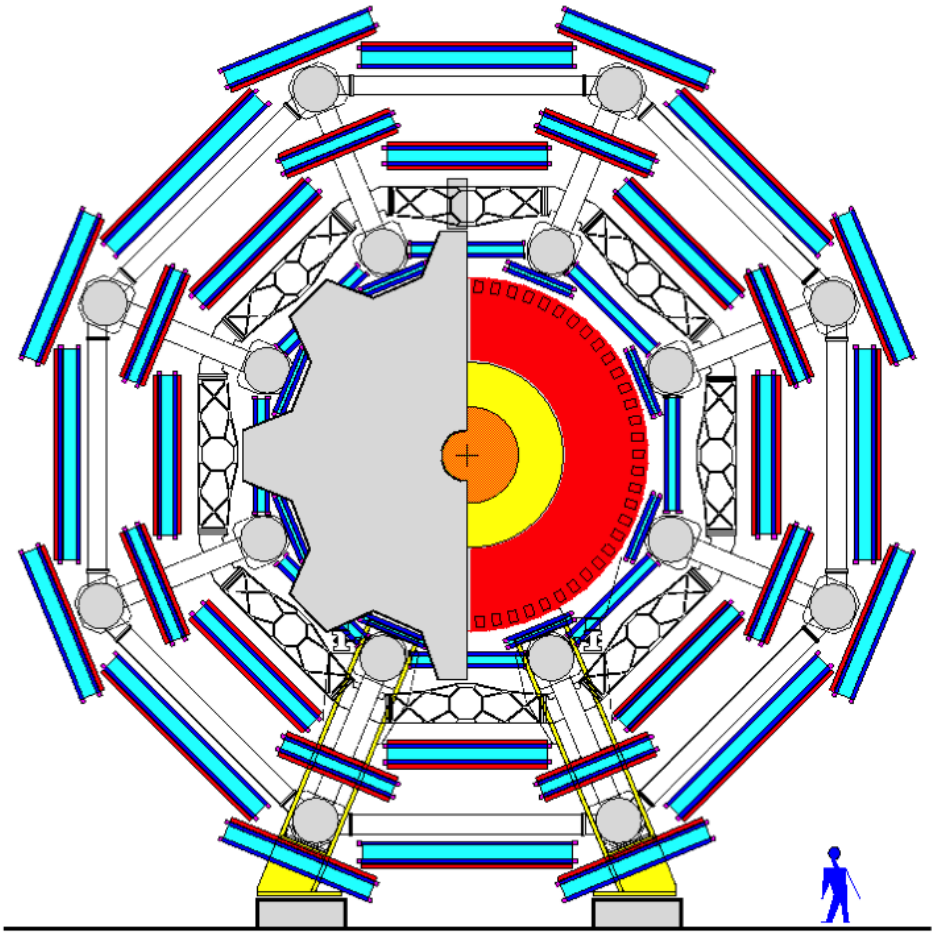

Figure 2.11: The ATLAS muon spectrometer. The barrel MDT chambers are shown in light blue, the endcap MDT chambers are dark blue. The RPC chambers are shown in purple.

tial of 3080 V. The distance of closest approach of the charged particle to the wire is reconstructed by measuring the time elapsed from the collision to the collection of the ionization current. The time measurement is converted to a distance by using a calibrated radius-time ($r-t$) relation. This measurement provides a ”drift circle”, which is the circle defined by the distance of closest approach. In each multilayer, a muon segment can be reconstructed by finding the line which is tangent to the drift circles. These muon segments are local measurements of the position and direction of the muon. Figure 2.12 shows a muon traversing a BIS chamber, with the drift circles shown in light purple and the muon segment shown as the dark purple line.

Chamber Type	Tube Layers	Location in R (m)	Tube Length (cm)	Multilayer Spacing (cm)
BIS	2×4	4.55	182	0.65
BIL	2×4	4.95	282	17
BMS	2×3	8.1	322	17
BML	2×3	7.1	370	31.7
BOS	2×3	10.5	392	31.7
BOL	2×3	9.5	511	31.7

Table 2.2: The location in R and the space between multilayers for the MDT barrel chambers.

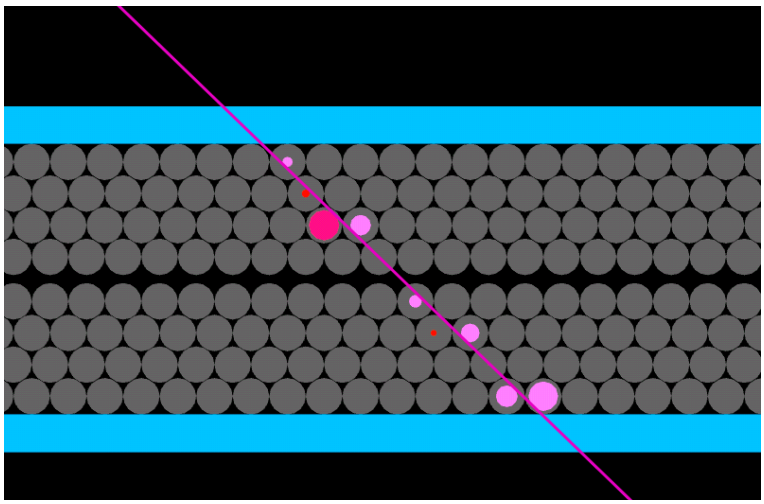

Figure 2.12: A muon traversing a BIS chamber. The drift circles are shown in light purple and the muon is shown as the dark purple line.

Because the MDT tubes are ∼2-5 m in length, the MDT measurement does not provide an accurate phi position or direction. In order to reconstruct the phi position and direction, the MDT measurements need to be combined with the measurements from the RPC (in the barrel) or the TGC (in the endcap).

MDT Calibration

The MDT $r-t$ relations are dependent on many external variables, such as temperature, precise gas mixture and the magnetic field. In order to ensure the best performance of the MDTs, they are routinely calibrated. The calibration routine groups the MDTs into groups which have approximately equal conditions (i.e. B-field and gas) and uses a high statistics sample of well reconstructed muons (see Section 3.5) to correct the $r-t$ relations. The routine selects the MDT hits associated to the track segments, and iteratively refits them, allowing the drift radii to float, until the hit residuals are minimized. Using this procedure, the MDT $r-t$ relations are accurate to a level of $\sim$20 μm.

2.5.2 Cathode Strip Chambers

The CSC chambers are located in the inner layer of the endcap at high pseudorapidity ($2 < \mid \eta \mid < 2.7$) as shown in Figure 2.8. The CSC's are multiwire proportional chambers with two sets of cathodes, one on either side of the gas gap and a set of anode wires in the middle of the gap. The gas gaps are 5.08 mm wide, and the wires are held at a potential of 1900 V with respect to the cathodes. The cathodes are used in the readout while the wires are used only to provide the potential difference. One of the cathode planes is segmented in η and the second in ϕ, such that each gas gap measures both η and ϕ. The cathode strips are 1.13 mm (1.72 mm) wide for the readout (intermediate) strips with an inter-strip spacing of 0.25 mm in the precision (bending) plane while the ϕ strips have a width of 12.15 mm. The position of the charged track is obtained by interpolation between the charges on adjacent strips, yielding a resolution of 60 μm per CSC plane. Each CSC contains four independent gas gaps, resulting in four measurements of η and ϕ along each track.

2.5.3 Resistive Plate Chambers

The RPC chambers provide the trigger system and measure the phi coordinate for muon segments in the MS barrel. The chambers are located on either side of the MDT middle station and on the MDT outer station. In Figures 2.8 and 2.11 the RPC chambers are shown as the purple chambers. The stations are named RPC1, RPC2 and RPC3 for the innermost, middle and outermost stations, respectively.

The RPC's are a gaseous parallel-plate detector without wires. Each chamber is made from two separate detector layers, each of which measure η and ϕ. The detector layers are 2 mm gas-gaps filled with $C_2H_2F_4$:Iso-C_4H_{10}:SF_6 (94.7:5:0.3) and have an electric field of 4.9 kV/mm in the gap. The signal is readout via metallic strips on either side of the gas-gap. The strips have a width of 23-35 mm and a spacing between strips of 2 mm. The RPC single layer efficiency has been measured to be be greater than 97%.

2.5.4 Thin Gap Chambers

The middle station of MDT's in the endcap is surrounded by seven layers of TGC's, three layers in the inner most TGC chamber (TGC1) and two layers each in the outer chambers (TGC2 and TGC3). Additionally, the inner MDT station is complemented with two TGC layers (Endcap Inner TGC or EI TGC). The chambers are shown in Figure 2.8 as the purple chambers.

The TGC's are comprised of a gas volume containing a wire plane and two cathodes, as shown in Figure 2.13. The 2.8 mm wide gas-gap is filled with CO_2:n-C_5H_{12} (55:45) and the wires are held at a potential of 2900 V. The wires are arranged to measure the η coordinate and the cathode planes measure the azimuthal coordinate.

2.6 Luminosity Detectors

There are two primary detectors used to make luminosity measurements: LUCID and the Beam Condition Monitor (BCM).

2.6.1 LUCID

LUCID (LUminosity measurement using Cerenkov Integrating Detector) is a Cerenkov detector located at z = $\pm$17 m and is only 10 cm from the beam pipe ($\eta \approx 5.8$). LUCID consists of twenty aluminium tubes which surround the beam pipe and point toward the IP. The 1.5 m long tubes are 15 mm in diameter and filled with C_4F_{10} at $\sim$1.3 bar. This provides a Cerenkov threshold of

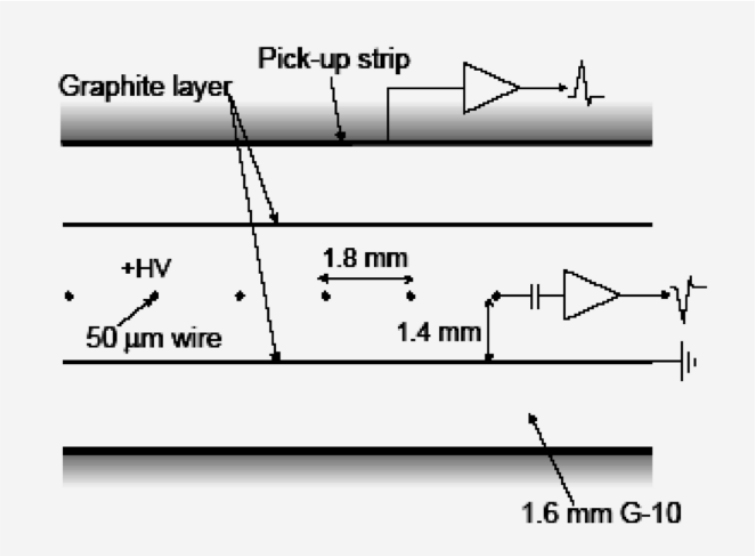

Figure 2.13: TGC structure showing the anode wires, graphite cathodes, G-10 layers and a pick-up strip, orthogonal to the wires.

2.8 GeV for pions and 10 MeV for electrons. The Cerenkov light is measured by Photomultiplier tubes (PMTs) located at the back end of the aluminium tube. The PMT response is proportional to the number of particles traversing the tube allowing for thresholds to be set to optimize signal performance.

2.6.2 Beam Condition Monitor

The BCM consists of two stations of detectors, each with four modules. The stations are located symmetrically around the IP, positioning the modules at z = $\pm$1.84 m and R = 55 mm ($\mid \eta \mid \approx 4.2$). The modules are made of two diamond sensors which are readout in parallel. The modules are arranged in a cross pattern, with two modules in the horizontal plane (BCMH) and two in the vertical plane (BCMV). Because BCMH and BCMV are read out separately, each BCM station makes two independent luminosity measurements.

2.7 Trigger System

The bunch crossing frequency in the LHC can reach ∼40 MHz; however, only 300-400 Hz can be recorded due to the constraints of data storage and event processing time. Therefore, ATLAS uses a three tiered trigger system to select events of interest. Each level of the trigger refines the decision of the previous level by using more detailed information and more advanced algorithms. At each level of the trigger, the rate is decreased from 40 MHz to 75 kHz (after Level 1) and finally to 300-400 Hz (after Level 2 and 3).

2.7.1 The Level 1 Trigger

The Level 1 (L1) trigger searches for high transverse-momentum muons, electrons, photons, jets and τ-leptons, as well as large missing and total transverse energy. The L1 trigger uses reduced-granularity information from calorimeter and MS trigger chambers to select Regions of Interest (RoI's). The RoI contains the coordinates, (η,ϕ), of the triggered object as well as information about the type of object (e.g. electron, muon, etc.) and the object's energy. This information is processed by the Central Trigger Processor (CTP) which implements a trigger menu made up from combinations of trigger elements. For events which are accepted by the CTP, the RoI is passed to the Level 2 trigger for further processing.

Trigger Naming Convention

The triggers are named according to the level where the trigger is run, the type of object the trigger selects, and the energy threshold. For example, the trigger L1_MU6 is a Level 1 (L1) trigger which selects muons (MU) with $p_{\mathrm{T}} > 6$ GeV, or the L1_2MU6 trigger requires two muons with $p_{\mathrm{T}} > 6$ GeV. Other trigger objects, such as jets, tau's, or electrons/photons are selected by the L1_J, L1_TAU, and L1_E, respectively.

Level 1 Muon Trigger Operation

The Level 1 muon trigger coverage is provided by the RPC, in the barrel, and the TGC chambers, in the endcap. The trigger is separated into two types: low p_{T} (approximately 6-9 GeV) and high p_{T} (approximately 9-40 GeV). The trigger is based on a coincidence matrix, requiring hits in both

RPC1 and RPC2 (TGC2 and TGC3) for the low p_T trigger in the barrel (endcap) and hits in all three stations for the high p_T trigger, as shown in Figure 2.14. The size of the coincidence matrix is set in firmware and is related to the p_T threshold for the trigger. In the barrel, the muon RoI's have a

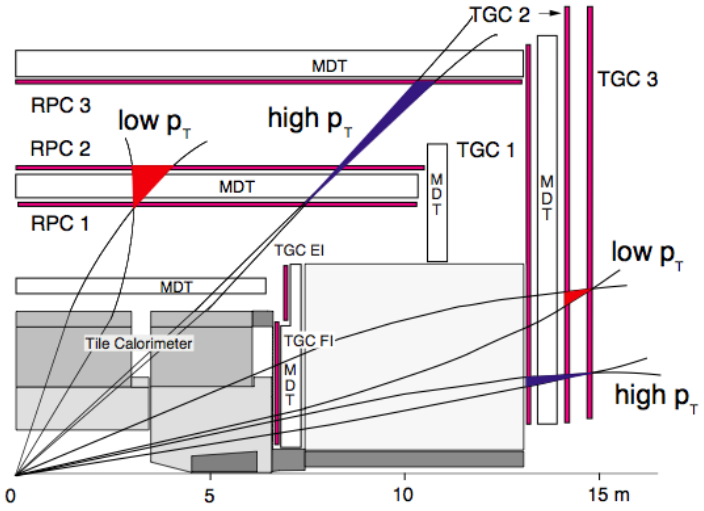

Figure 2.14: The schema of the Level 1 muon trigger. The RPC/TGC are arranged in three stations (RPC1,RPC2 and RPC3 or TGC1, TGC2 and TGC3). The low p_T trigger uses RPC1 and RPC2 in the barrel and TGC3 and TGC2 in the endcap. The high p_T trigger uses all three stations: RPC1,RPC2 and RPC3 in the barrel or TGC1,TGC2 and TGC3 in the endcap.

spatial extent of $\sim$0.2$\times$0.2, in $\eta \times \phi$, and are limited to two RoI's per RPC sector. In case more than two RoI's are found in the same sector, the two highest p_T RoI's are selected by the muon CTP for processing at Level 2.

2.7.2 The Level 2 Trigger

The Level 2 (L2) trigger is seeded by the RoI's found at L1. The L2 trigger has access to the full granularity of the detector in the vicinity of the RoI coordinates, approximately 2% of the total detector information. The L2 trigger uses this detailed information to refine the decision of the L1 CTP and rejects events to reduce the total rate of $\sim$3.5 kHz.

2.7.3 The Event Filter

The final event selection is provided by the Level 3 trigger, known as the Event Filter (EF). The EF has access to the full event information and uses more advanced algorithms to reconstruct and analyze the event. Events which pass the EF are written to mass storage and are available for analysis using the ATLAS offline software.

Chapter 3

RECONSTRUCTION

ATLAS makes several independent measurements of each particle as it passes through the detector. For example, a charged particle will have it's position measured by the inner detector subsystems and will leave energy in several calorimeter cells. In order to analyze the collisions, the information from each of the subsystems needs to be combined to form the high-level physics objects which will be used in the analysis.

3.1 Track Reconstruction

3.1.1 SpacePoint Formation

The first step in track reconstruction is to convert the individual pixel and SCT measurements ("hits") into three-dimensional points (SpacePoints). For measurements from the Pixel detector, this is trivially done since each pixel is able to measure both ϕ and z with high accuracy and is located at a known radius, R. Single SCT measurements are not sufficienct to produce a unique SpacePoint because only the coordinate orthagonal to the silicon strip is well measured. To create a SpacePoint, it is neccessay to combine a single SCT strip measurement with it's stereo partner strip. The stereo pair of SCT measurements, combined with the IP constraint, allows the SCT measurements to be combined into a single SpacePoint measurement. Measurements from the TRT are converted from drift times to drift radii by using the $r-t$ relations.

3.1.2 Pattern Recognition

The reconstructed SpacePoints are used to seed the inside-out track finding algorithms [32, 33]. Track seeds are formed using a combination of SpacePoints from the three pixel and first SCT layers. These seeds are then extended thoughout the ID volume using a Kalman filter and hits along the path are associated to the track candidate. Next the track candidates are fit, using all the asso-

ciated hits. "Outlier" hits[1] are removed from the track and quality cuts are applied to remove the fake tracks. The quality cuts includes a cut on the minimum number of SpacePoints associated to a track and a cut on the number of "holes" on the track. A "hole" occurs when a track cross an active tracking element but no hits are measured in the detector. Only about 1% of the track candidates satisfy all of the quality criteria to be considered a reconstructed track.

Once the inside-out track finding has completed, the back-tracking (or outside-in) track algorithms are run. These algorithms start by removing all hits used by the inside-out tracking from consideration to avoid duplicating tracks. The back-tracking algorithm starts by finding track seeds in the TRT using a histogramming track finding technique. A Hough transform [34] is used to project the hits from the r-ϕ (z-ϕ) plane in the barrel (endcap), into the parameter space of a straight line. The line is parameterized by the initial azimuthal angle, ϕ_0, and the inverse momentum p_{T}^{-1} (or p_z^{-1} in the endcap). The parameter space is histogrammed and track finding is reduced to locating local maxima in the histogram. These TRT tracks are then extrapolated back toward the IP and hits in SCT and pixel detectors are associated to the track. The track is finally refit using all of the associated hits and outliers removed.

3.2 Primary Vertex Reconstruction

Reconstructed tracks are used to find the primary vertices, the points where pp collisions occurred [35]. The reconstructed tracks which satisfy the following quality criteria are used for the primary vertex reconstruction:

- $p_{\mathrm{T}} > 500$ MeV
- $|\mathrm{d}_0| < 4$ mm
- $\sigma(\mathrm{d}_0) < 5$ mm
- $\sigma(\mathrm{z}_0) < 10$ mm

[1] Outlier refers to those hits which give a large χ^2 when they are included in the track fit.

- at least 2 hits in the pixel detector
- at least 4 hits in the SCT

The transverse and longitudinal impact parameters, d_0 and z_0, are measured with respect to the center of the luminous region and $\sigma(d_0)$ and $\sigma(z_0)$ are the corresponding uncertainties. This selection criteria is designed to remove tracks originating from secondary interactions or other wise poorly reconstructed tracks.

The position of the primary vertices is then determined using an adaptive vertex fitting algorithm. This algorithm uses an iterative χ^2 minimization routine [36] which down-weights the contribution of outlying tracks[2]. Tracks are considered to originate from the vertex if they are compatible with the vertex with $\chi^2 < 49$. The tracks which are incompatible with the found vertex are used to reconstruct the successive primary vertices. This process continues until there are either no tracks left unassociated to a vertex or it is not possible to reconstruct a vertex with an acceptable χ^2. The vertices are then ordered by the average p_{T} of tracks originating from the vertex. The vertex with the highest average p_{T} is considered to be the signal vertex (the position of the inelastic collision) and the other vertices are considered to be from "pileup" collisions. During 2011, the number of primary vertices reconstructed varied between an average of $\sim$4 per event (in March) to $\sim$15 (in October). The increase in the number of pileup vertices was due an increase in the number of protons per bunch and a decrease in β^* (see Section 2.1.3).

3.3 Photon Reconstruction

Photon identification [37, 38] is seeded by energy clusters in the electromagnetic calorimeter. The reconstruction algorithm searches for energy clusters in projective towers of 3×5 cells in the second layer of the ECal. The energy clusters are then matched to tracks reconstructed in the ID. Energy clusters without any matching tracks are considered to be photon candidates. Energy clusters which are matched to tracks originating from a conversion vertex [33] are also stored as photon candidates.

[2]Outlying tracks are those which have a χ^2 greater than a threshold χ^2 value.

To discriminate from backgrounds, the shape of the energy deposit in the ECal is inspected. Due to the large amount of material in the ECal ($\sim$24 X_0), photons are expected to deposit nearly all of their energy in the ECal with little or no energy being deposited in the HCal. Therefore, the photon candidates must have less than 2% energy leakage ($E_T^{HCal}/E_T^{Total} < 2\%$). Next the lateral and longitudinal shower shapes are inspected. The ratio of energy deposits in 3×7 cells over 7×7 cells (R_η) and 3×3 cells over 3×7 cells (R_ϕ) in $\eta \times \phi$ are computed. The cuts applied to the ratios, R_η and R_ϕ, is dependent on the photon η and are designed to have an efficiency of $\sim$99% for true prompt photons. Finally, the development of the shower in the calorimeter is examined. The energy deposits in the first layer of the ECal are examined for the presence of multiple particles or overlapping showers. The presence of multiple particles (or overlapping showers) is used to reject photon candidates which originate from π^0 decays and other sources of background.

Photon candidates which satisfy all of the selection criteria are promoted to photon objects. These photons are then divided into two categories: isolated and non-isolated. The total energy in a isolation cone of $\Delta R = 0.4$ is computed, excluding the energy of the photon cluster. Photons which have less than 3 GeV in the isolation cone are considered to be isolated, while those with more than 3 GeV are non-isolated.

3.4 Electron Reconstruction

Electron reconstruction [37, 39] uses a sliding window of 3×5 ($\eta \times \phi$) cells, in the second layer of the ECal, to select clusters of energy in the ECal. The energy cluster is then required to match to a reconstructed ID track. The matching track is required to be within $\Delta\eta < 0.01$, have p_T >0.5 GeV and be reconstructed using at least one pixel hit, seven total hits in the pixel and SCT, and 10 TRT hits. Clusters with a matching track are then subjected to a series of cuts on the shower shape in the ECal, similar to those applied to photon candidates. Surviving electron candidates can be further purified by making cuts on the number of high-threshold TRT hits (see Section 2.3.3) and requiring the ratio E/p be approximately 1, where E is measured in the calorimeter and p is measured from the ID track.

3.5 Muon Reconstruction

Muon identification and reconstruction relies on measurements made in both the ID and MS. There are three different approaches to muon reconstruction [40] allowing for coverage up to $|\eta| < 2.7$ and over a wide range of p_{T}.

The *standalone muon* reconstruction algorithm uses only the hits in the MS to reconstruct a muon track. This is done by first reconstructing MDT segments in individual MDT chambers. These MDT segments are then combined with measurements from the RPC (in the barrel), or the TGC (in the endcap) to create a muon segment with a well defined ϕ coordinate. Because ATLAS uses a toroidal magnetic field in the MS, the muon segments are required to point in the radial direction. Muon segments from multiple stations (inner, middle and outer) are then combined using a global fit to create a muon track and measured the parameters (p_{T}, η, ϕ) are expressed at the entrance to the MS.

The *combined muon* reconstruction algorithm starts with a standalone muon track. The standalone muon is then extrapolated through the calorimeter, correcting for energy loss, to the inner detector. The muon track is then paired with an ID track on the basis of χ^2 match between the track parameters. The full muon track (ID+MS) is then either refit or formed from a statistical combination of the two tracks.

The *tagged muon* reconstruction algorithm is designed to recover efficiency for low momentum muons ($p_{\mathrm{T}} < 1$ GeV in the MS). The algorithm extrapolates inner detector tracks through the calorimeter and attempts to associate a muon segment to the ID track. In case the ID track is matched to a muon segment, the ID track is considered to be a muon and the track parameters are taken to be those of the ID track.

Reconstructed muons are then classified as *isolated* or *non-isolated*. Isolation is done with respect to inner detector tracks and calorimeter energy as:

- Track Isolation: $\sum p_{\mathrm{T}}(\Delta\mathrm{R}<0.4)/p_{\mathrm{T}}(\mu)$, where the sum is over all ID tracks in the cone, ex-

cluding the muon track.

- Calorimeter Isolation: the transverse energy (E_{T}) deposition in the calorimeter in a cone of ΔR<0.4 around the muon is required to be less than $0.2p_{\mathrm{T}}(\mu)$. The energy in the isolation cone is corrected for the muon energy loss.

This muon isolation provides a powerful tool for rejecting muon which originate from hadron decay.

3.6 Jet Reconstruction

Jet reconstruction [41, 42] is uses the anti-k$_t$ algorithm [43] with a distance parameter R = 0.4. The jets are constructed using topological clusters "topoclusters" in the calorimeter. Topological clusters attempt to reconstruct the three-dimensional shower topology of particles in the calorimeter. The clusters are seeded from cells that satisfy $\mathrm{E}_{cell} > 4\sigma_{noise}$ and then iteratively adding neighboring cells with $\mathrm{E}_{cell} > 2\sigma_{noise}$, where σ_{noise} is the measured electronic noise. In the final step, all cells which directly neighbor the cluster are added.

The anti-k$_t$ algorithm starts by selecting the topocluster with the highest p_{T} and defining it to be a jet. The algorithm then looks for near by topoclusters which can be added to the jet. This is done by computing the distance parameter:

$$d_{ij} = \frac{(\eta_i - \eta_j) + (\phi_i - \phi_j)}{R\ p_{T,i}^2} \tag{3.1}$$

where i denotes the jet and j denotes the topocluster. The $j-th$ topocluster is merged with the jet if d_{ij} is less than $\frac{1}{p_{T,i}^2}$. This process continues until no more topoclusters are added to the jet. The algorithm then selects the highest p_{T} topocluster, that is not already part of a jet, and uses it to seed a new jet. This process repeats until there are no more seeds left.

Once reconstructed, the jet four-vector can be computed by summing the four-vectors of each topocluster, assuming zero mass for the topocluster:

$$p^{\mu}_{topocluster} = < E, E \cdot \tfrac{cos\phi}{cosh\eta}, E \cdot \tfrac{sin\phi}{cosh\eta}, E \cdot tanh\eta > \tag{3.2}$$

$$p^{\mu}_{jet} = \sum_i p^{\mu}_{topocluster,i} \tag{3.3}$$

where E is the total energy of the topocluster, and η and ϕ are the energy weighted position of the topocluster.

3.6.1 Jet Quality Definition

To ensure that energy deposits in the calorimeter are due to physics arising from the collision, jets are identified as "good", "bad" or "ugly". Good jets are those jets which are produced in the collision and are well measured, while the ugly jets are those jets that are produced in the collision, but are not well measured. By contrast, the bad jets are energy deposits in the calorimeter which are not from the collision, but are produced by detector noise, cosmic ray showers, or beam halo.

Jets coming from the decay of a long-lived particle can originate throughout the detector volume; therefore, a custom definition of a good jet is required. The standard good jet definitions [44] used in ATLAS assume the jet originates at the IP and thus deposits energy in both the electromagnetic and hadronic calorimeters. However, if a long-lived particle decays inside the hadronic calorimeter, and therefore leaves no energy in the electromagnetic calorimeter, the assumptions made by the standard good jet criteria are no longer valid.

The bad jet criteria is based upon several discriminating variables, summarized below.

- EMf: The fraction of the jet's energy which is in the electromagnetic calorimeter.
- FMax: The maximal fraction of energy contained in one calorimeter layer.
- HECf: The fraction of the jet's energy contained in the HEC.
- LArQ: The fraction of LAr cells with a cell Q-factor[3] greater than 4000.
- HECQ: The fraction of HEC cells with a cell Q-factor greater than 4000.
- NegativeE: The total amount of negative energy in the jet.

[3]The cell Q-factor measures the difference between the predicted and measured pulse shapes.

- t: The energy weighted average time of all cells used in the jet reconstruction.
- η: The η of the jet.
- CHf: The jet charge fraction, the ratio of $\sum_{tracks} p_{\mathrm{T}}^{track}$ to the calibrated jet p_{T}.

Using these variables, a bad jet is defined as any jet that satisfies at least one of the following criteria:

- HECf $>$ 1-|HECQ|
- |NegativeE| $\geq$ 60 GeV
- EMf $>$ 0.9 and |LArQ| $>$ 0.8 and $|\ \eta\ | < 2.8$
- |t| $>$ 25 ns
- FMax $>$ 0.99 and $|\ \eta\ | < 2$
- EMf $>$ 0.95 and CHf $<$ 0.05 and $|\ \eta\ | < 2$

Ugly jets are those jets which are either in the transition region between the barrel and endcap or have significant energy deposited in problematic calorimeter cells. The ugly jets are therefore defined as jets that satisfy one of the following criteria:

- The fraction of jet energy contained in the TileGap3[4] is greater than 50% of the total jet energy
- The fraction of jet energy that is in dead[5] or problematic cells is greater than 50% of the total jet energy.

Good jets are then defined to be those jets which are neither bad nor ugly. Unless otherwise noted, all jets used in the analysis are good jets, using these definitions.

---

[4]TileGap3 is the portion of the calorimeter that covers the transition between the barrel and endcap calorimeters.

[5]The energy in dead cells is estimated from the surrounding calorimeter cells.

3.6.2 LAr Hole

During part the 2011 data taking, one of the LAr calorimeter's power supplies failed, producing a region of the calorimeter that was unable to measure energy. This hole covers the region -0.74 $< \phi <$ -0.69 and 0 $< \eta <$1.4. To ensure that all the jets used in the analysis are well measured, any event containing a jet with $E_{\mathrm{T}} \geq 20$ GeV that falls within ΔR < 0.4 of the LAr hole is rejected. This rejection leads to a loss of acceptance that is purely geometric and therefore can be applied to the Monte Carlo signal.

3.7 τ-lepton Reconstruction

Hadronically decaying τ-leptons are reconstructed [45, 46] from either track or calorimeter seeds. *Track-seeded* τ candidates have a seed track with $p_{\mathrm{T}} > 6$ GeV, reconstructed with at least 7 total hits in the pixel plus SCT, and have impact parameters that satisfy $\mathrm{d}_0 < 2$ mm, $|\mathrm{z}_0| \times \sin\theta < 10$ mm. *Calorimeter-seeded* τ candidates consist of jets, reconstructed with the Anti-k_t algorithm, that have $E_{\mathrm{T}} > 10$ GeV. Those τ candidates which are seeded by both the track and calorimeter seeds, separated by ΔR < 0.2 are referred to as *double-seeded*.

The selection of τ candidates uses very loose criteria and provides little background rejection. Instead the τ candidates are identified in a second step which uses several discriminating variables to select the true τ's. Hadronically decaying τ's are characterized by one or three collimated tracks and a corresponding narrow energy deposition in the calorimeter. The τ's are identified by using several variables including the τ candidate invariant mass, fraction of energy in the core (ΔR < 0.1) of the jet, and the shape of the shower in the EM calorimeter.

3.8 Missing Energy

Because the protons involved in collisions in ATLAS have $p_{\mathrm{T}} \sim 0$, the final state should also have $p_{\mathrm{T}} \sim 0$. However, some particles, such as neutrinos, escape the detector without interacting causing the event to appear unbalanced. The "missing" energy (MET or E_T^{miss}) [47] can be inferred from conservation of momentum. This is done by summing the transverse energy in the calorimeters and

the transverse momentum of the reconstructed muons as:

$$E_{x(y)}^{miss} = E_{x(y)}^{miss,calo} + E_{x(y)}^{miss,\mu} \tag{3.4}$$

Then the values of E_T^{miss} and the direction of the MET, ϕ^{miss} can be calculated as:

$$E_T^{miss} = \sqrt{(E_x^{miss})^2 + (E_y^{miss})^2} \tag{3.5}$$

$$\phi^{miss} = \arctan(E_y^{miss}/E_x^{miss}) \tag{3.6}$$

The missing energy in the calorimeter, $E_{x(y)}^{miss,calo}$, is found by summing the transverse energy of all of the reconstructed objects in the event:

$$E_{x(y)}^{miss,calo} = E_{x(y)}^{miss,e} + E_{x(y)}^{miss,\gamma} + E_{x(y)}^{miss,\tau} + E_{x(y)}^{miss,jet} + E_{x(y)}^{miss,calo,\mu} + E_{x(y)}^{miss,CellOut} \tag{3.7}$$

where the terms correspond to the following:

- $E_{x(y)}^{miss,\gamma}$,$E_{x(y)}^{miss,e}$,$E_{x(y)}^{miss,\tau}$: The sum of the energy from photons, electrons and τ-leptons, respectively.

- $E_{x(y)}^{miss,jet}$: The sum of energy from jets with $p_{\mathrm{T}} > 7$ GeV.

- $E_{x(y)}^{miss,calo,\mu}$: The sum of energy deposited by muons as they traverse the calorimeter.

- $E_{x(y)}^{miss,CellOut}$: The sum of energy in topoclusters which are not included in any of the above terms.

The missing energy from muons is calculated from combined muons, in the range $|\eta| < 2.5$, and standalone muons in the range $2.5 < |\eta| < 2.7$. In order to avoid double counting, the energy deposited in the calorimeter, $E_{x(y)}^{miss,calo,\mu}$, is only used in the calculation of MET for non-isolated muons. In this case, the muon momentum, as measured in the MS, is used in calculation of $E_{x(y)}^{miss,\mu}$, while for isolated muons, the combined muon momentum is used in the calculation.

3.9 Luminosity Measurement

An accurate measurement of the luminosity [48] is an essential component of any analysis, as it is needed to predict the expected number of events for a given process. This directly affects both the

measurement of cross-sections for known process and searches for new physics. In a search, the integrated luminosity is used to estimate backgrounds and the number of expected signal events.

The instantaneous luminosity can be calculated as:

$$\mathrm{L} = \frac{\mu n_b f_r}{\sigma_{inel}} \tag{3.8}$$

where μ is the average number of interactions per bunch crossing (BC), n_b is the number of bunches, f_r is the rotation frequency and σ_{inel} is the inelastic cross-section. However, it is not possible to measure μ directly, because the detectors have a finite acceptance and efficiency. Therefore, the measured number of interactions, μ^{meas}, can be expressed as $\mu^{meas} = \varepsilon\mu$, where ε accounts for the acceptance and efficiency of the luminosity detectors. Defining σ_{vis} as $\sigma_{vis} = \varepsilon\sigma_{inel}$, equation 3.8 becomes:

$$\mathrm{L} = \frac{\mu^{meas} n_b f_r}{\sigma_{vis}} \tag{3.9}$$

Relative changes in the instantaneous luminosity can be measured by knowing the value of μ^{vis}. However, in order to measure the instantaneous luminosity, it is necessary to determine the value of σ_{vis}. This can be done by formulating the instantaneous luminosity in terms of the machine parameters [49]:

$$\mathrm{L} = \frac{n_b f_r N_1 N_2}{2\pi\Sigma_s\Sigma_y} \tag{3.10}$$

where N_1 and N_2 are the number of protons per bunch in beams 1 and 2, respectively. Σ_x and Σ_y are characteristics of the beam profiles in horizontal and vertical planes, respectively.

By using dedicated van der Meer scans [50], the necessary machine parameters can be directly measured. In a van der Meer scan, one of the beams is displaced vertically (or horizontally) with respect to the other, in steps of a known distance. The size and shape of the interaction region can be determined by recording the interaction rates as a function of the separation. This is a direct measurement of Σ_x and Σ_y, and thereby allows σ_{vis} to be calculated in terms of experimentally observable variables:

$$\sigma_{vis} = \mu^{meas}_{MAX} \frac{2\pi\Sigma_x\Sigma_y}{N_1 N_2} \tag{3.11}$$

where μ_{MAX}^{meas} is the peak interaction rate measured during the van der Meer scan and corresponds to the beams having zero separation.

Chapter 4

SIMULATION OF HIDDEN VALLEY SIGNAL SAMPLES

In order to study the response of the ATLAS detector to highly displaced decays, four samples of signal Monte Carlo (MC) samples have been produced using PYTHIA [51], version 6.423. In each of the samples, the Higgs is produced via gluon fusion and then subsequently decays to a pair of long-lived π_v's, see Figure 4.1. To simulate a π_v particle that decays mainly to heavy flavor, the

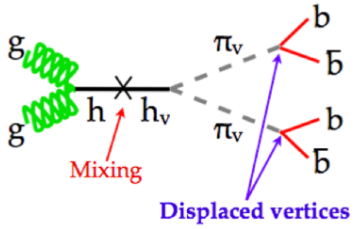

Figure 4.1: Higgs decay to Hidden Valley π_v.

A^0, which is already defined in PYTHIA, is used as a surrogate. Instead of directly simulating the SM Higgs (h^0) in PYTHIA, it is convenient to use the SUSY Higgs (H^0) which has a coupling to the A^0. The mass of the H^0 is then set to m_{h^0} and the mass and lifetime of the A^0 are set to m_{π_v} and τ_{π_v}. All of the decays of the H^0 are turned off expect $H^0 \rightarrow A^0A^0$ and the A^0 is allowed to decay as it normally does, to heavy flavor quarks and leptons.

The parameters used to generate the samples are summarized in Table 4.1. The lifetimes for each of the samples was chosen (arbitrarily) to give decays throughout the volume of ATLAS.

Due to the production mechanism, gluon fusion, the Higgs is produced boosted in the z-direction with little or no p_T (see Figure 4.2) and only has significant p_T in events where it is recoiling against a high energy jet from Initial State Radiation (ISR). This implies that the π_v's will be produced

Dataset Number	Higgs Mass (GeV)	π_v Mass (GeV)	π_v lifetime (mm)
105377	120	20	730
105378	140	20	630
105379	120	40	1950
106698	140	40	1500

Table 4.1: Hidden Valley signal Monte Carlo parameters.

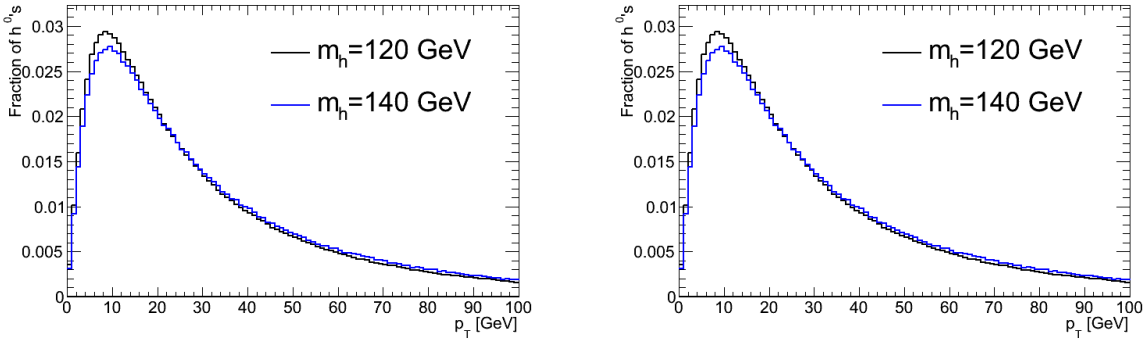

Figure 4.2: Left: The p_z of the Higgs boson in the signal Monte Carlos. Right: The p_T of the Higgs boson in the signal Monte Carlos.

back-to-back in phi, $\Delta\phi \sim \pi$, as shown in Figure 4.3.

Because of the low mass Higgs, the π_v's are not highly boosted. Figure 4.4 (Left) shows that π_v's which are produced in the barrel ($|\eta| < 1$) have β_{π_v} in the range ~0.7-1, depending on the π_v mass. Because the Higgs tends to have significant momentum in the z-direction (Figure 4.2, Left), the π_v which are produced in the forward direction tend to have a higher β_{π_v}, in range ~0.9-1. Figure 4.5 shows the boost, $\gamma = 1/\sqrt{1-\beta_{\pi_v}^2}$, for π_v's produced in the barrel (Left) and endcap (Right). As can be seen, the boost is typically on the order of γ ~1-2 (2-4) for m_{π_v} = 40 GeV and γ ~2-4 (4-10) for m_{π_v} = 20 GeV in the barrel (endcap). The π_v predominately decays to a $b\bar{b}$ pair, which produces an average of 10 low p_T charged particles and 5 π^0 's (Figure 4.6). The relatively low boost implies

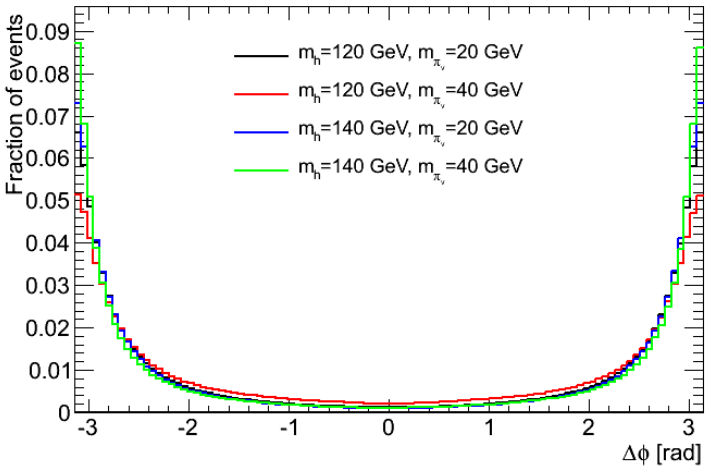

Figure 4.3: $\Delta\phi$ between the two π_v's in each of the four signal Monte Carlos.

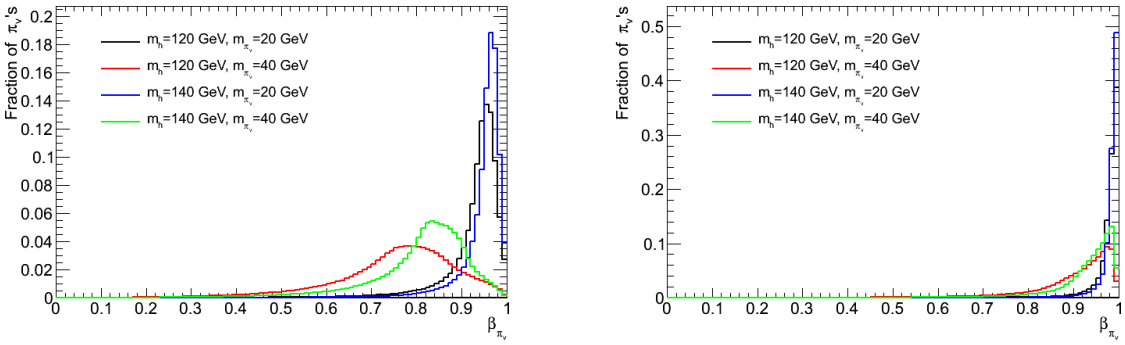

Figure 4.4: Left: The β of π_v's produced in the barrel region, $|\eta| < 1$. Right: The β of π_v's produced in the endcap region, $1 < |\eta| < 2.5$.

that the π_v decay products will have a wide opening angle and be relatively low p_{T}, as can be seen in Figure 4.7.

4.1 Note on the PYTHIA Simulation

The simulation was done in PYTHIA 6 with color connections turned on. This can lead to quarks from the π_v decay to be connected to partons at the IP via a macroscopic gluon string, which is

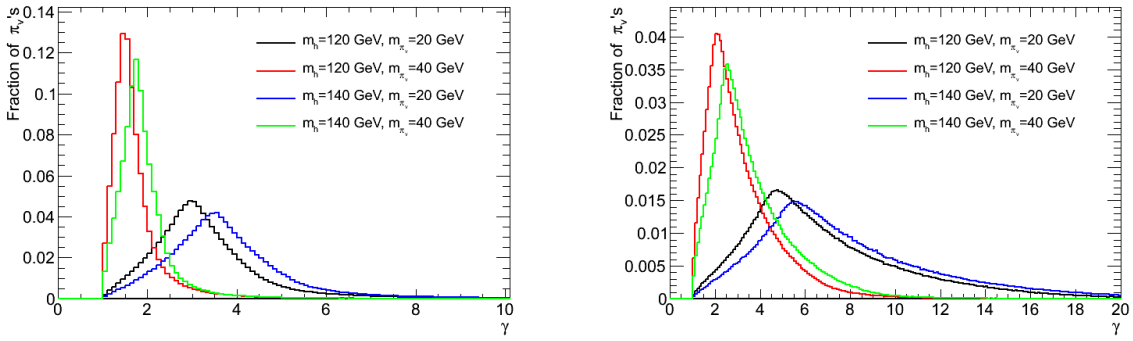

Figure 4.5: Left: The boost, γ, of π_v's produced in the barrel region, $\mid \eta \mid < 1$. Right: The boost, γ, of π_v's produced in the endcap region, $1 < \mid \eta \mid < 2.5$.

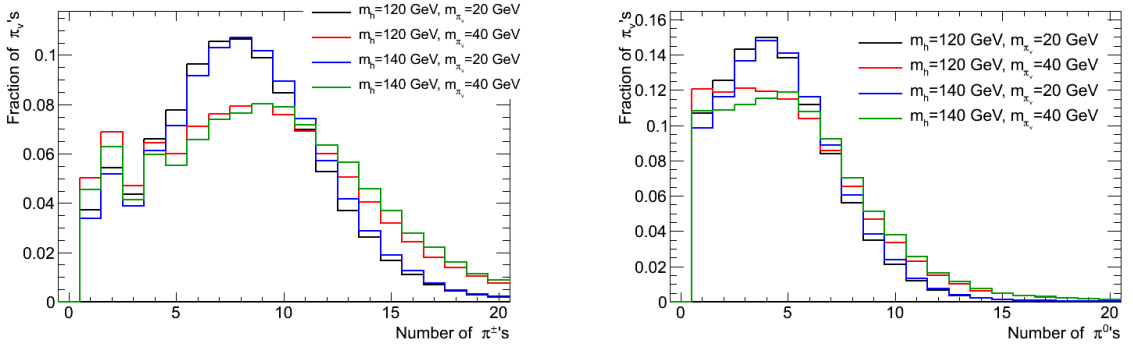

Figure 4.6: Charged hadron (Left) and π^0 (Right) multiplicity in π_v decays to $b\bar{b}$ pairs. Only those particles with $p_{\mathrm{T}} \geq$1GeV are counted.

an unphysical situation. The average probability for a colored decay product of the π_v to have a macroscopic color connection is $\sim$5.7%. The events which exhibit one of these macroscopic color strings are removed from the dataset by requiring both "mothers" of the gluon string be located at the same point in configuration space. The remaining events are then reweighted to preserve the correct branching ratios for the π_v. This reweighting is necessary because π_v's which decay to $\tau^+\tau^-$ do not have any color connections, and their relative proportion in the dataset is increased by the removal of events with long-range color connections.

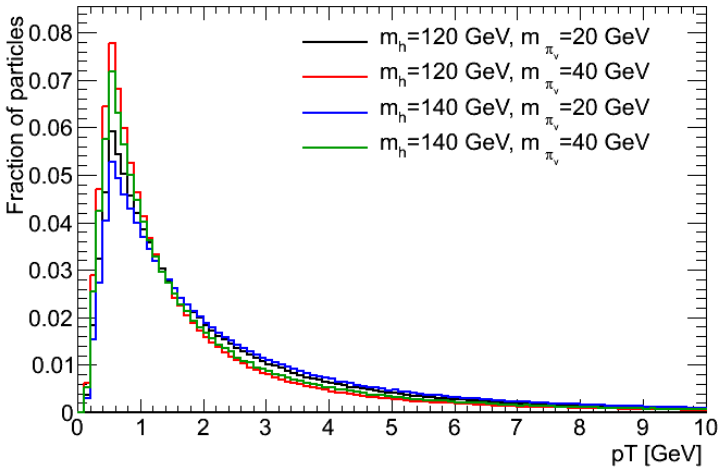

Figure 4.7: p_{T} distribution of MC truth charged particles from π_v decays

4.2 Detector Simulation

The response of the ATLAS detector was modeled using GEANT4 [52] which simulates the propagation and scattering of particles as they traverse the detector. The effects of multiple pp interactions occurring during the same bunch crossing (pileup) was simulated by overlaying several minimum bias events on the signal event. The simulated energy deposits and ionization from the signal event plus pileup are then passed into a simulation of the detector's electronics and digitization. The resulting "Raw Data Objects" (RDO's) that are produced are identical in format to data taken during collisions. The RDO's are then processed by the standard reconstruction algorithms. The last step is to weight the MC events such that the pileup in simulation agrees with the number of pileup events found in data. This reweighting was especially import because the pileup conditions were rapidly changing as the LHC luminosity increased.

Chapter 5

SIGNATURES OF DISPLACED DECAYS AND DEDICATED TRIGGER ALGORITHMS

The Hidden Valley particles, as discussed in [20], can have lifetimes comparable to the ATLAS detector dimensions. This leads to the possibility of displaced decays to (b-)jets occurring throughout the detector volume. Figure 5.1 shows the probability for a π_v to decay in each of the ATLAS subsystems: the Inner Detector[1], electromagnetic (EM) calorimeter, hadronic calorimeter and the muon spectrometer as a function of the π_v proper lifetime ($c\tau$). For each of the subsystems, the combined probability for the π_v to decay in barrel and endcap detectors ($| \eta | < 2.5$) is shown.

The "standard" ATLAS triggers[2] have been designed to select physics originating at (or near) the Interaction Point (IP). Events with long-lived particles present many challenges for these types of triggers: muons from π_v decays do not have associated inner detector tracks, jets from π_v decays are relatively low energy and may not have normal energy deposition. The result of this is a low overall efficiency for triggering on signal events. To improve the triggering efficiency, a set of signature driven triggers has been developed, which select events characterized by highly displaced hadronic jets [53]. In developing these Hidden Valley triggers three regions of the detector have been considered:

- Decays from the end of the hadronic calorimeter to the first muon spectrometer trigger plane
- Decays in the hadronic calorimeter
- Decays beyond the pixel detector though the electromagnetic calorimeter

[1]For the purposes of this analysis, the inner detector is defined as the region outside the volume of the beam pipe ($50 < r < 1000$ mm)

[2]"Standard" ATLAS triggers refers to the trigger items in the menu before the addition of specialized triggers to select displaced decays.

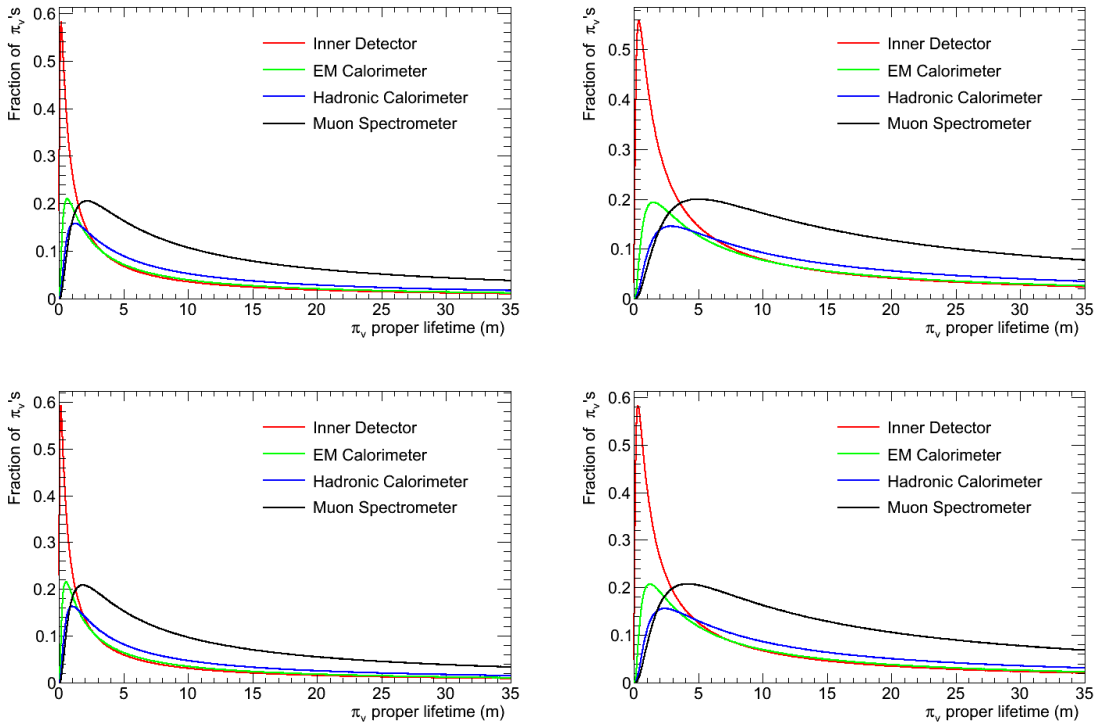

Figure 5.1: Probability for a π_v to decay in each of the detector regions as a function of the π_v proper lifetime for each of the four signal monte carlos. Top Left: m_h = 120 GeV, m_{π_v} = 20 GeV, Top Right: m_h = 120 GeV, m_{π_v} = 40 GeV, Bottom Left: m_h = 140 GeV, m_{π_v} = 20 GeV, Bottom Right:m_h = 140 GeV, m_{π_v} = 40 GeV

For each of these regions a unique decay topology exists which can be used to improve the triggering efficiency for events with displaced decays.

5.1 Decays in the Muon Spectrometer

Decays occurring at the end of the hadronic calorimeter or inside the muon spectrometer result in a large number of charged hadrons traversing a narrow (η,ϕ) region of the spectrometer. The Level 1 muon trigger system will return several Regions of Interest (RoI's) clustered in a small (η,ϕ) area. Figure 5.2 shows a Monte Carlo event with a π_v decaying inside of the barrel muon spectrometer. In the display, inner detector tracks are shown in black, energy in the calorimeter is shown as green boxes (EM energy) and red boxes (hadronic energy). The blue points inside the muon spectrometer

represent MDT measurements, and the four blue bars located outside the detector volume show the location of the RoI's found by the Level 1 trigger. The muon RoI's from this type of decay topology usually will not have any associated tracks in the inner detector or significant energy deposits in the calorimeter.

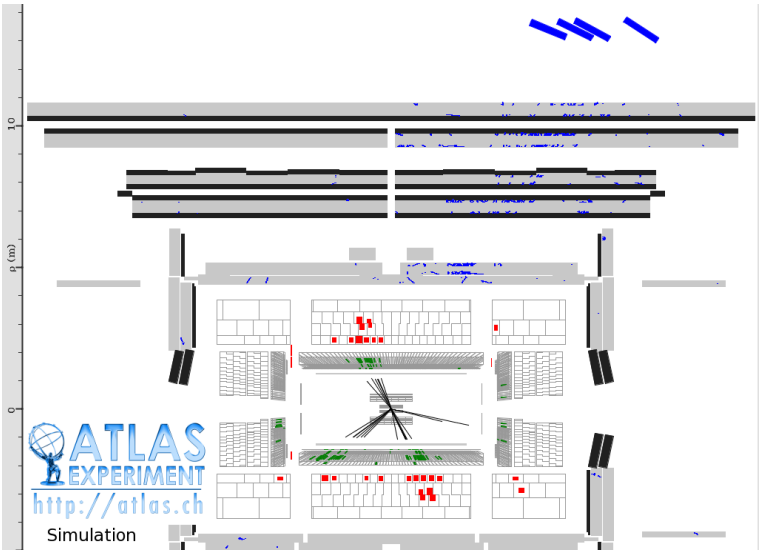

Figure 5.2: Event display from Monte Carlo showing a π_v decay in the barrel muon spectrometer. Reconstructed inner detector tracks are shown in black, energy deposits in the hadronic calorimeter are shown in red and energy in the electromagnetic calorimeter are shown in green. MDT hits are shown as blue points, and the location of the Level 1 muon RoI's are shown by the blue bars located outside the spectrometer.

These events are characterized by a cluster of Level 1 muon RoI's centered around the π_v line of flight. Figure 5.3 shows the total number of RoI's found in events with a π_v decaying inside the barrel muon spectrometer ($R \geq 4$ m). Figure 5.4 gives the average number of Level 1 muon RoI's contained in a cone of $\Delta R = 0.4$ around the π_v line of flight as a function of the π_v radial decay distance and illustrates that a majority of the RoI's from the π_v decay are clustered around the π_v line of flight. As the π_v decays close to the end of the hadronic calorimeter (4 m), the average number of muon RoI's contained in the cone increases rapidly due to the charged tracks from the π_v decay passing through the calorimeter and entering the muon spectrometer. Once the π_v decay is inside

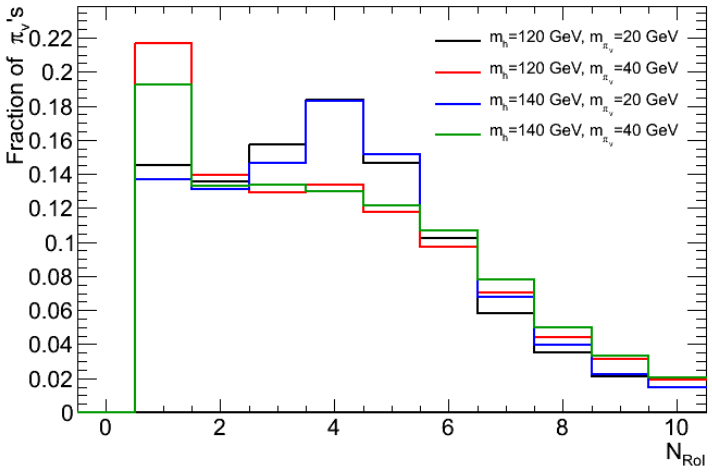

Figure 5.3: The total number of RoI's found in events with a π_v decaying inside the barrel muon spectrometer.

the spectrometer, the number of RoI's remains approximately constant until the π_v decays close to the muon trigger plane (7 m), at which point the charged hadrons are not spatially separated enough to give multiple, unique RoI's. Decays occurring beyond the first trigger plane do not give RoI's because hits are required in both the first and second trigger planes. The few RoI's from decays beyond 7 m are due to low momentum curling tracks from the π_v decay.

5.1.1 The Muon RoI Cluster Trigger

The cluster of muon RoI's provides a characteristic signature that can be used in the HLT to select events with π_v's decaying inside the muon spectrometer. By requiring a cluster containing at least three muon RoI's at Level 2, it is possible to trigger on such displaced decays with high efficiency. The backgrounds of punch-through and muon bremsstrahlung can be suppressed by requiring the that RoI cluster be isolated with respect to both calorimeter jets and inner detector tracks. Figure 5.5 (Left) shows the fraction of events accepted as a function of ΔR between the nearest jet and the center of the RoI clusters in signal events. For all of the signal samples considered, the acceptance is relatively constant up to values of $\Delta R \sim 0.7$. Requiring that the muon RoI cluster be isolated from

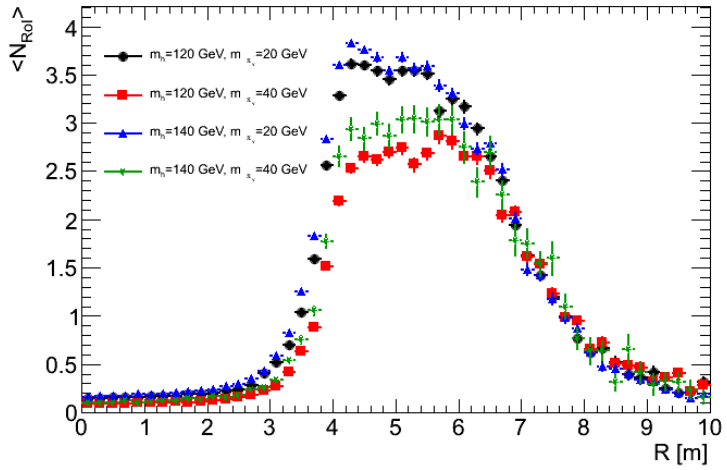

Figure 5.4: Average number of Level 1 muon RoI's in cone of $\Delta R = 0.4$ around the π_v line of flight as a function of the π_v radial decay distance.

jets, within $\Delta R \leq 0.7$, results in a loss of signal of less than $\sim$2%. It should be noted that the RoI cluster is only required to be isolated with respect to jets that have $\log_{10}(E_{HAD}/E_{EM}) \leq 0.5$. This is done to increase the signal efficiency for events in which the π_v decays at the end of the calorimeter, depositing energy and thus producing both a jet (with only hadronic energy) and a muon RoI cluster.

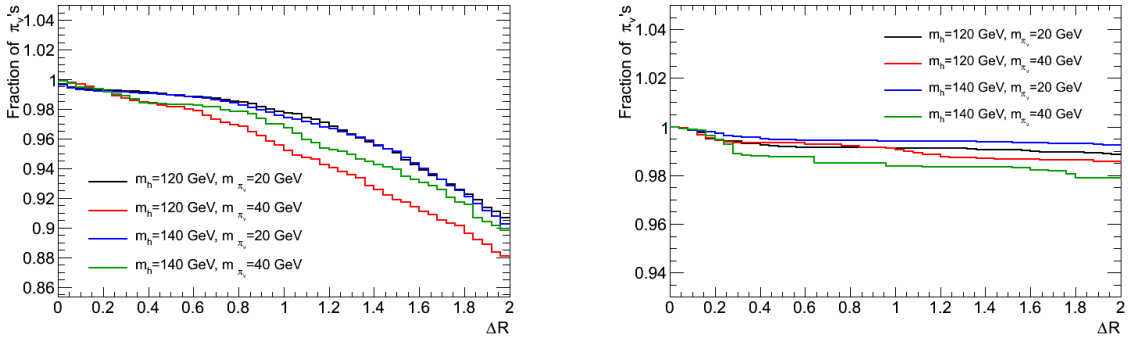

Figure 5.5: Fraction of RoI Clusters accepted in signal events as a function of ΔR between the center of the RoI Cluster and jets (Left) and tracks (Right).

QCD backgrounds can be further suppressed by also imposing isolation with respect to inner detector tracks. Figure 5.5 (Right) shows the fraction of events accepted as a function of ΔR between the center of the RoI cluster and the nearest inner detector track (reconstructed by the Level 2 algorithm, SiTrack [33]) with $p_{\mathrm{T}} > 5$ GeV. Because the π_v's are both long lived, we do not expect many high p_{T} tracks to be reconstructed in the inner detector, thus the acceptance is flat across a wide range in ΔR. Requiring isolation within a region of $\Delta\mathrm{R} \leq 0.4$ results in a loss of less than $\sim$1% in all of the signal samples.

5.1.2 Implementation of the RoI Cluster Trigger

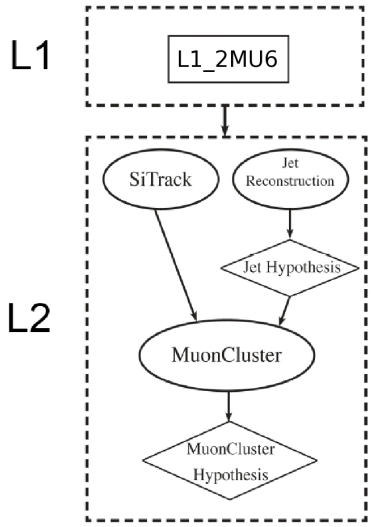

Figure 5.6: Schematic diagram of the Hidden Valley Muon RoI Cluster trigger. The ovals and diamonds represent the Feature Extraction and Hypothesis algorithms, respectively.

The schematic diagram for the sequence of algorithms used in the Muon RoI Cluster trigger is shown in Figure 5.6. The Level 1 muon trigger L1_2MU6 is used to seed the Level 2 trigger. The Muon RoI Cluster Fex[3] algorithm starts by finding the ΔR = 0.4 cone that contains the maximum number of muon RoI's. Then it finds all jets with $E_{\mathrm{T}} \geq 35$ GeV with $\log_{10}(\mathrm{E_{HAD}}/\mathrm{E_{EM}}) \leq 0.5$ in the

[3]The Fex (Feature EXtraction) algorithms compute the features of the object associated with the Level 1 RoI. These features are subsequently compared against selection criteria in the Hypothesis (Hypo) algorithms.

range $\mid \eta \mid < 2.5$ within a cone of $\Delta R \leq 0.7$ around the cluster center. Next the Fex computes the number of inner detector tracks with $p_T > 5$ GeV in a $(\Delta\eta \times \Delta\phi)$ region of (0.2×0.2) around the RoI cluster center. The Hypothesis algorithm requires that the cluster contain at least three muon RoI's and there be no jets or tracks in the regions defined above. There are no additional requirements imposed at the Event Filter.

The Muon RoI Cluster trigger has only been implemented in the barrel portion of the muon spectrometer ($\mid \eta \mid < 1$) due to rate problems in the endcap spectrometer ($1 \leq \mid \eta \mid \leq 2.5$). At an instantaneous luminosity of $10^{33}\text{cm}^{-2}\text{s}^{-1}$, beam halo produces fake triggers in the endcap at a rate of $\sim$2 Hz, which exceeds the total allowed bandwidth for new trigger objects. Therefore, the trigger cannot be used in the endcap spectrometer.

5.1.3 Trigger Timing Issues

The distribution of β_{π_v}, Figure 4.4, shows that π_v's in our signal samples typically have $\beta \geq 0.7$. The important issue is to ensure that the Muon RoI Cluster Trigger is associated with the correct bunch crossing. The critical parameter to examine is the time delay of a trigger coming from a π_v with respect to a trigger arising from a $\beta \simeq 1$ particle originating from the IP in the same interaction that produced the π_v. The hadrons from the π_v decay will have $\beta \simeq 1$, thus in determining the time delay (Δt) between the π_v trigger and a $\beta \simeq 1$ particle from the IP, only the path length of the π_v from the IP to the decay position needs to be considered.

The Δt shifts for the benchmark points are shown in Figure 5.7 as a function of the π_v proper lifetime, for π_v's decaying inside the barrel muon spectrometer. As the proper lifetime increases, the fraction of π_v's that arrive late increases until the proper lifetime is on the order of the detector dimensions. This is because when the lifetime is small compared to the detector dimensions, only very boosted π_v's have non-negligible probability to decay inside the spectrometer. As the lifetime increases, those π_v's with a smaller boost begin to have some probability to decay inside the muon system, until the lifetime becomes on the order of the detector dimensions, when all π_v's have roughly equal probability to decay inside the spectrometer.

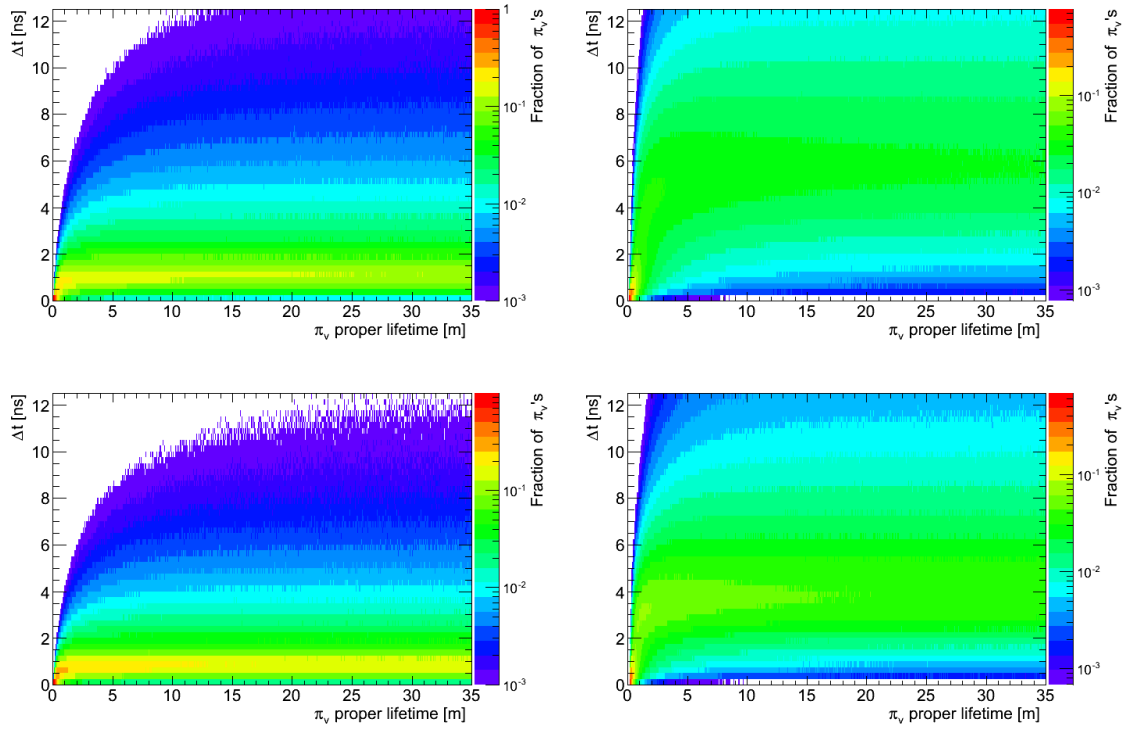

Figure 5.7: The Δt for a π_v decaying in the muon spectrometer as a function of the π_v proper lifetime for each of the four signal Monte Carlos. Top Left: m_h = 120 GeV, m_{π_v} = 20 GeV, Top Right: m_h = 120 GeV, m_{π_v} = 40 GeV, Bottom Left: m_h = 140 GeV, m_{π_v} = 20 GeV, Bottom Right:m_h = 140 GeV, m_{π_v} = 40 GeV

It is important to compare these expected time shifts with the acceptance window of the Level 1 muon triggers. The current configuration of the muon trigger is centered on the bunch crossing, so that the trigger is active for 12.5 ns before and 12.5 ns following the interaction. Using this timing window, the efficiency of the trigger has been measured as a function of the delay time (Δt) with the H8 test beam [54]. Figure 5.8 shows that the muon trigger is ∼100% efficient for time delays of less than approximately 6 ns. Absent errors in timing calibrations, time delays beyond this will result in some of the triggers being associated with the next bunch crossing in a predictable Gaussian manner. If the trigger signal from the π_v is not associated to the correct bunch crossing, then the event cannot be used in the analysis, as the analysis requires a coincidence between signatures. Figure 5.9 shows

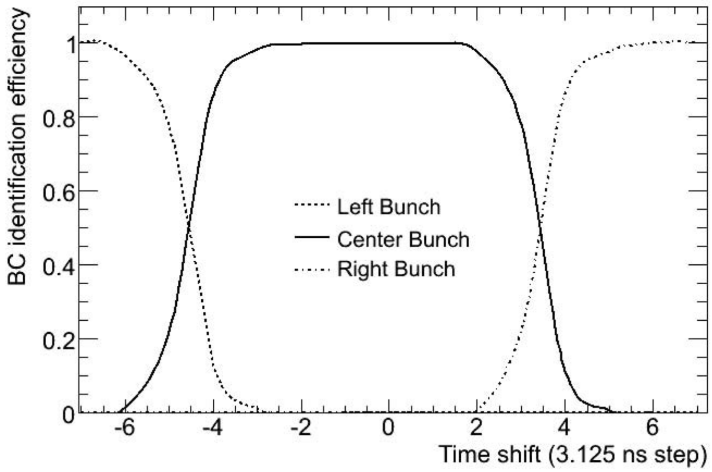

Figure 5.8: Efficiency of correctly associating the low p_{T} muon trigger with the correct bunch crossing as a function of the signal delay; one unit of time shift corresponds to 3.125 ns (From [54]).

the fraction of π_v's decaying in the muon spectrometer that produce a trigger associated with the correct bunch crossing as a function of the π_v proper lifetime. In all the signal samples considered, the π_v is associated with the correct bunch crossing with an efficiency of greater than 70% over the entire range of lifetimes, except in the case where m_{h^0} = 120 GeV and m_{π_v} = 40 GeV, where the average boost of the π_v is much lower (see Figure 4.5).

5.1.4 Trigger Efficiency

In order to satisfy the Muon RoI Cluster trigger, the jets from the π_v decay must enter adjacent sectors of the muon spectrometer. This is because the Level 1 muon firmware is configured to report only the two highest p_{T} RoI's per sector. Therefore, any decay topology in which both jets from the π_v decay are contained in the same sector (when they traverse the trigger plane) will not produce enough RoI's to satisfy the RoI Cluster trigger. Figure 5.10 shows the fraction of π_v's, as a function of the radial decay position, which produce jets that enter two adjacent sectors of the muon spectrometer and provides an estimate of the maximum efficiency for the trigger.

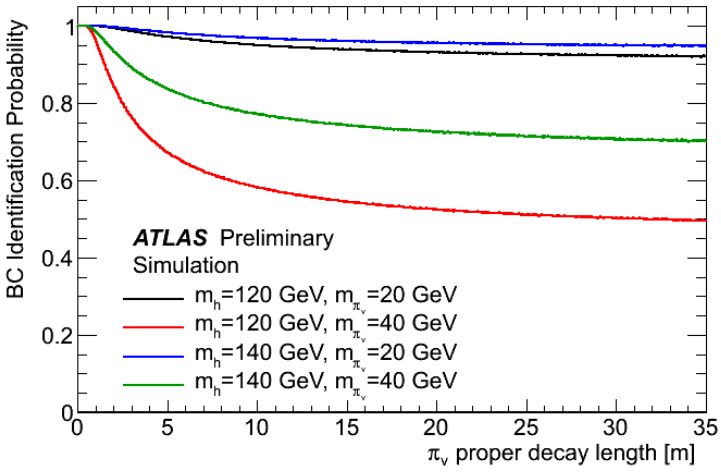

Figure 5.9: Probability that π_v's decaying in the muon spectrometer produce a trigger associated with the correct bunch crossing as a function of the π_v proper lifetime.

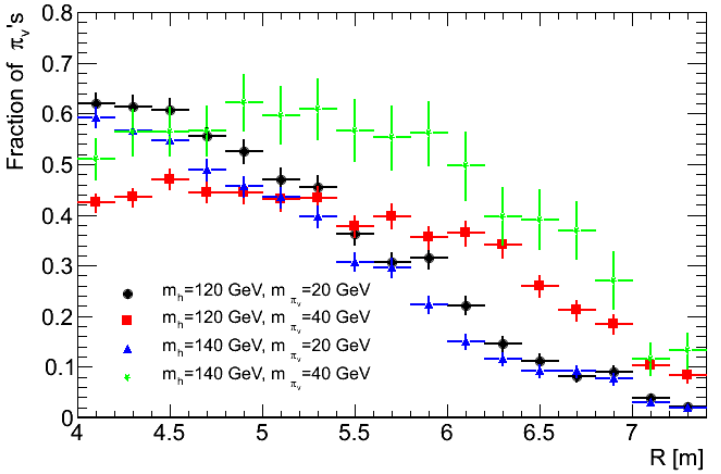

Figure 5.10: The fraction of π_v's which result in jets traversing two adjacent sectors (measured at the trigger plane) of the muon spectrometer, as a function of the π_v radial decay position.

The trigger efficiency is defined as the fraction of π_v's decaying at a distance R that pass the Muon RoI Cluster trigger. Figure 5.11 shows that the Muon RoI Cluster trigger is ∼30-50% effi-

cient from the end of the hadronic calorimeter (4 m) to ∼6 m. The efficiency drops beyond a radial distance of 6 m because the jets originating from the π_v decay do not sufficiently separate before reaching the first muon trigger plane (7 m).

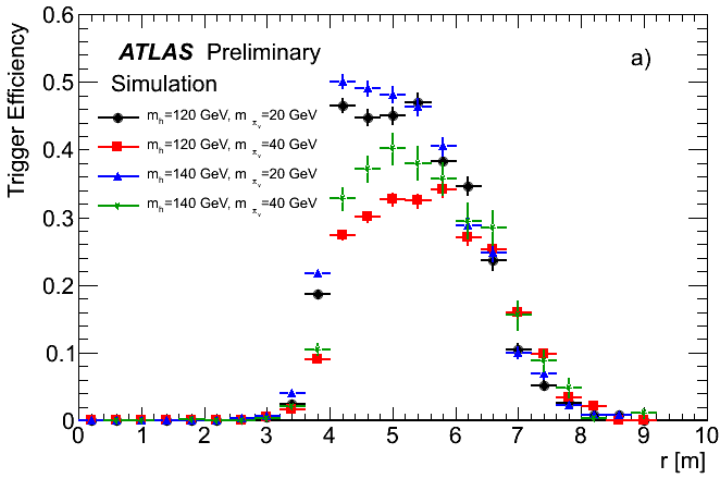

Figure 5.11: Efficiency for the Muon RoI Cluster trigger as a function of the π_v decay position, for decays in the barrel ($|\eta| < 1$)

The mass point, m_{h^0} = 120 GeV and m_{π_v} = 40 GeV, has a lower efficiency, with respect to the other Monte Carlo mass points, due to a combination of trigger timing and kinematics. As can be seen in Figure 5.9, a large fraction of π_v's from this mass point arrive in the muon spectrometer with a significant time delay, which reduces the number of RoI's produced. In addition to fewer total RoI's (Figure 5.3), the RoI's that are produced in the event do not lie along the π_v line of flight (Figure 5.4), but are more spread out. These factors result in a reduced number of RoI clusters found that contain at least 3 RoI's and leads to an overall lower trigger efficiency.

5.1.5 Performance on Data

The 1.94 fb^{-1} data set used in this analysis contains a total of $\sim 1.58 \times 10^6$ events passing the RoI cluster trigger. The (η,ϕ) distribution of these events is shown in Figure 5.12. The relatively low occupancy at $\eta \sim 0$ is due to a small gap in the RPC trigger coverage at $\eta = 0$ and the low occupancies

near $\phi \sim$ -1 and -2 are due to the presence of the MS feet. The slight increase in the number of triggers around $\eta \sim$ -0.8 and $\phi \sim 0$ is the from the beam halo, which predominately occurs in this plane.

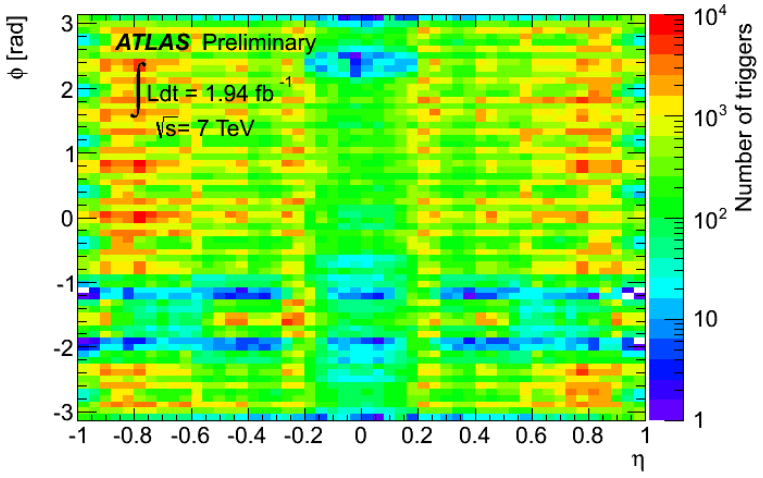

Figure 5.12: Location, in (η,ϕ), of the RoI Cluster for all RoI Clusters in 1.94 fb^{-1} of 2011 Data.

5.1.6 The Muon RoI Cluster Trigger: Systematic Uncertainty

To validate that the Muon RoI Cluster is performing as expected both in Data and Monte Carlo, the trigger is divided into its individual parts and for each part a comparison between Data and Monte Carlo is made.

The most important part of the Muon RoI Cluster is the cluster of muon RoI's that are produced in the spectrometer as a result of the π_v decay. To compare the response of the spectrometer, and its trigger system, to hadrons and photons, a sample of jets that punch-through[4] the calorimeter is used. These punch-through jets, which contain both low p_{T} photons and charged hadrons that traverse a narrow region of the spectrometer reproduce well the environment of a π_v decay. The candidate punch-through jets are selected from events which pass a single jet trigger, and are required to be in

[4]A punch-through jet occurs when particles from the jet, or from the shower in the calorimeter, escapes the calorimeter volume.

the barrel region ($|\eta| < 1.5$) and contain a minimum of 300 MDT hits in a $\Delta R = 0.6$ cone centered around the jet axis. To verify the jet was produced in the collision and not machine or cosmic related noise, the jet is required to contain at least four tracks with $p_T > 1$ GeV in the inner detector. Further, missing energy of at least 20 GeV is required to point in the direction of the jet to ensure the jet punched-through the calorimeter causing its energy to be measured low. Each punch-through jet that produces at least one muon RoI in a cone of $\Delta R = 1$, centered around jet axis, is then processed by the clustering algorithm used by the Muon RoI Cluster trigger. Figure 5.13 shows the number of muon RoI's contained in the cluster for both Data and Monte Carlo.

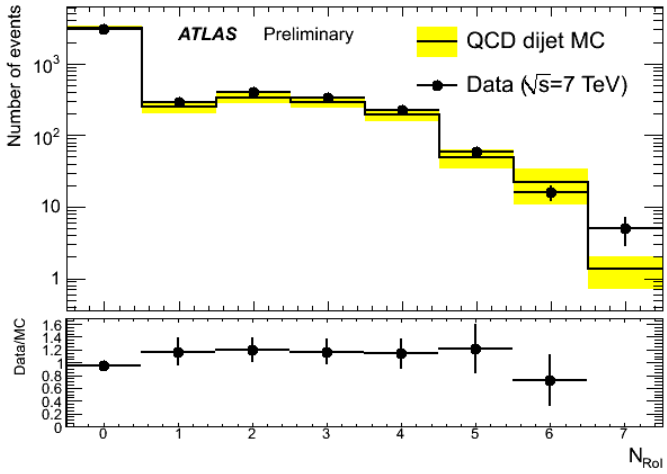

Figure 5.13: The number of Level 1 muon RoI's, from punch-through jets, contained in the Muon RoI Cluster for both Data and Monte Carlo.

Fitting the ratio of data to Monte Carlo, in the region $N_{RoI} \geq 1$, yields a constant of 1.14 ± 0.09. The fit is consistent with one; therefore, the scale factor between data and Monte Carlo is taken to be one and the difference from one, 14%, is taken to be the systematic uncertainty on the RoI cluster.

The RoI Cluster trigger also makes use of the standard Level 2 tracking and jet finding algorithms. Both of these algorithms have been studied in detail by the trigger group [55], and the Monte Carlo has been tuned to reproduce the data. Figure 5.14 shows the Level 2 jet energy for

both Data and Monte Carlo, which agree very well even in the tails of the distribution.

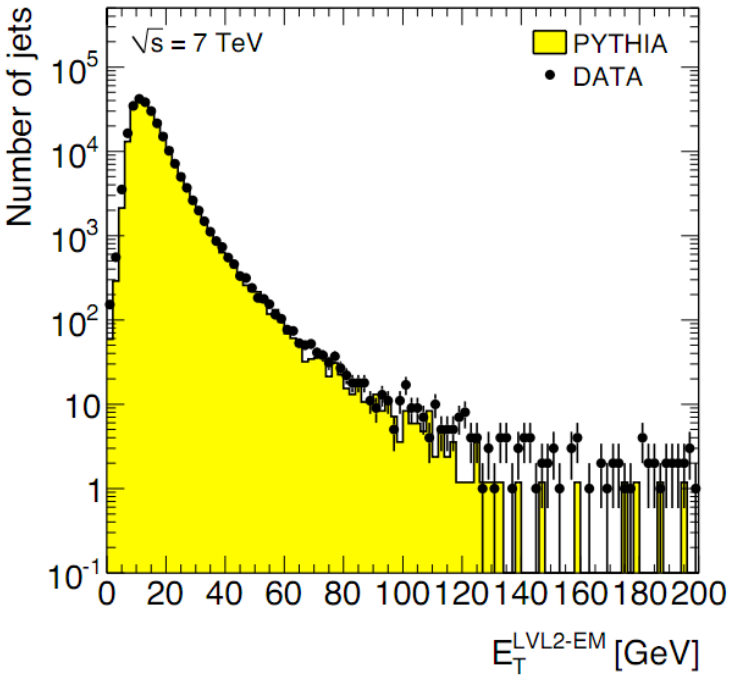

Figure 5.14: E_{T} distribution for Level 2 jets at the EM-scale.

To understand the affects of the JES uncertainty [56] on the isolation requirement, the jet energy cut is varied by 5%, which is the JES uncertainty for jets in the energy range of interest. The resulting change in trigger efficiency is less than 1% in all four signal Monte Carlo samples. The pileup effects have been studied by removing the pileup reweighting tool, which effectively increases the amount of pileup in the signal samples. By comparing the unreweighted and reweighted samples, a trigger efficiency systematic uncertainity of less than one percent is found for each of the Monte Carlo signal samples. From [57], the ISR in gluon fusion produced Higgs can vary the p_{T} of the Higgs by 5%, which implies that the ISR p_{T} spectrum will also vary by 5%. This variation in jet p_{T} leads to a change in the trigger efficiency of less than 1% in all four signal Monte Carlo samples. The small effects due to these uncertainties, are due to the relatively few number of events with a jet, from ISR or pileup, with energy above the isolation cut (Figure 5.15). Therefore, the dominant uncertainty in

the trigger algorithm is the cluster of muon RoI's, and the systematic uncertainty is taken to be 14%, the sum (in quadrature) of all the uncertainties.

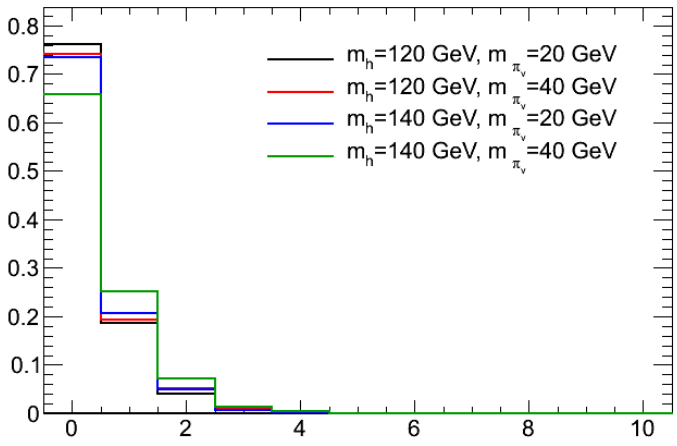

Figure 5.15: The number of jets, found by Level 2 jet reconstruction, with $E_{\mathrm{T}} > 35$ GeV and $\mid \eta \mid < 1.7$. Jets with $\mid \eta \mid > 1.7$ are beyond the range in which jets could spoil the isolation requirements of the RoI Cluster trigger.

5.2 Decays in the Hadronic Calorimeter

Decays that occur toward the end of the electromagnetic or inside of the hadronic calorimeter will deposit most of their energy in the hadronic calorimeter. Jets from Standard Model processes will originate from the IP, and will therefore deposit energy in both the electromagnetic and hadronic calorimeter. This suggests that the ratio of energy deposited in the hadronic calorimeter to that deposited in the electromagnetic calorimeter can be used to select jets from decays occurring inside the calorimeter. Figure 5.16 shows a simulated event with a π_v decaying inside the hadronic calorimeter, where there is a large energy deposit, while electromagnetic calorimeter records little to no energy. Furthermore, the event display shows a second characteristic of this topology, no tracks connecting the jet to the IP. This is expected because the neutral π_v has traveled through the tracking volume without interacting before decaying to a $b\bar{b}$ inside of the calorimeter. Because the $b\bar{b}$ pair is created inside of the calorimeter, they do not have time to spatially separate before depositing their energy

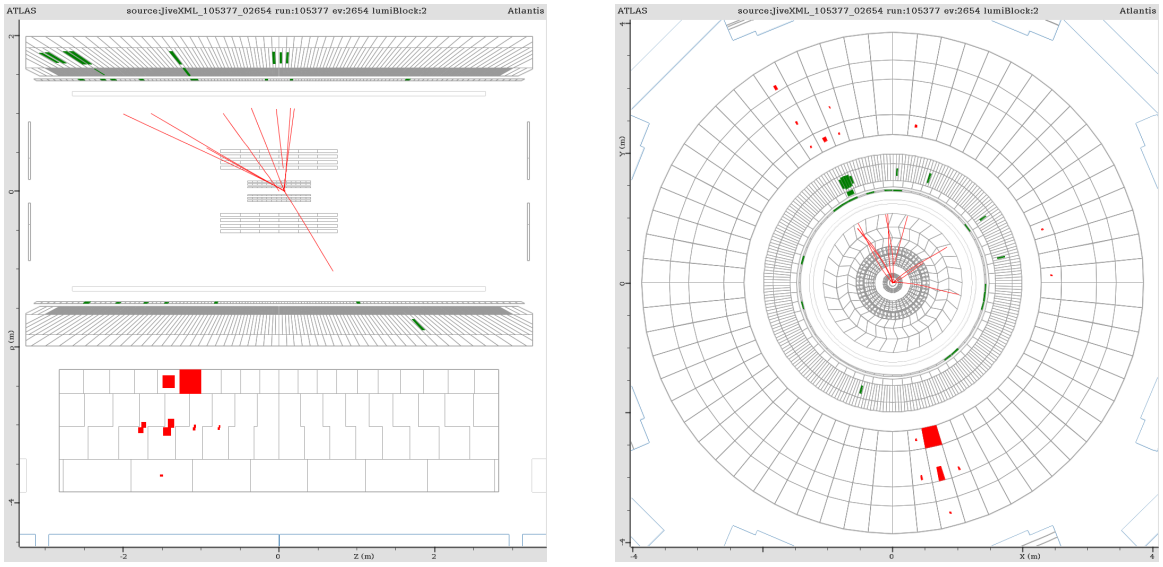

Figure 5.16: Event display of a showing typical signatures of a π_v decaying inside the barrel hadronic calorimeter. Energy deposits in the hadronic calorimeter are shown in red and energy in the electromagnetic calorimeter are shown in green. Right: Longitudinal view, Left: Transverse view

in the calorimeter, which leads to a very narrow jet being produced. As can been seen in Figure 5.17, almost all of the energy from jets originating inside the hadronic calorimeter is contained within a cone of $\Delta R = 0.1$ around the jet axis.

5.2.1 The Calorimeter Ratio Trigger

The Level 1 tau triggers select jets with energy contained in a ($\Delta\eta \times \Delta\phi$) region of (0.2×0.2), which naturally selects narrow jets, such as those produced when a π_v decays inside the hadronic calorimeter. The tau triggers also have a lower energy threshold, with respect to jet triggers, which increases the signal efficiency without increasing the amount of QCD background accepted. Figure 5.18 shows the logarithm (base 10) of the hadronic to electromagnetic energy ratio for jets from π_v decays as a function of the π_v decay position. As the π_v decays close to the end of the electromagnetic calorimeter (2200 mm), the ratio changes from a characteristic negative to a positive value. The value of $\log_{10}(E_{HAD}/E_{EM})$ plateaus at ∼1.5 until ∼3600 mm, at which point the π_v decay occurs too close to the end of the hadronic calorimeter (4250 mm) to accurately measure the jet energy, which causes the value of $\log_{10}(E_{HAD}/E_{EM})$ to decrease.

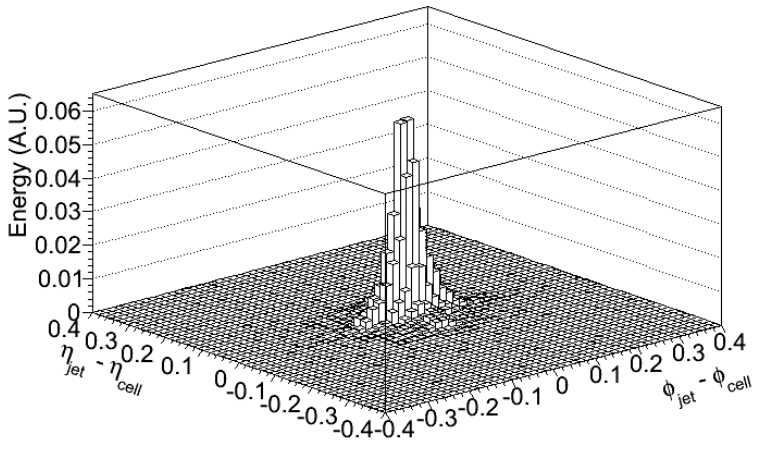

Figure 5.17: Lego plot of the energy deposition in the calorimeter cells around the jet axis (0,0,0) for π_v's decaying in the hadronic calorimeter.

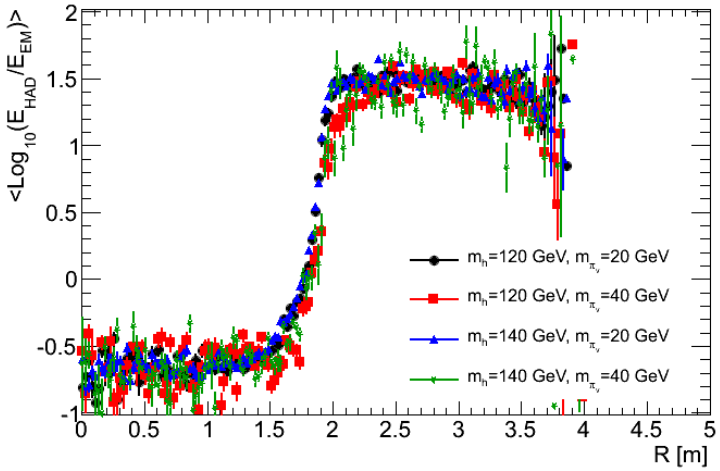

Figure 5.18: Mean value of $\log_{10}(E_{HAD}/E_{EM})$ for all jets in the barrel calorimeter coming from π_v decays as a function of the π_v radial decay distance.

If $\log_{10}(E_{HAD}/E_{EM})$ is plotted for each jet located inside of a L1_TAU30 RoI, two distributions are clearly present, see Figure 5.19. The distribution centered at ∼-1 is from π_v decays inside the

inner detector or electromagnetic calorimeter, while the second distribution, centered at ∼1.5, is from π_v decays inside the hadronic calorimeter.

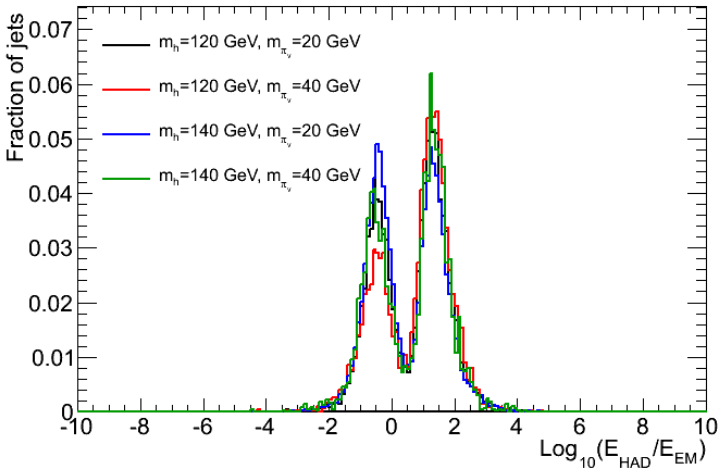

Figure 5.19: Distribution of $\log_{10}(E_{HAD}/E_{EM})$ for all jets in the barrel region ($\mid \eta \mid < 1.4$) inside of Level 1 tau RoI's

Because jets with $\log_{10}(E_{HAD}/E_{EM})\geq 1$ are produced by π_v's decaying in the calorimeter, the inner detector should not contain any tracks pointing at signal jet. Using the Level 2 tracking algorithm, SiTrack, greater than 95% of jets with $\log_{10}(E_{HAD}/E_{EM})\geq 1$ have zero tracks with $p_{\mathrm{T}} > 1$ GeV reconstructed in a region of (0.2×0.2) in $(\Delta\eta\times\Delta\phi)$ around the jet axis, as shown in Figure 5.20.

5.2.2 Implementation of the Calorimeter Ratio Trigger

The schematic diagram for the sequence of algorithms used for the Calorimeter Ratio trigger is shown in Figure 5.21. The trigger starts from the Level 1 tau trigger, L1_TAU30. This Level 1 tau RoI is then used to seed the Level 2 jet finding and SiTrack algorithms. The decision to accept the event is made by the Hypothesis algorithm, which is a modified version of the standard Level 2 jet Hypothesis. The event is accepted by the Hypothesis algorithm if the jet satisfies: $E_T \geq 35$ GeV, $\mid \eta \mid < 2.5$, $\log_{10}(E_{HAD}/E_{EM})\geq 1$ and no ID tracks with $p_{\mathrm{T}} > 1$ GeV in a $(\Delta\eta\times\Delta\phi)$ region of

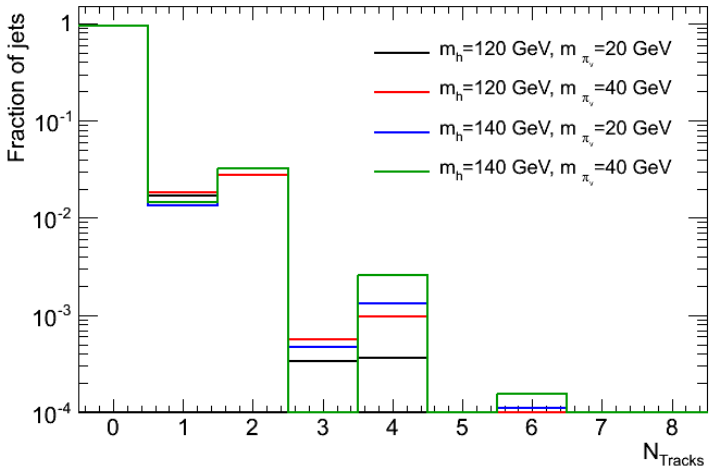

Figure 5.20: Number of tracks reconstructed using the Level 2 tracking algorithm SiTrack with $p_T > 1$ GeV in a region of $(\Delta\eta \times \Delta\phi)$ of (0.2×0.2) around the jet axis, for jets with $\log_{10}(E_{HAD}/E_{EM}) \geq 1$

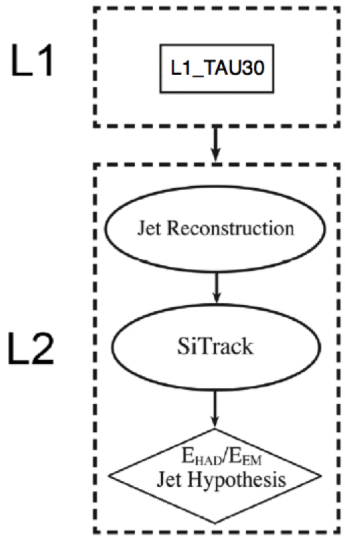

Figure 5.21: Schematic diagram of the algorithms used in the Calorimeter Ratio Trigger. The ovals and diamonds represent the Feature Extraction and Hypothesis algorithms, respectively.

(0.2×0.2) around the jet direction. At the Event Filter, a standard jet algorithm is used and the jet is required to have $E_{\mathrm{T}} > 35$ GeV.

5.2.3 Trigger Timing Issues

Figure 4.4 shows that a majority of π_v's in our signal samples have $\beta \geq 0.7$. The calorimeter samples the energy only once, at the expected peak signal, for use by the trigger. This implies that π_v's decaying late will have a poorly measured, lower energy which will lead to a lower acceptance. Figure 5.22 shows the distribution of time delays, Δt, between π_v's decaying in the hadronic calorimeter and a particle produced in the same interaction traveling with $\beta \simeq 1$. The π_v's that decay within $\sim$3 ns

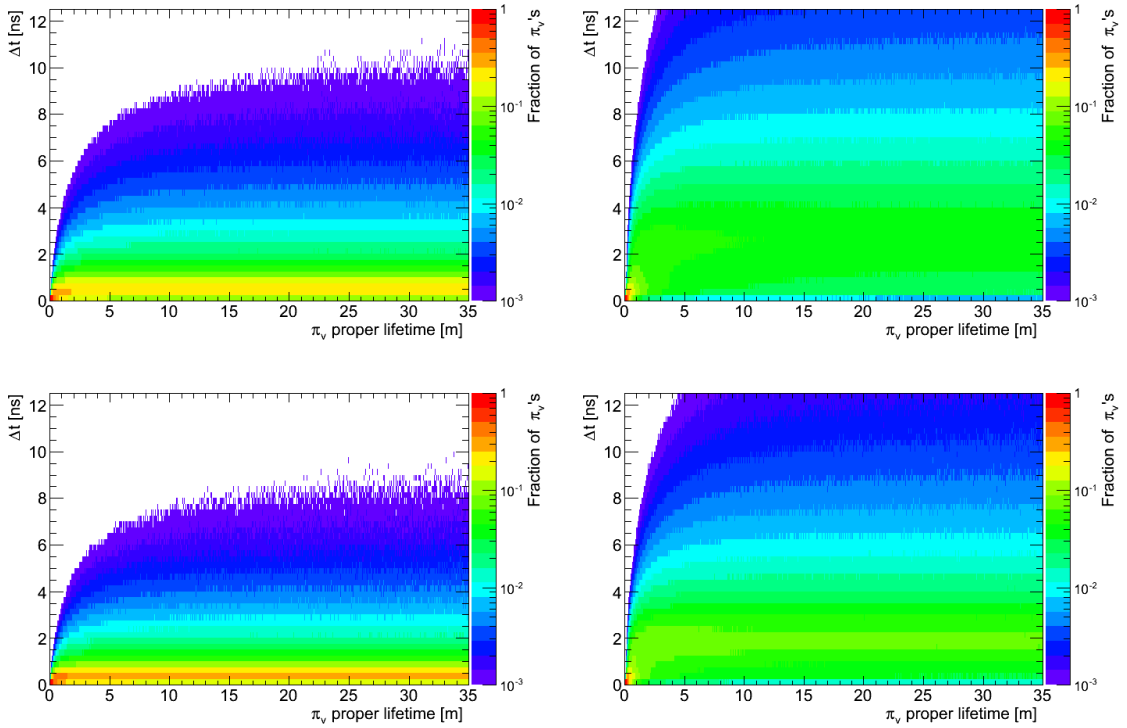

Figure 5.22: The Δt for a π_v decaying in the hadronic calorimeter as a function of the π_v proper lifetime for each of the four signal Monte Carlos. Top Left: m_h = 120 GeV, m_{π_v} = 20 GeV, Top Right: m_h = 120 GeV, m_{π_v} = 40 GeV, Bottom Left: m_h = 140 GeV, m_{π_v} = 20 GeV, Bottom Right:m_h = 140 GeV, m_{π_v} = 40 GeV

of the expected ($\beta \simeq 1$) signal will not have a significant degradation in the measurement of the jet energy by the trigger system. As can be seen in Figure 5.23, more than 80% of π_v's arrive in the hadronic calorimeter with a Δt of less than 3 ns for all lifetimes considered, except in the case where m_h = 120 GeV and m_{π_v} = 40 GeV, where the average boost of the π_v is much lower (see Figure 4.5).

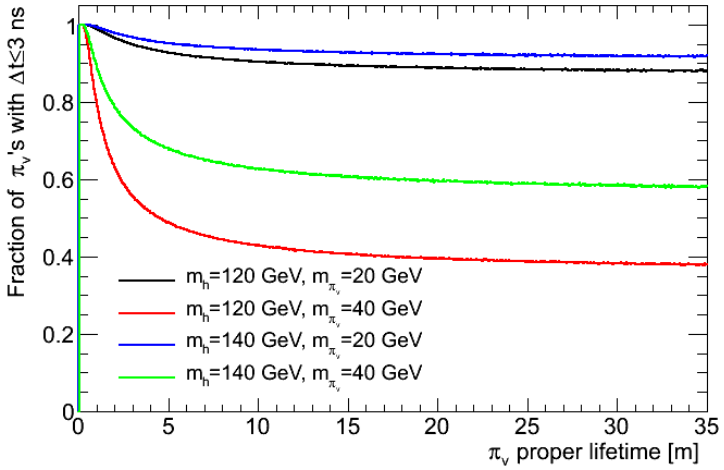

Figure 5.23: Fraction of π_v's that decay in the hadronic calorimeter with a delay of $\Delta t \leq 3$ ns as a function of the π_v proper lifetime

5.2.4 Trigger Efficiency

The trigger efficiency is defined as as the fraction of π_v's that decay a distance L from the Interaction Point that pass the Calorimeter Ratio Trigger. Figure 5.24 (Left) shows that this trigger is ~40-60% efficient for π_v's decaying inside the barrel ($|\eta| < 1.4$) hadronic calorimeter, and Figure 5.24 (Right) shows the trigger is ~10-20% efficient for π_v's decaying inside the endcap ($1.5 < |\eta| < 2.5$) hadronic calorimeter. The lower efficiency in the endcap region is due to the presence of the underlying event, which can deposit energy in the electromagnetic calorimeter, spoiling the $\log_{10}(E_{HAD}/E_{EM})$ for the signal jet, and tracks from the underlying event can spoil the request of having zero tracks (with p_T 1 GeV) inside the jet cone.

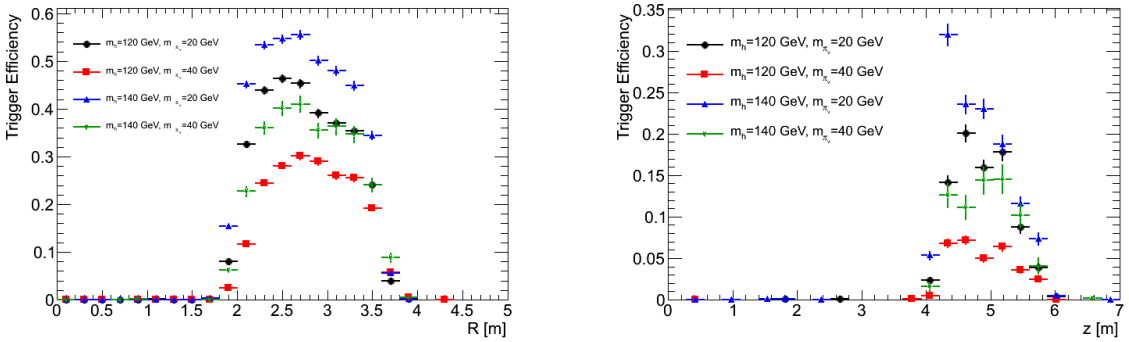

Figure 5.24: Efficiency for the Calorimeter Ratio trigger as a function of the π_v decay position for decays in the barrel, $|\eta| < 1.4$, (Left) and endcap, $1.4 \leq |\eta| < 2.5$ (Right).

5.2.5 Machine Backgrounds

There is a significant background to events that pass the Calorimeter Cluster trigger from beam halo muons which bremsstrahlung inside the hadronic calorimeter. Figure 5.25 shows a typical beam halo triggered event. These events are characterized by a pair of muon segments (purple lines) re-

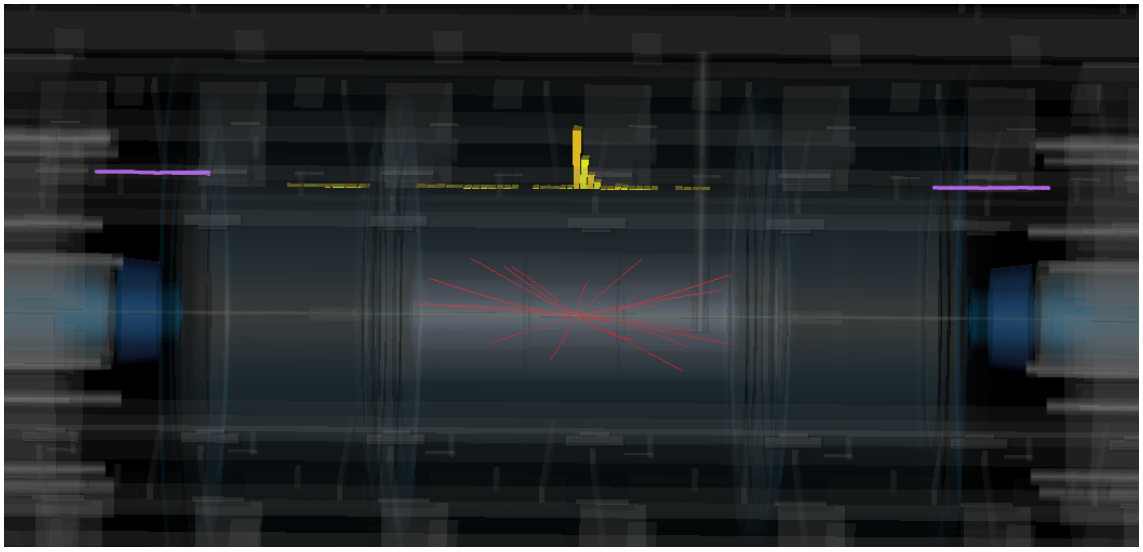

Figure 5.25: Event display showing a beam halo muon which has bremsstrahlunged inside of the hadronic calorimeter and caused the event to pass the Calorimeter Ratio trigger. The two purple lines are reconstructed muon segments and the yellow boxes represent energy deposited in the hadronic calorimeter.

constructed on either side of the detector which are parallel to the z-axis, and a line of calorimeter cells (yellow boxes) extending the length of the calorimeter in line with the jet. Two separate algorithms have been developed to remove these events.

The first algorithm uses the calorimeter cell timing to identify the beam halo track inside the calorimeter and match it to a reconstructed jet. Figure 5.26 shows the calorimeter timing for cells which have been traversed by the beam halo muon. The time, t = 0 ns, corresponds to when a particle produced at the IP during the beam crossing would arrive in the calorimeter cell. The figure shows two distributions super imposed, one for muons traveling from positive z to negative z, and, the second, muons traveling from negative to positive z. Muons enter the calorimeter $\sim$25 ns early and leave approximately in time. This characteristic line of calorimeter cells with cell timing is used reject jets which have come from beam halo muon bremsstrahlung.

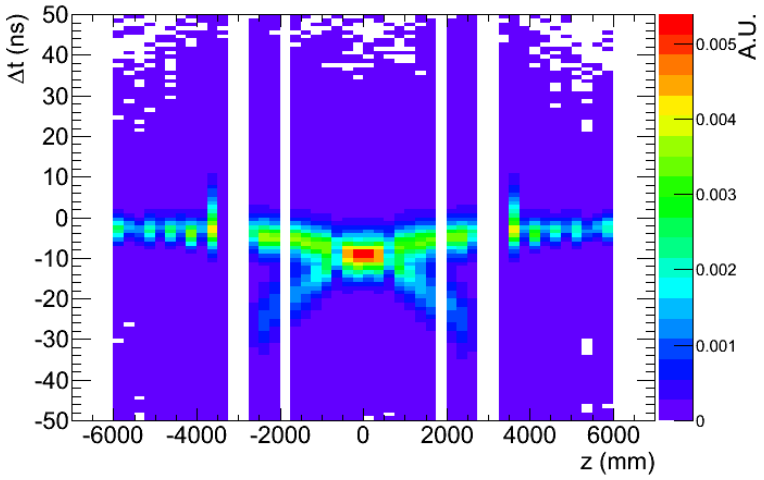

Figure 5.26: Calorimeter cell timing for cells traversed by beam halo muons in events that pass the Calorimeter Ratio trigger. Time t=0 ns corresponds to the expected arrival time of a particle produced at the IP during the bunch crossing.

The second algorithm to reject beam halo events that have passed the Calorimeter Ratio trigger uses the muon segments that are reconstructed. The algorithm requires that a muon segment

be reconstructed on both sides of the detector. A Calorimeter Ratio trigger jet that has two muon segments, one on each side of the detector, which are parallel to the z axis aligned with the jet in phi are rejected as beam halo.

5.2.6 Beam Halo in the Hadronic Calorimeter: Rejection Efficiency

The rejection efficiency of the two beam halo rejection algorithms can be measured using collision data. To make the measurement, one of the algorithms is used to tag the jet as beam halo, and then the second algorithm is applied. The fraction of events that have been selected by both algorithms is taken to be efficiency of the second algorithm. Using this method, the efficiency are measured as:

$$\varepsilon_{Timing} = \text{N(Timing}|\text{Muon Segment)/N(Muon Segment)} = 412954/453825 = (91.0\pm0.2)\%$$
$$\varepsilon_{MuonSegment} = \text{N(Muon Segment}|\text{Timing)/N(Timing)} = 412954/515381 = (80.1\pm0.2)\%$$

The residual contribution of beam halo to the number of events that pass the Calorimeter Ratio trigger can be estimated from the efficiency of both beam halo removal algorithms. The total efficiency, using both algorithms, for removing beam halo triggered events is the probability that either the timing or the muon segment algorithm reject the event, less the overlap between the two algorithms:

$$\varepsilon_{total} = \varepsilon_{Timing} + \varepsilon_{MuonSegment} - \varepsilon_{Timing} * \varepsilon_{MuonSegment}$$

Using the efficiencies calculated above, the total efficiency, ε_{total}, is found to be $(98.2\pm0.4)\%$. Therefore, the residual number of beam halo triggered events is $(1.8\pm0.4)\%$.

5.3 Decays in the Inner Detector and Electromagnetic Calorimeter

Decays that occur beyond the first layers of the Semi-Conductor Tracker (SCT) will produce jets with no reconstructable tracks at Level 2, using the SiTrack algorithm. This produces a very typical signature of highly displaced decays, “trackless jets”. Two examples of this type of event are shown in Figure 5.27. In both events, a π_v has decayed inside the TRT, leaving a visible vertex in the TRT and no tracks connecting to the IP. These jets do not have reconstructable tracks because the current ATLAS HLT tracking algorithms[33] require the formation of tracks seeds built from at least three hits in the pixel detector and one in the first layer of the SCT. These tracking requirements

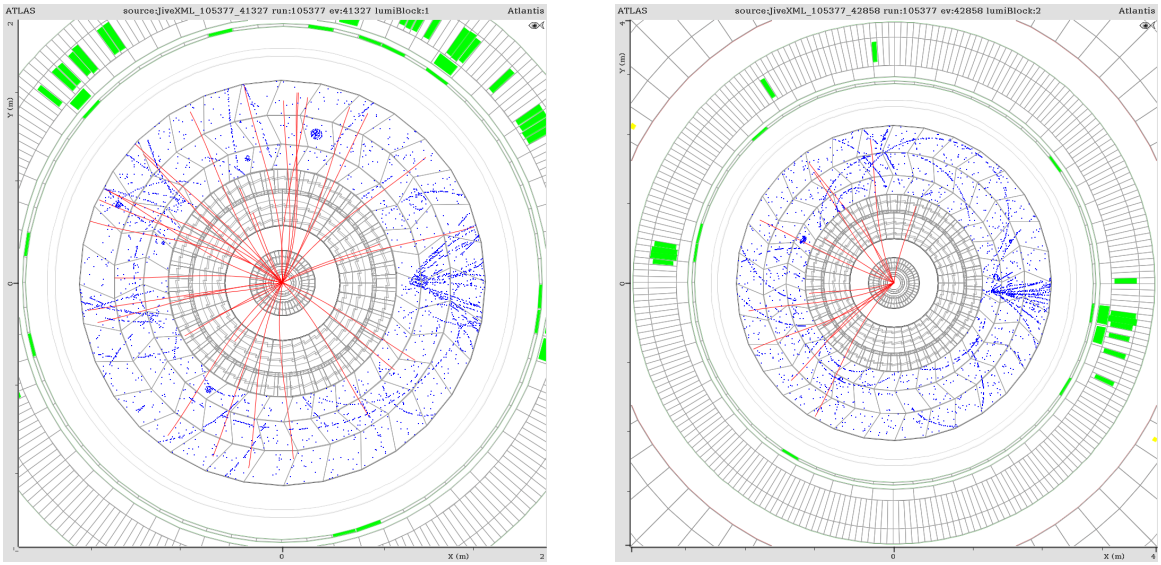

Figure 5.27: Event displays of two different events with a π_v decaying inside the TRT. TRT drift circles are shown in blue, reconstructed tracks are shown in red, and energy deposits in the electromagnetic calorimeter are shown in green.

significantly reduce the efficiency for reconstructing tracks from π_v's which decay beyond the pixel detector. Consequently a large fraction of jets originating from π_v decays have no reconstructed tracks with $p_{\mathrm{T}} > 1$ GeV as can be seen in Figure 5.28.

Those jets that have no reconstructed tracks with $p_{\mathrm{T}} > 1$ GeV in a region of (0.2×0.2) in $(\Delta\eta\times\Delta\phi)$ are referred to as "trackless jets". The trackless jet signature provides a powerful handle for identifying jets from displaced decays; however, tracking is not available until the HLT, so another approach is needed for the event to pass the Level 1 trigger. In case of the signal events, events in which the π_v's decay inside the detector are characterized by 1-2 relatively low energy jets, see Figure 5.29.

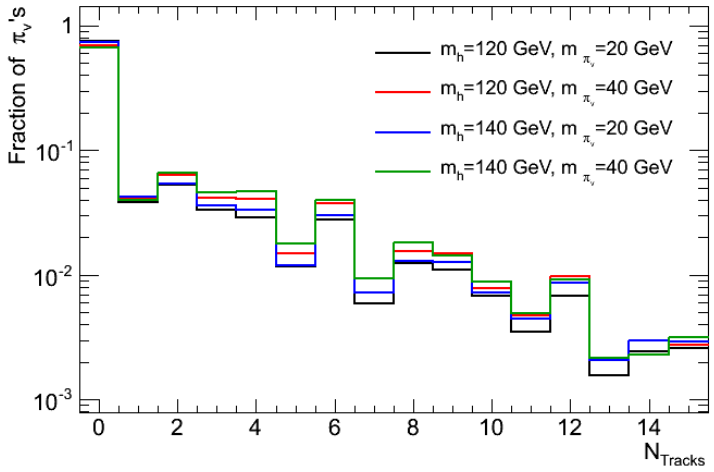

Figure 5.28: Number of reconstructed tracks with $p_T > 1$ GeV associated with each Level 2 jet using the SiTrack tracking algorithm in a $(\Delta\eta \times \Delta\phi)$ region of (0.2×0.2) around the jet axis.

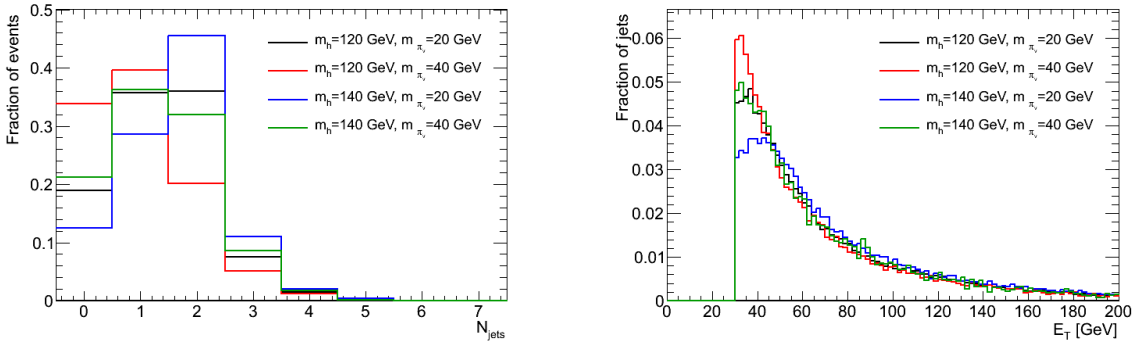

Figure 5.29: Left: Number of jets present in events where both π_v's decay inside the calorimeter volume. Right: E_T of the jets present in events where both π_v's decay inside the calorimeter volume.

5.3.1 The Trackless Jet plus Muon Trigger

Because the jets in the signal events are not very energetic, it is not possible to rely on the Level 1 jet triggers. In order to avoid being swamped by QCD dijets, the unprescaled[5] Level 1 jet trigger

[5]Prescales are applied to triggers to keep the rate low. If a trigger has a prescale of N, then 1 in N events will be accepted by that trigger.

thresholds have been set to moderately high values[6]. Therefore, it is necessary to require something else in the event to pass the Level 1 trigger. In signal events the π_v decays to a $b\bar{b}$ pair which have a combined probability of $\sim$40% to produce a muon. At Level 2, the QCD background to a trackless jet can be significantly reduced by requiring the muon be contained inside of the trackless jet. In QCD jets produced via Standard Model processes, the muon will typically be prompt and thus leave a track in the inner detector, while in π_v events, the muon is produced close to the π_v decay vertex, which can be highly displaced from the IP.

5.3.2 Implementation of the Trackless Jet plus Muon Trigger

The schematic diagram for the sequence of algorithms used in the Trackless Jet plus Muon trigger is shown in Figure 5.30. The trigger starts from the logical AND between the L1_J35 and L1_MU6 items. The L1_J35 trigger is then used to seed the Level 2 jet reconstruction and the Level 2 tracking algorithm, SiTrack. The ID-jet+Muon Fex algorithm then finds the angular separation, in ΔR, between the Level 1 muon RoI and the Level 2 jet. The Hypothesis algorithm then requires that the jet have $E_T > 35$ GeV, no tracks with $p_T > 1$ GeV in the $(\Delta\eta \times \Delta\phi)$ region of (0.2×0.2) around the jet axis and ΔR between the jet and muon RoI be less than 0.4. At the Event Filter, the normal jet algorithm is used and again, the jet is required to have $E_T > 35$ GeV.

5.3.3 Trigger Efficiency

The trigger efficiency is defined as the fraction of π_v's that decay a distance L from the IP that pass the Trackless Jet plus Muon trigger. Figure 5.31 shows the trigger is 5-10% efficient for decays occurring in the region of the barrel between the middle of the inner detector and electromagnetic calorimeter. The trigger efficiency then increases to 20-30% efficient as the decay occurs closer to the end of the hadronic calorimeter. This efficiency can be understood by considering the p_T spectrum of muons produced by the π_v decays, Figure 5.32. A muon originating inside the inner detector will loose, on average, $\sim$4 GeV of energy as it traverses the calorimeters[33]; therefore, a larger fraction of muons produced in π_v decays will make it to the muon system as the π_v decays farther into the calorimeter. The efficiency in the endcap is $\sim$5% throughout the detector volume.

[6] In the trigger menu for an instantaneous luminosity of $L = 10^{33}cm^{-2}s^{-1}$, the lowest unprescaled jet trigger is L1_J75

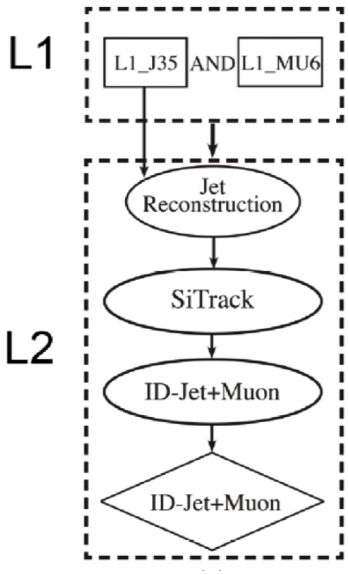

Figure 5.30: Schematic diagram of the Hidden Valley Trackless Jet plus Muon trigger. The ovals and diamonds represent the Feature Extraction and Hypothesis algorithms, respectively.

The low efficiency in the forward region is due to both the low p_{T} muons and increased number of tracks present in the forward region due to the underlying event and pile-up.

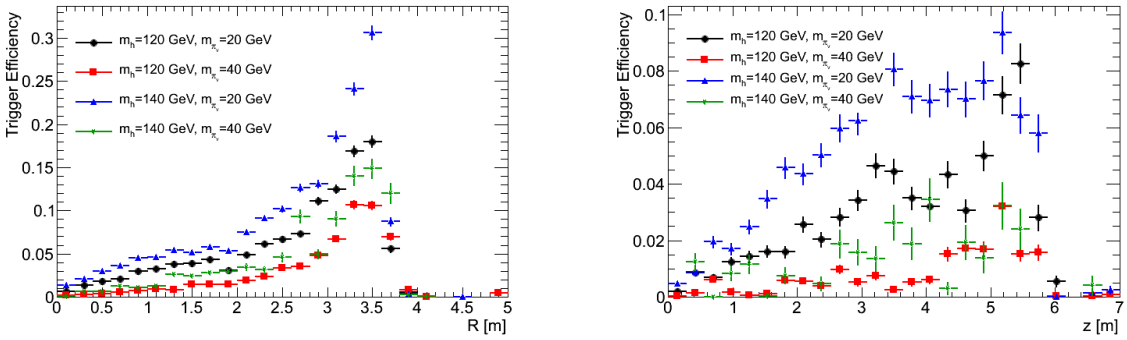

Figure 5.31: Efficiency for the Trackless Jet plus Muon trigger as a function of the π_v decay position for decays in the barrel, $|\eta| < 1.4$, (Left) and endcap, $1.4 < |\eta| < 2.5$, (Right)

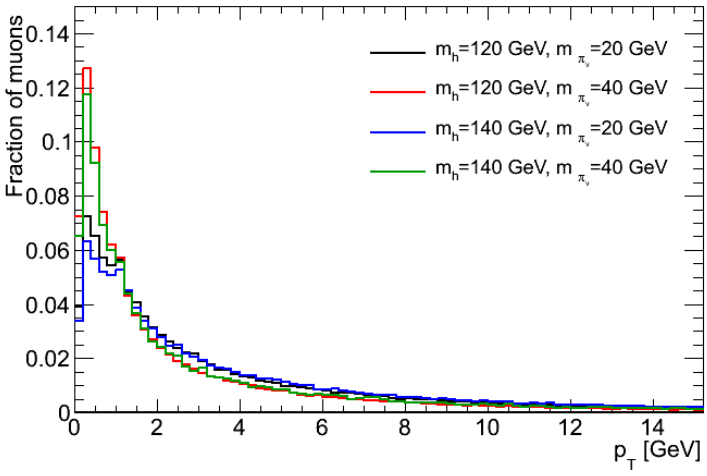

Figure 5.32: p_{T} of muons produced in the decay of π_v's.

5.4 Expected Number of Triggered Events

From the trigger efficiency plots (Figures 5.11, 5.24,and 5.31), it is possible to predict the fraction of Higgs decays that would be accepted by the three Hidden Valley trigger algorithms as a function of the π_v proper lifetime, and assuming a 100% branching fraction for $h^0 \rightarrow \pi_v\pi_v$. In order to make this prediction, one million $h^0 \rightarrow \pi_v\pi_v$ events were generated for a range of lifetimes (from 0 - 25000 mm, in steps of 50 mm). For each lifetime, the fraction of π_v's that decay in each region (as defined in the efficiency plots) is weighted by the corresponding trigger efficiency for that region. The error band is dominated by the uncertainty in the efficiency measurements[7]. Figure 5.33 shows the expected fraction of events that pass each of the three Hidden Valley triggers as a function of lifetime. Events passing the Muon RoI Cluster trigger are required to be associated with the correct bunch crossing, as discussed in 5.1.3.

[7]The statistical uncertainty introduced by the lifetime simulation is $\sim$0.5% and is therefore negligible when compared to the uncertainties in the trigger efficiencies,$\sim$7%

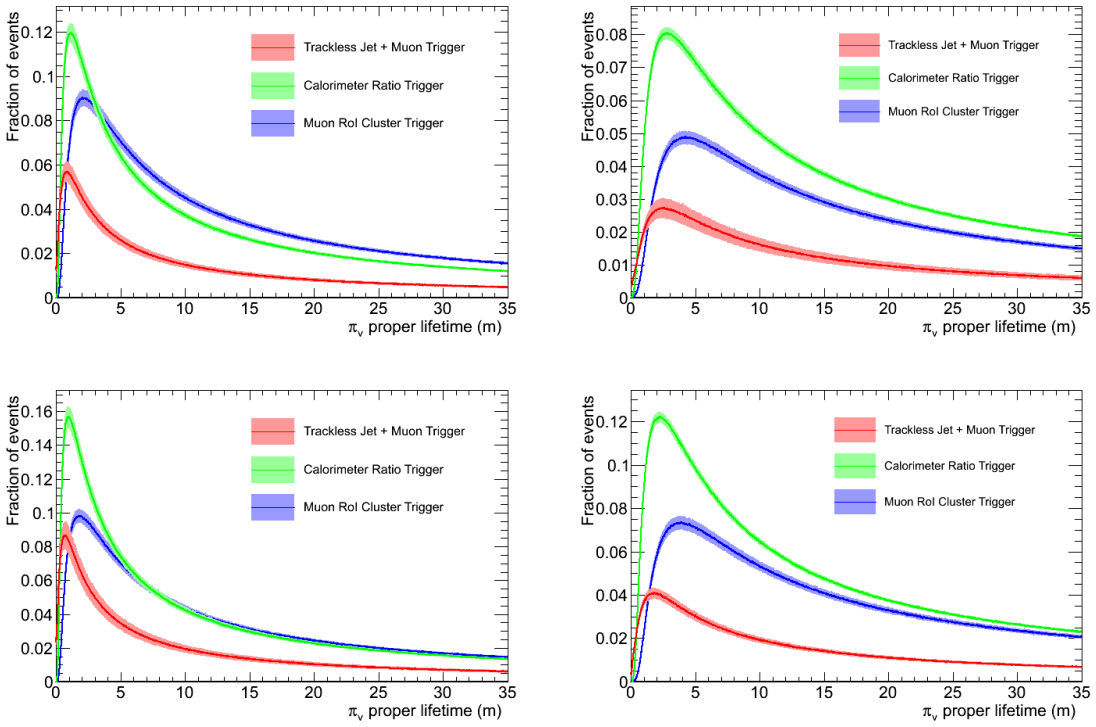

Figure 5.33: The expected fraction of $h^0 \rightarrow \pi_v\pi_v$ that pass one of the Hidden Valley triggers as a function of the π_v proper lifetime for each of the four signal samples. The Error bands represent the 1 σ uncertainty for the total fraction accepted. Top Left: m_h = 120 GeV, m_{π_v} = 20 GeV, Top Right: m_h = 120 GeV, m_{π_v} = 40 GeV, Bottom Left: m_h = 140 GeV, m_{π_v} = 20 GeV, Bottom Right:m_h = 140 GeV, m_{π_v} = 40 GeV

Chapter 6

VERTEX FINDING IN THE MUON SPECTROMETER

Neutral particles with long decay lengths and many particle final states represent, from an experimental point of view, a challenge for the reconstruction capabilities of ATLAS. If the lifetimes are long enough there will be a non negligible number of decays in the muon spectrometer (see Section 5.1). Because the ATLAS muon spectrometer is an "air core" toroid, it allows for track and vertex reconstruction in events with a long-lived particle decaying to low energy hadrons inside the muon spectrometer. Typically the decay of a π_v results in high multiplicity jets of low p_{T} particles produced in a narrow region of the spectrometer (see Figures 4.6 and 4.7). Figure 6.1 shows a typical event with a π_v decaying in the spectrometer and the resultant splash in the MDTs.

6.1 Hadrons and Photons in the Muon Spectrometer

In order to study the behavior of charged hadrons and photons in the spectrometer, two samples of simulated single $\pi^{\pm}$ and π^0 's in the spectrometer, using the full GEANT4[52] simulation have been produced. For these simulations, two separate cases are studied. In the first case, a single $\pi^{\pm}$ (or π^0 with the subsequent decay $\pi^0 \rightarrow \gamma\gamma$) is shot into the middle of the barrel large sectors, where the π traverses only the three muon stations (and associated services). In the second case, the π is shot into the middle of the small sectors, where the π hits the toroid coil in addition to the three muon stations.

First, the properties of the charged pions as they pass through the spectrometer are considered. Figure 6.2 shows the total number of MDT hits resulting from a single $\pi^{\pm}$ produced in the muon spectrometer, with p_T in the range $1 < p_T < 5$ GeV. The black histogram shows the number of hits present when the pion is in the large sectors, while the red histogram shows when the pion is shot into the small sector, where it also traverses the magnet coil. In both cases, the pion leaves $\sim$20

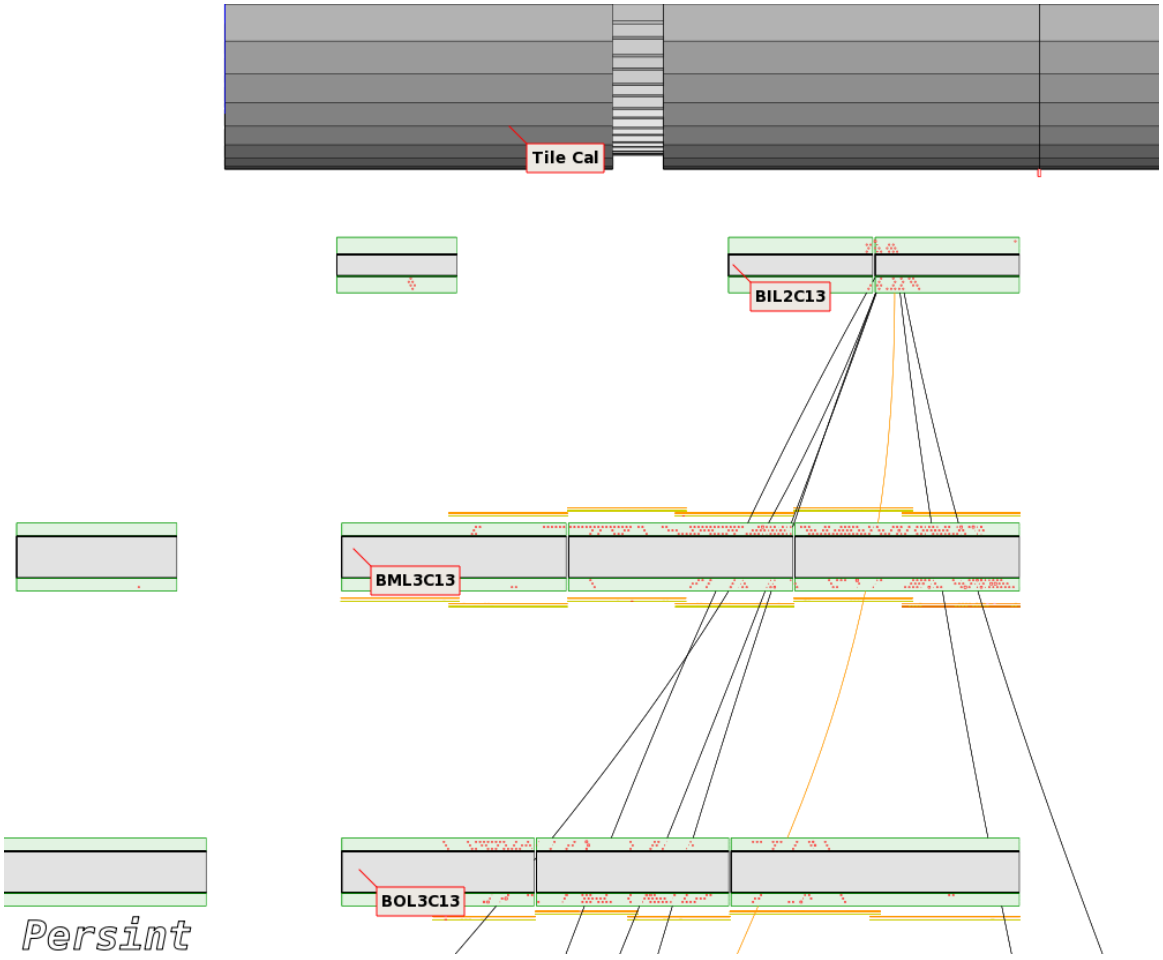

Figure 6.1: Event display showing the Monte Carlo truth tracks from a π_v decay in the MS barrel and the simulated MDT hits.

hits in the MDTs, which is consistent with the expected behavior of a minimum ionizing particle in the muon spectrometer[58], suggesting that a charged pion leaves a clean track in the spectrometer with few spurious hits to confuse pattern recognition.

Next, π^0 's in the same p_T range produced in the muon spectrometer are considered. Figure 6.3 shows the total number of MDT hits resulting from the two photons from the π^0 . The π^0 's that pass through the large sectors (black histogram) produce an average of $\sim$45 MDT hits, while those π^0 's that pass through the magnet coil (red histogram) produce an average of $\sim$150 MDT hits.

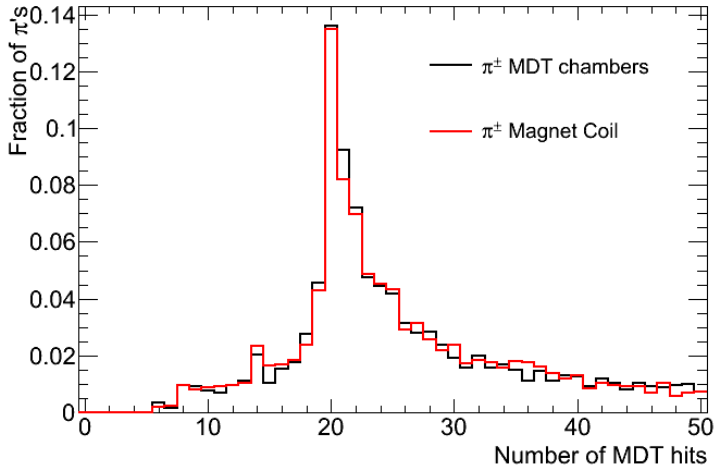

Figure 6.2: MDT hit multiplicity from single charged pions simulation in the MS barrel. In black, pions that pass through the 3 muon stations. In red, pions that pass through the 3 muon stations plus the magnet coil.

From this it is possible to measure the average number of interaction lengths, $<X_0>$, in the muon spectrometer, by measuring the fraction of π^0 's that do not result in an EM shower. Using this method, the interaction lengths are measured to be $<X_0>\sim 0.6$ in the large sectors and $<X_0>\sim 1.6$ in the small sectors, which is in good agreement with the amount of material known to be in the muon spectrometer[31]. The large number of hits due to the γ's showering in the spectrometer has the potential to cause problems with the standard muon reconstruction algorithms, as shown in section 6.2.

6.2 Hidden Valley Decays in the Muon Spectrometer

The p_T distribution of the charged particles from the π_v decay is shown in Figure 4.7. As can be seen, the distribution is sharply peaked at low momentum. These low momentum particles mean that any decay occurring before the last sampling layer of the hadronic calorimeter will not produce a significant number of tracks in the muon spectrometer. Thus, detectable decay vertices must be located in the region between the end of the tile calorimeter and before the middle station of muon

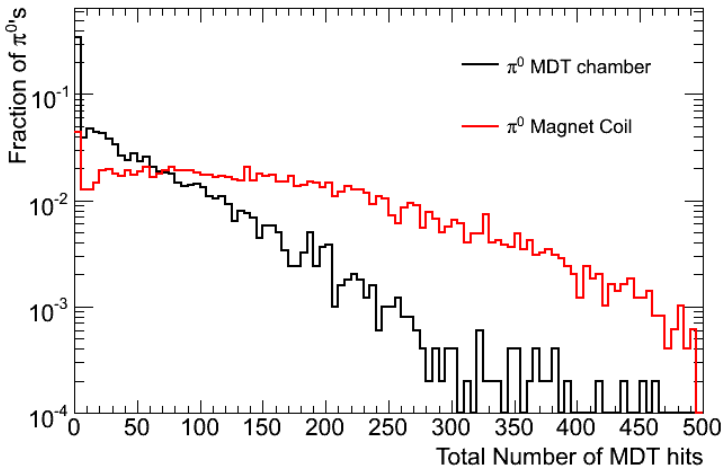

Figure 6.3: MDT hit multiplicity from single π^0 simulation in the MS barrel. In black, π^0 's that pass through the 3 muon stations in the large sectors. In red, π^0 's that pass through the 3 muon stations in the small sector plus the magnet coil.

chambers[1]. This configuration implies that the charged hadrons from the π_v decay will traverse at least two of the MDT stations (middle and outer) while events in which the π_v decays at the end of the hadronic calorimeter, the charged hadrons will traverse all three stations.

As a consequence of the $\sim$5 π^0 's produced in our signal events, large EM showers are expected to accompany the $\sim$10 charged tracks from π_v decays. The effects of these EM showers can be seen in Figure 6.4, which shows the total number of MDT hits per event (Left) and the total number of RPC hits per event (Right) seen in the signal samples. As these plots show, the muon spectrometer is very busy during one of these events with an average of $\sim$800 hits in both the MDT and RPC systems. Figure 6.5 shows the fraction of MDT hits contained in a cone, centered about the π_v line of flight, as a function of the cone size, ΔR. It can be seen that the MDT hits are concentrated in a narrow region of the spectrometer, with $\sim$70% of the hits contained in a cone of size ΔR=0.6. In this region, along the π_v line of flight, the average chamber occupancy is $\sim$30% (Figure 6.6).

[1]The vertex routine requires tracks in at least two MDT stations, therefore decays beyond the middle station will not have a reconstructable vertex.

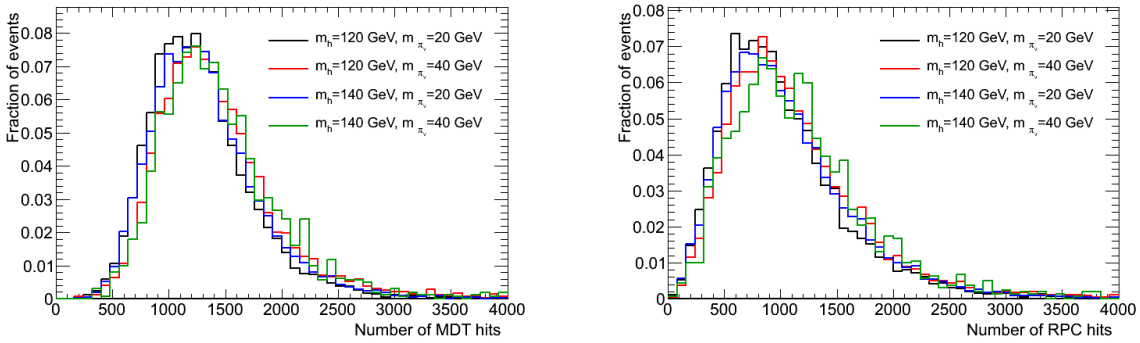

Figure 6.4: Left: Total number of MDT hits per event and Right: Total number of RPC hits per event in signal events where the π_v decays in the barrel region ($|\eta| \leq 0.8$)

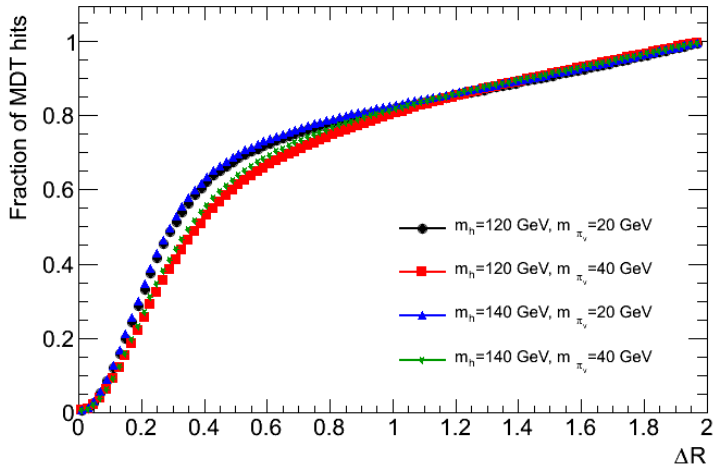

Figure 6.5: Fraction of MDT hits contained in a cone of size ΔR around the π_v line of flight, as a function of ΔR.

A typical muon or $\pi^{\pm}$ gives a track with 20-25 MDT hits, while the average number of hits per charged particle in our displaced decay events is $\sim$100. This implies that on average, an event contains $\sim$75% "noise" hits resulting from the EM shower. These extra hits in the spectrometer cause problems with the standard muon segment finding routines, which are optimized to find muons in a relatively clean, quiet environment. Figure 6.7 shows the number of segments found by the standard reconstruction algorithms, Moore[60] (Left) and MuonBoy[58, 61] (Right), per event and Figure 6.8

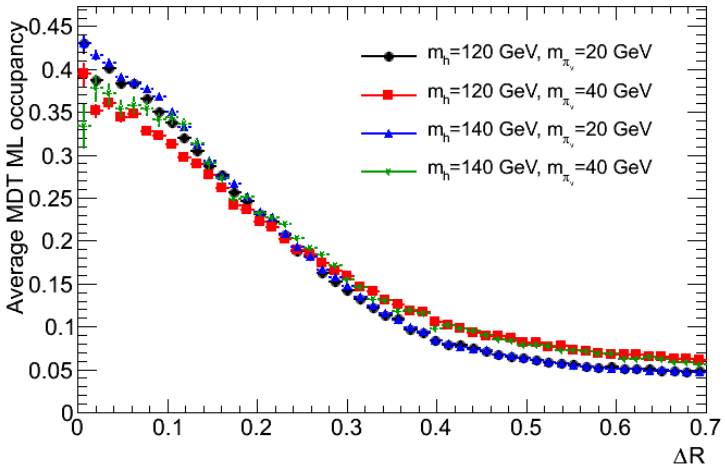

Figure 6.6: Fraction of MDT hits per multilayer (ML) as a function of ΔR between the center of the MDT chamber and the RoI cluster (η,ϕ) in events with a π_v decaying in the barrel muon spectrometer.

shows the χ^2 probability for those segments. The χ^2 probability of the Moore segments is peaked at 1 because errors on the MDT drift radii are artificially increased to increase the efficiency of the algorithm for clean, low p_T tracks. These increased errors lead to a large number of noise hits being reconstructed as segments, as can be seen by the number of reconsturcted segments (Figure 6.7). The χ^2 probability distribution for MuonBoy is sharply peaked at zero which shows that the pattern recognition being used is confused by the large MDT multiplicity. Because the segment finding is not able to identify the segments that belong to a charged track, and the large number of combinatorics, it is not possible to use the standard muon reconstruction algorithms which combine segments from multiple chambers into a single track. Therefore a new approach to the pattern recognition and track momentum reconstruction has been developed.

6.3 Track Finding and Momentum Reconstruction

6.3.1 Track Finding Technique

This new, specialized tracking algorithm starts by reconstructing single multilayer segments that contain 3 or more MDT hits using a private version of the Moore segment finding algorithm[62].

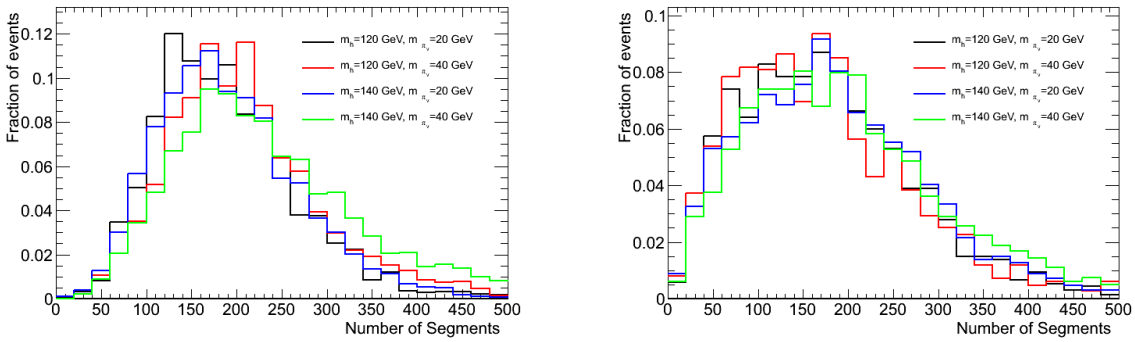

Figure 6.7: The number of segments reconstructed by Moore (Left) and MuonBoy (Right) in events with a π_v decaying in the muon spectrometer.

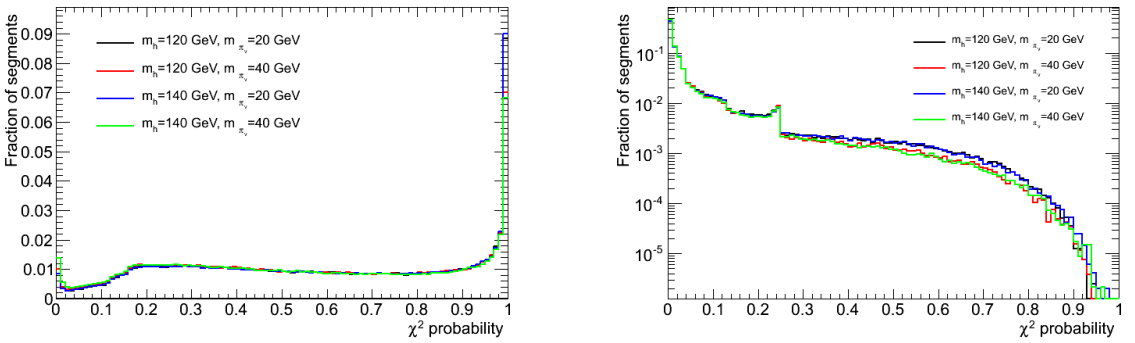

Figure 6.8: χ^2 probability for the reconstructed segments by Moore (Left) and MuonBoy (Right).

All segments that point to the second multilayer and have a χ^2 probability greater than 5% are kept. Figure 6.9 shows the number of single multilayer segments that are reconstructed per event. As expected, due to the large number of hits, an average of 500 single multilayer segments per event are found. This number of segments should be compared to the number of charged particles per signal event[2], approximately 10. It is clear from these distributions that the reconstructed segments contain a large number fakes.

It should be noted that the separation of the two multilayers inside a single chamber provides a

[2]A charged particle will give two single multilayer segments inside an MDT chamber

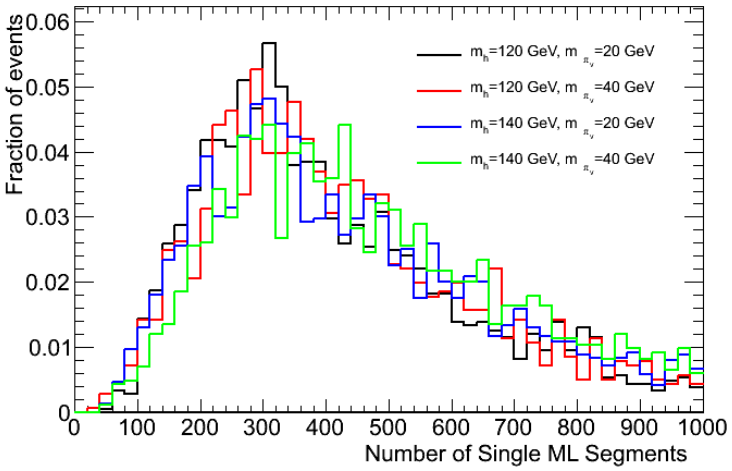

Figure 6.9: Total number of reconstructed single multilayer segments per π_v decay per event

powerful tool for track pattern recognition. This separation provides enough of a lever arm to allow, in the barrel[3], a momentum measurement with an acceptable resolution up to a track momentum of approximately 10 GeV. Therefore, it is crucial to find and correctly pair the segments belonging to the same *tracklet* within the two multilayers of a single chamber.

In order to select the segments that belong to tracklets, segments from multilayer 1 are matched with those from multilayer 2. In this match, two parameters, Δb and $\Delta\alpha$ (see Figure 6.10) are used. The first parameter, Δb , is defined to the be the distance of closest approach between the pair of segments at the middle plane of the MDT chamber [4]. The second parameter, $\Delta\alpha$, measures the bend angle inside the chamber. Thus, by knowing the average magnetic field inside of an MDT chamber, $\Delta\alpha$ can be used to measure the tracklet momentum.

To understand the behavior of the matching parameters, two samples[5] of single pions have been

[3]This technique works throughout the barrel spectrometer, with the exception of the BIS and BOS chambers, which are outside of the magnetic field region.

[4]$\Delta b \sim 0$ selects segments that are tangent to the same circle

[5]Both samples have been simulated using the single particle generator in GEANT4 and have been simulated with a uniform distribution in (η,ϕ).

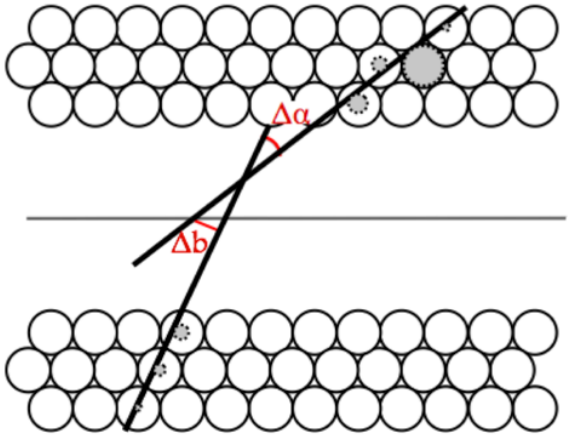

Figure 6.10: Definition of Δb and $\Delta\alpha$ between a pair of segments from the same tracklet in the two MDT multilayers

produced. The first sample consists of high energy pions (1 TeV), which produce straight tracklets inside the muon chambers, and the second sample is low energy pions ($1 < p_{\mathrm{T}} < 10$ GeV). From the high energy sample, the intrinsic angular resolution of the single multilayer MDT segments is measured. Figure 6.11 (Left) shows that the $\Delta\alpha$ matching parameter has a width of $\sim$4.3 mrad. This angular resolution leads to an uncertainty in the segment extrapolation to the middle plane of $\sim$0.75 mm. From this, Δb is expected to have a resolution of $\sim$1 mm, in good agreement with the distribution of Δb shown in Figure 6.11 (Right).

Figure 6.12 shows that Δb is only weakly dependent upon the angle of incidence with respect to the MDT chamber, while the comparison of Figures 6.11 and 6.13 (Right) shows that Δb is independent of tracklet momentum, as the distributions have the same width.

Figure 6.14 shows the bi-dimensional plot of $\Delta\alpha$ versus Δb in the BML chambers for the sample of low momentum pions ($1 < |p_{\mathrm{T}}| < 3$ GeV) in the barrel region ($|\eta| < 0.8$). The $\Delta\alpha$ projection (Figure 6.13, Left) shows a broad, double peaked distribution due to the spread in momentum and to the presence of both π^+ and π^- in the sample. The Δb projection (Figure 6.13, Right) shows the narrow peak with a width of $\sim$1 mm, in agreement with both the 1 TeV sample and the prediction

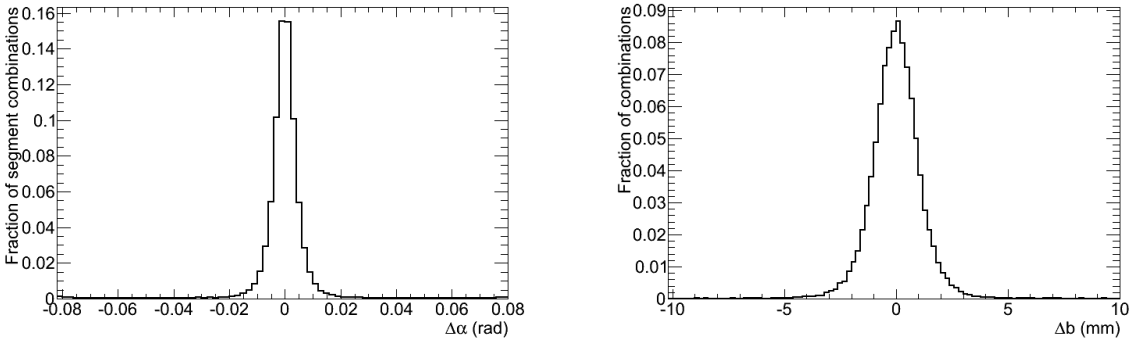

Figure 6.11: Left $\Delta\alpha$ and Right Δb, measured in the middle MDT station, for 1 TeV $\pi^{\pm}$ simulated sample. The $\Delta\alpha$ distribution has a width of 4.33 mrad, and the Δb distribution has a width of 1.01 mm.

from the angular resolution. From these distributions, the matching segment pairs, with $p_{\mathrm{T}} > 1$ GeV, can be seen to have $\Delta b \lesssim 3$ mm and $|\Delta\alpha| \lesssim 70$ mrad.

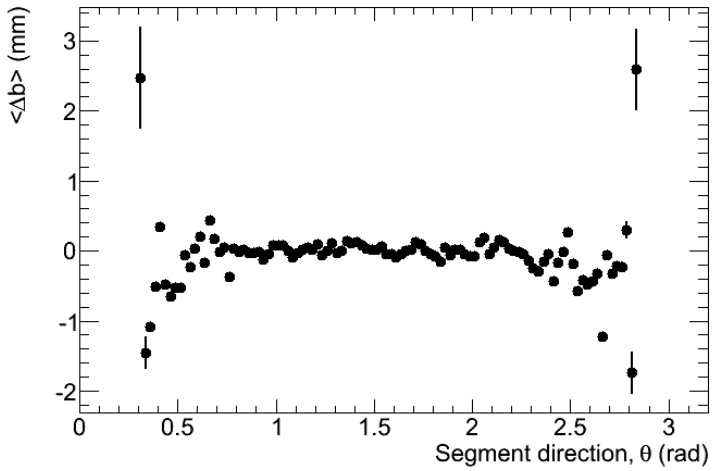

Figure 6.12: Δb as a function of the polar angle between the tracklet and the MDT chamber, measured using the $1 < p_{\mathrm{T}} < 3$ GeV $\pi^{\pm}$ sample.

These results have also been compared with the standard Moore results on the same sample. For the comparison, the standard Moore algorithm segments are required to contain at least 6 MDT

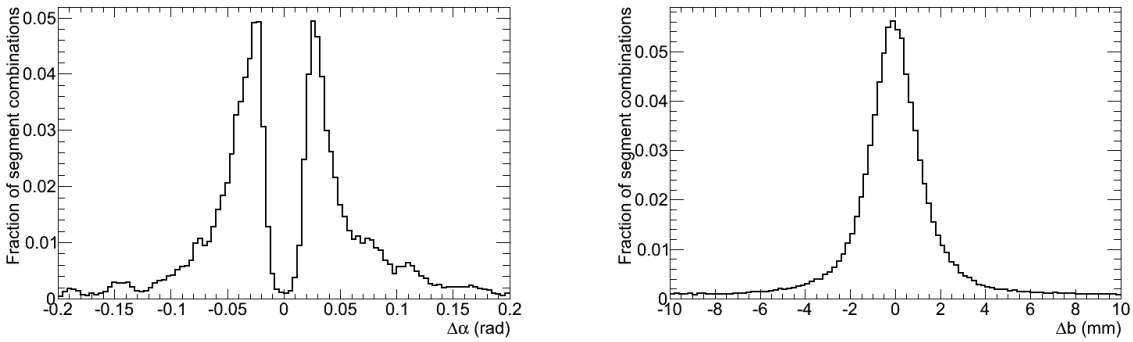

Figure 6.13: $\Delta\alpha$ projection (Left) and Δb projection (Right) for a simulated sample of $\pi^{\pm}$ with $1 < p_{\mathrm{T}} < 3$ GeV and $|\eta| \leq 0.8$. The Δb distribution has a width of 1.05 mm. The flat tails in the Δb distribution are due to multiple solutions to the segment finder, giving segments which are randomly oriented with respect to the true tracklet direction.

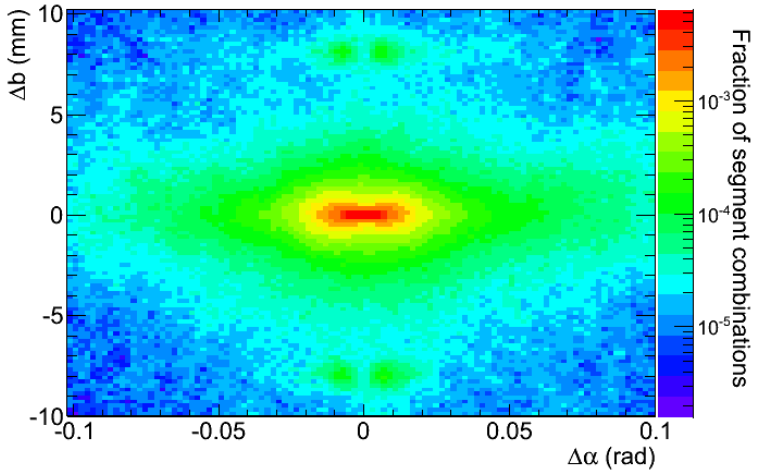

Figure 6.14: Δb vs $\Delta\alpha$ from a $\pi^{\pm}$ simulated sample with $1 < p_{\mathrm{T}} < 3$ GeV and $|\eta| \leq 0.8$, measured inside of the BML chamber

hits and be reconstructed with a χ^2 probability greater than 5%. The new algorithm has higher efficiency at low p_T (see Fig. 6.15), and plateaus at ~95% efficiency (with respect to the standard Moore single chamber segment finding); the reduced efficiency is mainly near the ends of the MDT chambers, where the single multilayer segment crosses between chambers. In the endcap and in the BIS and BOS chambers in the barrel, where the MDT chambers are outside of the magnetic field

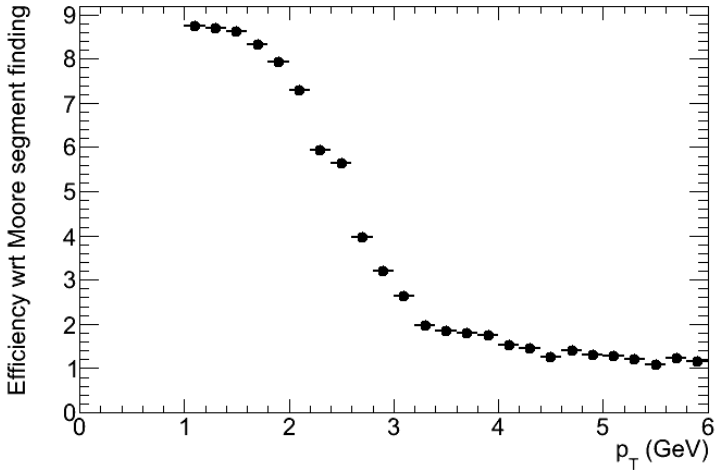

Figure 6.15: Fraction of segments found with respect to the standard Moore segment finding algorithm. For both algorithms, the segments are required to be made from at least 6 MDT hits and have a χ^2 probability greater than 5%.

region, the segment pairs are required to have $\Delta b \leq 3$ mm and $|\Delta\alpha| \leq 12$ mrad. The segment pairs are then refit using the Moore segment finding algorithm. This produces a straight line segment, containing at least 6 MDT hits, which has an improved angular resolution with respect to the two single multilayer segments.

6.3.2 Momentum and Charge Measurements

For segments found in the barrel region of the muon spectrometer[6], the measurement of $\Delta\alpha$ can be used to calculate the tracklet momentum. Because the segments do not have an associated ϕ coordinate, an average magnetic field per chamber must be used. To do this, the sample of low momentum pions has been used to find the correlation between $\Delta\alpha$ and 1/p for each muon station. Figure 6.16 (Left) shows the bi-dimensional plot of $\Delta\alpha$ versus 1/p for pions traversing the BML chambers, and 6.16 (Right) shows the peaks for each value of pion momentum. From the fit of this distribution, a relation of the form $\Delta\alpha$ = k/p is derived for each of the muon stations.

[6]excluding those found in the BIS and BOS chambers, where there is insufficient magnetic field to produce a measurable deflection inside the chamber.

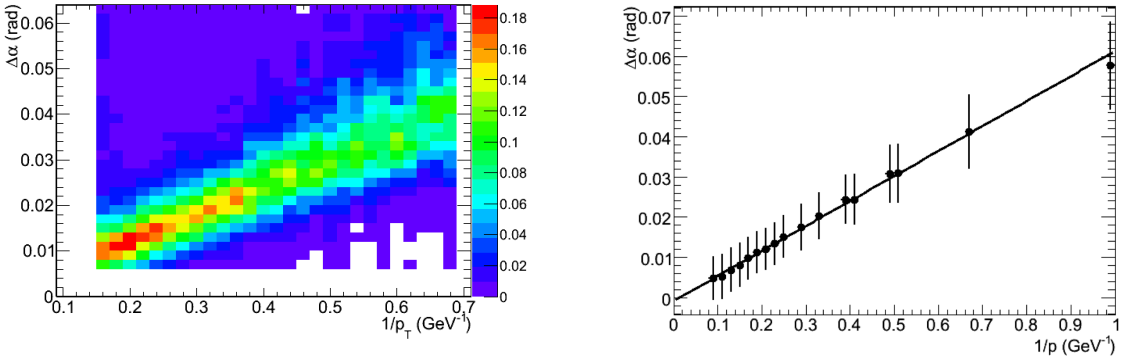

Figure 6.16: Left: bi-dimensional plot of $\Delta\alpha$ vs 1/p from a $\pi^{\pm}$ simulated sample with $1 < p_{\mathrm{T}} < 10$ GeV and $|\eta| < 0.8$; Right: the profile histogram of $\Delta\alpha$ vs 1/p. The error bars represents the width of the $\Delta\alpha$ distribution for each bin

To verify these results and to determine the error in the measurement of 1/p, a toy Monte Carlo which simulates single pions in a constant magnetic field has been created. This simulation measures the tangent to the pion trajectory at two points, separated by the same distance as the MDT multilayers, and smears the tangent direction by 4.3 mrad (the angular resolution measured for single multilayer MDT segments). The value of the magnetic field is taken to be the average field present inside the BML chambers[31]. Figure 6.17 (Left) shows the distribution of $\Delta\alpha$ for single pions, with p_T = 1.5 GeV, in the BML chambers, for both the pion tracklets reconstructed using the algorithm described above (black) and the toy MC (red), while Figure 6.17 (right) shows the distribution for single pions with p_T = 5.5 GeV. In all cases, the toy MC and the full reconstruction agree for the peak position and the width of the distributions. The low momentum (1.5 GeV) pions show a larger tail than the toy MC predicts, which is due to energy loss and scattering inside the muon chamber, neither of which are included in the toy MC.

The agreement between the toy MC and the tracklet reconstruction confirms that the uncertainty in the momentum measurement is dominated by the angular uncertainty in the single multilayer MDT segments. Using the relation $\Delta\alpha$ = k/p and the known uncertainty in $\Delta\alpha$ ($\delta\Delta\alpha \sim 4.3$ mrad), the uncertainty in the momentum measurement can be shown to be δp $\approx$ 0.06*p in the BML cham-

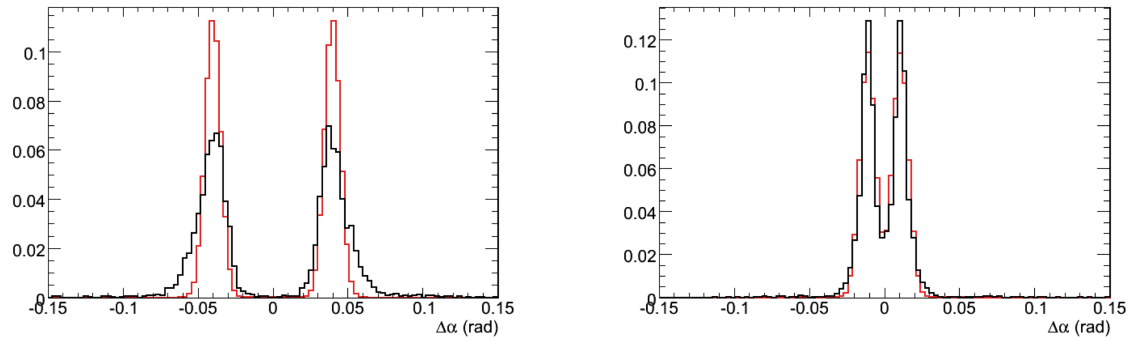

Figure 6.17: $\Delta\alpha$ from Toy Monte Carlo (red) compared with the full simulation results for a simulated sample of single pions of p_T = 1.5 GeV (Left) and p_T = 5.5 GeV (Right).

bers and δp $\approx$ 0.08*p in the BMS chambers.

From Figure 6.17, it is clear that the charge of low momentum tracklets can be measured. For tracklets with momentum less than 5 GeV, the charge of the pion can be identified with an efficiency of greater than 90% throughout the spectrometer, as can be seen in Figure 6.18. For tracklets above 5 GeV, the charge identification efficiency decreases due to the uncertainty in $\Delta\alpha$ becoming comparable to the value of $\Delta\alpha$. For pions with momentum of 7.5 GeV (corresponding to a $<|\ \Delta\alpha\ |>$ = 8 mrad), the charge identification efficiency drops to 70%.

6.3.3 Application of Tracking Algorithm in Signal Events

Having obtained the tracking parameters from single pions, the tracking algorithm can be applied to the Monte Carlo signal events with a π_v decaying in the muon spectrometer. Figure 6.19 shows the bi-dimensional distribution of $\Delta\alpha$ versus Δb for tracklets in the barrel region ($|\ \eta\ | < 1$). The segment combinations corresponding to real tracklets can be seen in the central region, while the diffuse background is from incorrect pairings of segments. This reconstruction method finds an average of 9 single chamber tracklets[7] per event (in all chambers), as can be seen in Figure 6.20 (Left),

[7]For a charged particle originating before the Inner muon station, 3 single chamber tracklets are expected to be associated with the particle, giving a total of $\sim$30 single chamber tracklets in events with a π_v decaying in the spectrometer

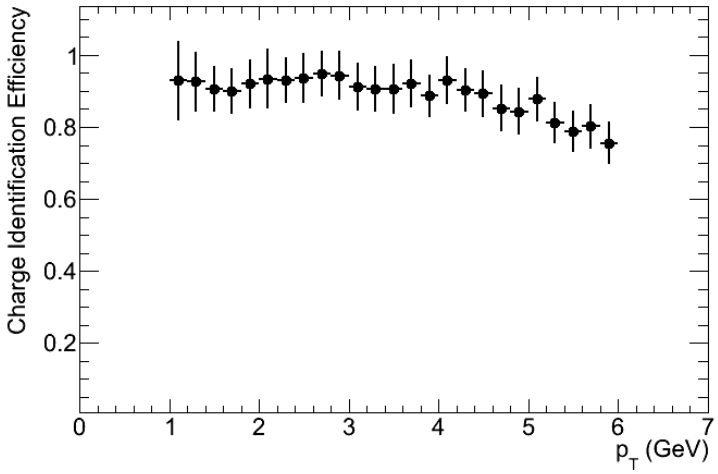

Figure 6.18: Charge identification efficiency for single pions in the BML chambers vs momentum.

and 6 single chamber tracklets with a momentum measurement for events with the π_v decaying in the barrel region (right). Figure 6.21 shows the distribution of Δb for all segment combinations that satisfy the criterion $\mid \Delta\alpha \mid > 70$ mrad. The fraction of fake tracklets reconstructed can be estimated by using the side bands ($\mid \Delta$b$\mid > 5$ mm) to measure the combinatorial backgrounds. The side bands are fit to a straight line which is extrapolated to the signal region, $\Delta b \leq 3$ mm. Taking the ratio of the number of events under the background fit to the total number of events in the signal region gives a fake rate of $\sim$20%. Figure 6.22 shows the number of RPC-phi hits (Left) and RPC-eta hits (Right) per chamber for events where the π_v decays in the barrel region ($\mid \eta \mid < 1$). Due to the large number of RPC measurements, the RPC-phi measurements cannot be associated with the MDT tracklets. This implies that the single chamber tracklets reconstructed using this method will not have an associated phi coordinate or direction. Therefore, in the vertex search, it is assumed that the tracklets are located in the middle in of the MDT chamber and are traveling radially outward.

An example event that demonstrates the functionality of this tracking algorithm is shown in Figure 6.23. In the figure the orange tracks are single chamber reconstructed tracklets extrapolated through the spectrometer volume, and the blue cylinder is the outer surface of the Hadronic Calorimeter. The reconstructed vertex is shown as the red circle (see section 6.4).

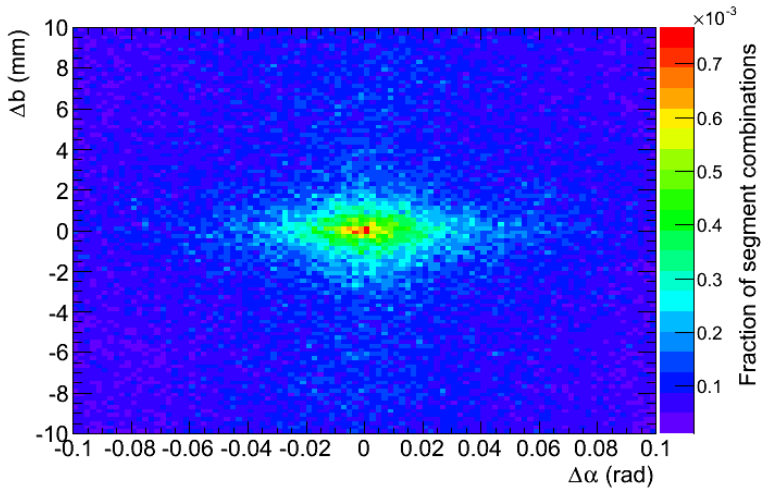

Figure 6.19: $\Delta\alpha$ vs Δb from signal events for segments in the barrel region ($|\eta| < 1$)

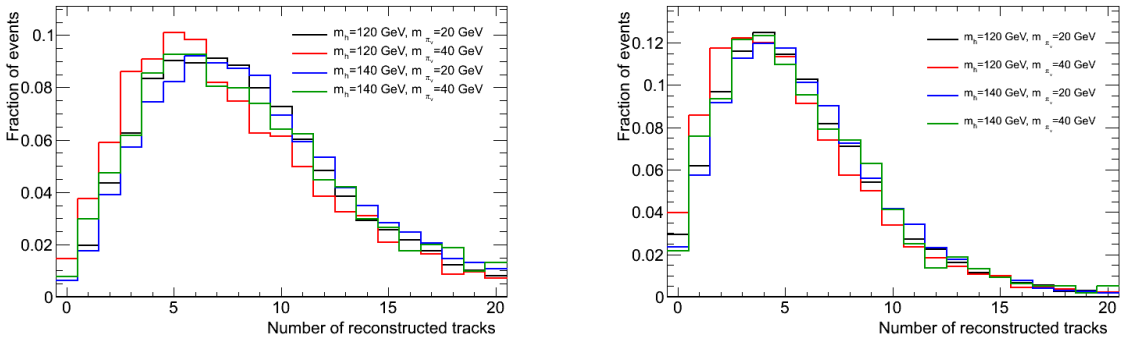

Figure 6.20: Left: Total number of reconstructed single chamber tracklets per event. Right: Number of reconstructed tracklets with a momentum measurement for events with a π_v decaying in the barrel spectrometer.

6.4 Vertex Finding

Due to the differences in the configuration of the magnetic field within the ATLAS muon spectrometer, different vertex algorithms are needed in the barrel region ($|\eta| < 1$) and the endcap region

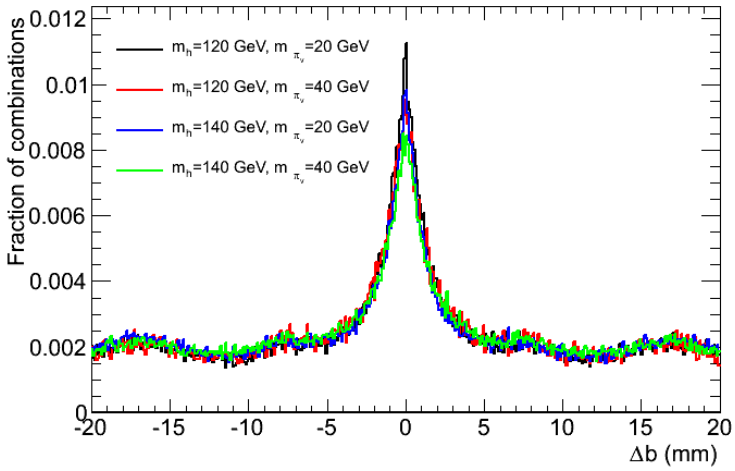

Figure 6.21: Δb from signal events for segments in the barrel region ($\mid \eta \mid < 1$) that satisfy the criteria $\mid \Delta\alpha \mid < 70$ mrad.

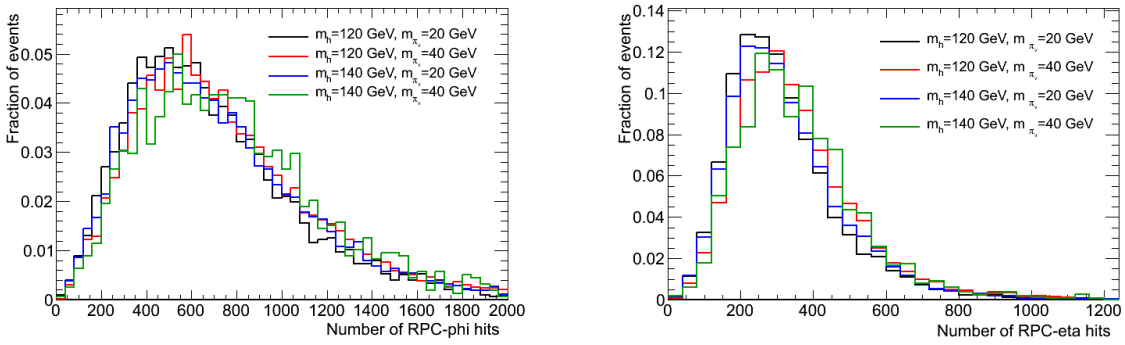

Figure 6.22: Left: Total number of RPC-phi hits for events with a π_v decay in the barrel and Right: The number of RPC-eta hits for same events

($1 < \mid \eta \mid < 2.5$). The driving reason for the use of different algorithms, is the barrel spectrometer is inside the toroidal magnetic field, while the endcap muon chambers are all outside the field region. This implies that all tracklets reconstructed in the endcap are straight and will have no associated momentum measurements, while in the barrel, the tracklets are reconstructed as curved tracklets and will have a measurement of the momentum.

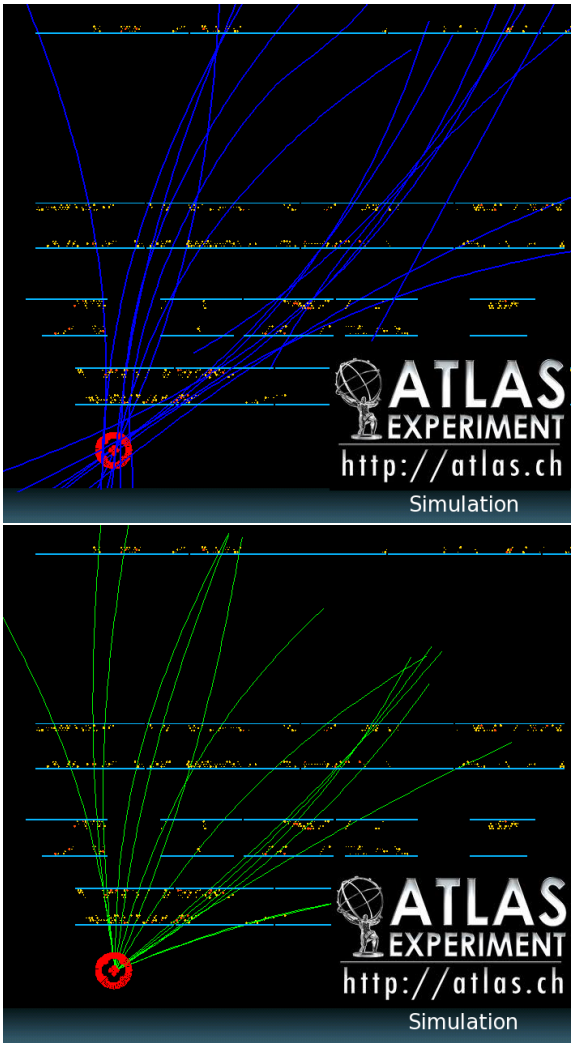

Figure 6.23: Event displaying showing the MC truth (top) and reconstructed (bottom) tracklets and vertex position for a π_v decaying just beyond the hadronic calorimeter. The reconstructed vertex position is shown by the red circle.

6.4.1 Vertex Finding in the Barrel Muon Spectrometer

Finding vertices in the Muon Barrel Spectrometer presents many unique challenges. Because the reconstructed single chamber tracklets do not have any measurement of the ϕ coordinate, the vertex reconstruction must be done in only two dimensions, (R,z). Therefore, all the tracklets used to fit the vertex are rotated into a single ϕ plane. This means that both the magnetic field and distance

between the tracklet measurements and the production vertex are incorrect. This will have the effect of spreading the vertex from a single point where all the tracklets meet, to region where tracklets approach a common point but do not necessarily cross.

In light of these constraints a new vertex finding routine that is able to identify vertices in the spectrometer has been developed. The algorithm starts by finding the set of tracklets to be used in the vertex routine. This is done by using a simple cone algorithm to find the cone of $\Delta R = 0.6$ which contains the maximum number of tracklets. Then the line of flight of the π_v is reconstructed by drawing a line between the IP and the centroid of all single chamber tracklets in our cluster. Figure 6.24 shows that this method is able to reconstruct the π_v line of flight in θ to within 12 mrads. The ϕ of the vertex is computed in two steps, first the average ϕ coordinate of the single chamber tracklets is computed[8]. Then, a cone of $\Delta R = 0.6$ is constructed using these measurements of θ and ϕ as the central axis. The average position of all RPC phi measurements within the cone is computed and taken to be the π_v line of flight in ϕ. Figure 6.25 shows this method is able to reconstruct the ϕ position of the vertex with a resolution of 50 mrads.

The tracklets are then extrapolated to a series of radial planes, which are equally spaced along the line of flight from R = 3.5 m to R = 7 m. The planes are spaced such that the distance, along the line of flight, between two adjacent planes is 250 mm. This results in 15 planes at $\eta = 0$ and increases to 22 planes at $|\eta| = 1$. Increasing the number of planes in this manner insures that the vertex routine treats the entire η range equally, by extrapolating each tracklet a constant distance along the line of flight. The tracklets are then rotated and shifted in position by an angle of 200 mrads, and extrapolated to each of the planes. The difference in the z-position of the shifted and nominal tracklet is measured at each plane, and is used as the uncertainty associated with the extrapolation. This uncertainty is then added, in quadrature, to the uncertainty arising from the error in the measured momentum of the single chamber tracklet. Figure 6.26 shows the uncertainty in the z-position for all tracklets, as a function of the extrapolation distance. The uncertainty ranges from $\sim$10 mm at 0 m of extrapolated distance, to $\sim$150 mm at 5 m of extrapolated distance.

---

[8]Each single chamber tracklet is fixed to be at the center of the MDT chamber where it was found

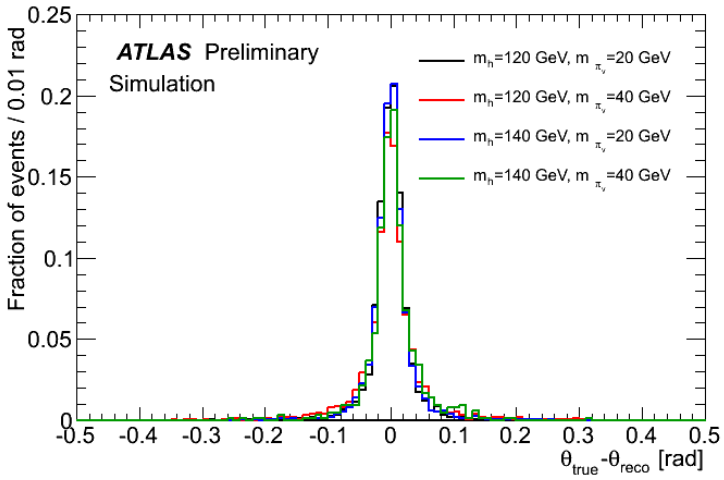

Figure 6.24: Angular difference between the π_v true line of flight in θ and the reconstructed line of flight in θ.

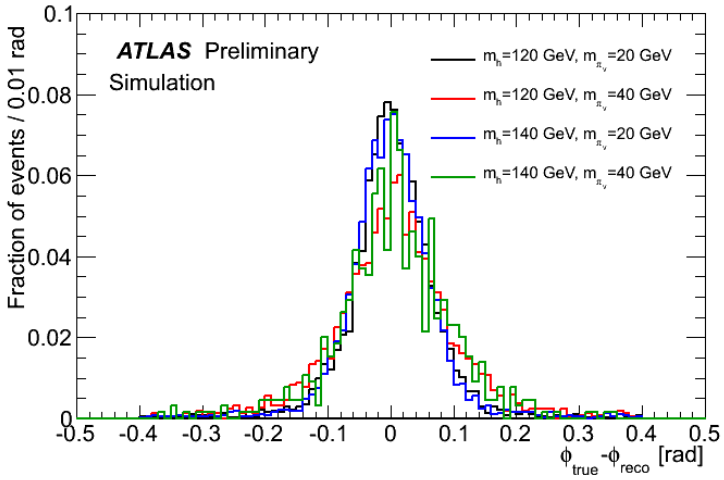

Figure 6.25: Angular difference between the π_v true line of flight in ϕ and the reconstructed line of flight in ϕ, for two different methods, average position of the single chamber tracklets (black) and average ϕ of the RPC/TGC hits (red).

At each plane, the average z-position of the tracklets is computed by weighting the tracklet posi-

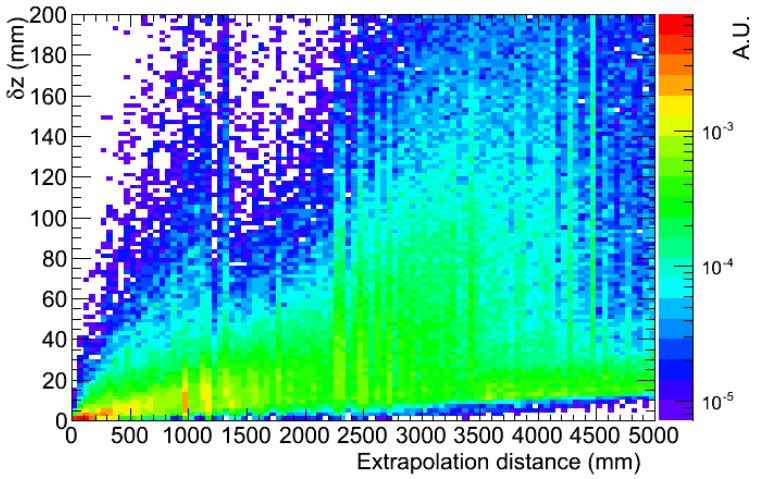

Figure 6.26: Uncertainty in the z-position of tracklets as a function of the extrapolation distance

tion by the significance of the tracklet[9]. Then the χ^2 is computed for each tracklet, assuming that it originates from the vertex point (average z-position). If the χ^2 probability for the vertex point is less than 5%, the worst tracklet is dropped and the vertex point is recomputed. This is done iteratively, until there is either an acceptable vertex, with χ^2 probability greater than 5%, or there are less than 3 tracklets left to compute the vertex point.

The radial position of the vertex is taken from the plane which had the largest number of tracklets used to create the vertex point. In case there are 2 (or more) planes with the same number of tracklets, the plane with the minimum χ^2 is selected as the vertex position. Figure 6.27 shows the number of tracklets used to reconstruct the vertices (Right) and the χ^2 probability for reconstructed vertex (Left). The position of the reconstructed vertex relative to the MC true decay point is shown in Figure 6.28. Using this method, the z and R positions of the π_v decay are reconstructed with a resolution of 200 mm in z and 320 mm in R, as can be seen in Figure 6.29.

Figures 6.30 and 6.31 (Black points) shows the position of the reconstructed vertices in the ATLAS coordinate system for each of the signal samples. The band structure visible in Figure 6.31

[9]The significance of the tracklet is defined as $1/\sigma^2$

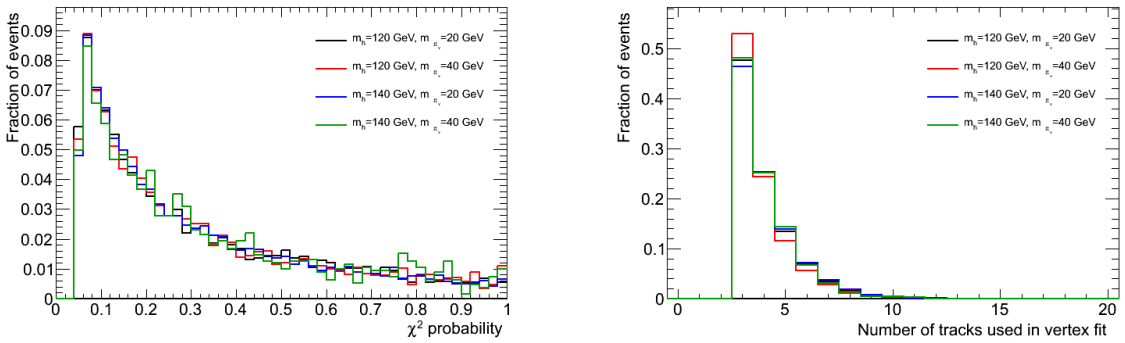

Figure 6.27: Left:χ^2 probability for each vertex region. Right:Number of tracklets associated to each vertex region.

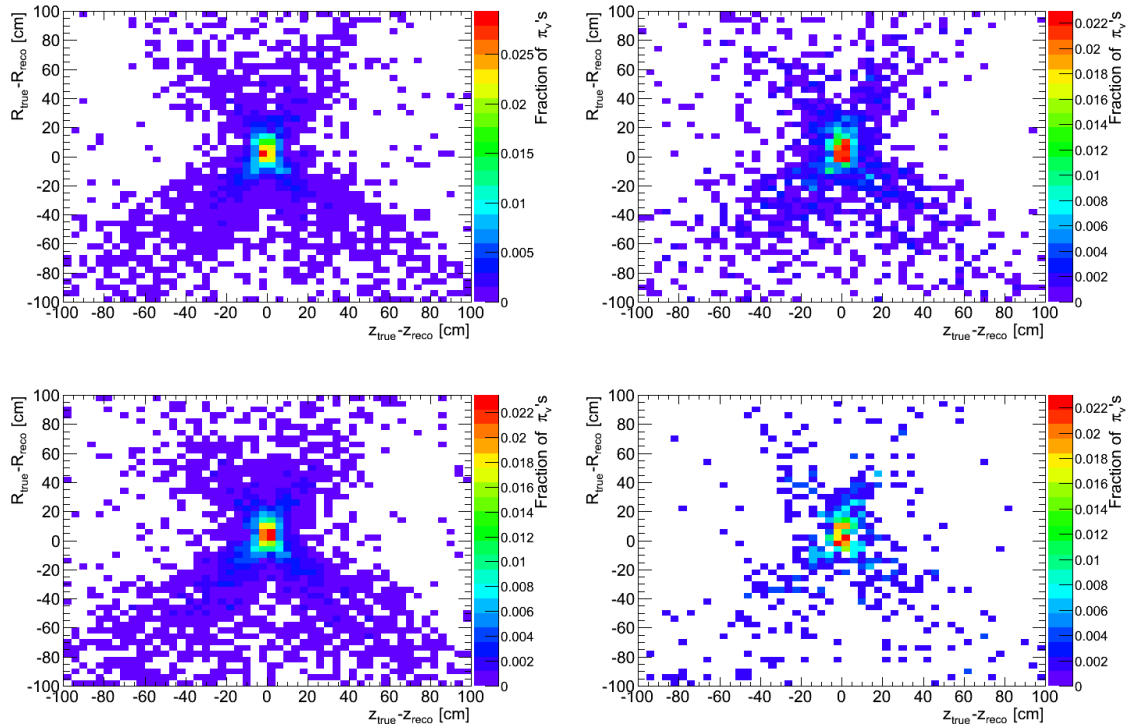

Figure 6.28: Position of the reconstructed vertex relative to the π_v true decay position. Top Left: m_h = 120 GeV, m_{π_v} = 20 GeV, Top Right: m_h = 120 GeV, m_{π_v} = 40 GeV, Bottom Left: m_h = 140 GeV, m_{π_v} = 20 GeV, Bottom Right:m_h = 140 GeV, m_{π_v} = 40 GeV

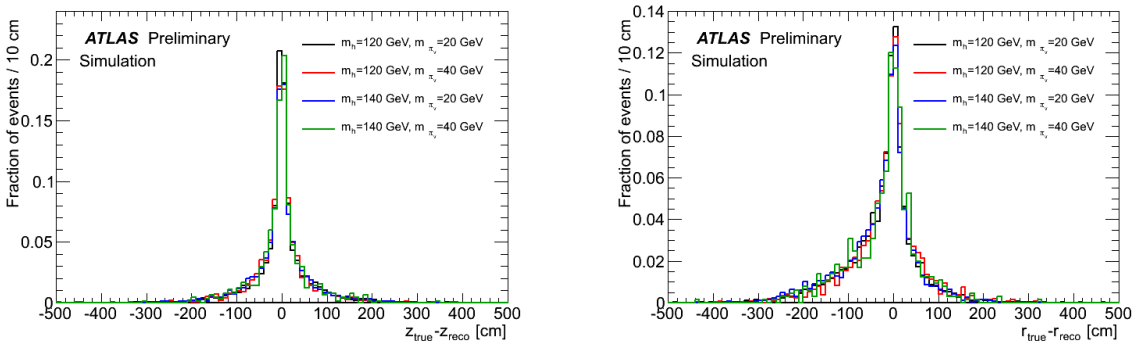

Figure 6.29: Left:Difference between the z-coordinate of the reconstructed vertex and π_v true decay position, for decays in the barrel muon spectrometer. Right:Difference between the R-coordinate of the reconstructed vertex and π_v true decay position.

is due to the vertex reconstruction algorithm. The algorithm has a lower efficiency near the magnet coils because π_v's decaying in this region produce a larger number of noise hits, due to the extra material present in the magnet coil (see Figure 6.3).

6.4.2 *Vertex Finding in the Endcap Muon Spectrometer*

Decays in the endcap muon spectrometer must occur in the range $7 < |z| < 14$ m to be detectable. Due to the low momentum particles (Figure 4.7), particles from π_v decays that occur before 7 m will not have enough energy to reach the middle station[10], while decays occurring after the middle station (14 m) will not be seen. This implies the detectable decays will occur inside of the endcap toroid, and measurements of the tracklets will be made after they have been bent by the magnet. This leads to a systematic shift in the position of the vertex and a degraded resolution with respect to the vertices found in the barrel region.

Single chamber tracklets from π_v decays in the endcap region ($1 < |\eta| < 2.5$) have no momentum or charge measurements, thus a different approach to vertex finding is required. In this region of the spectrometer, a simple linear extrapolation and minimization routine to find the vertex region is employed. Again, the routine starts by grouping tracklets into a set that is clustered in (η,ϕ). The

[10]The endcap calorimeter extends to 7 m.

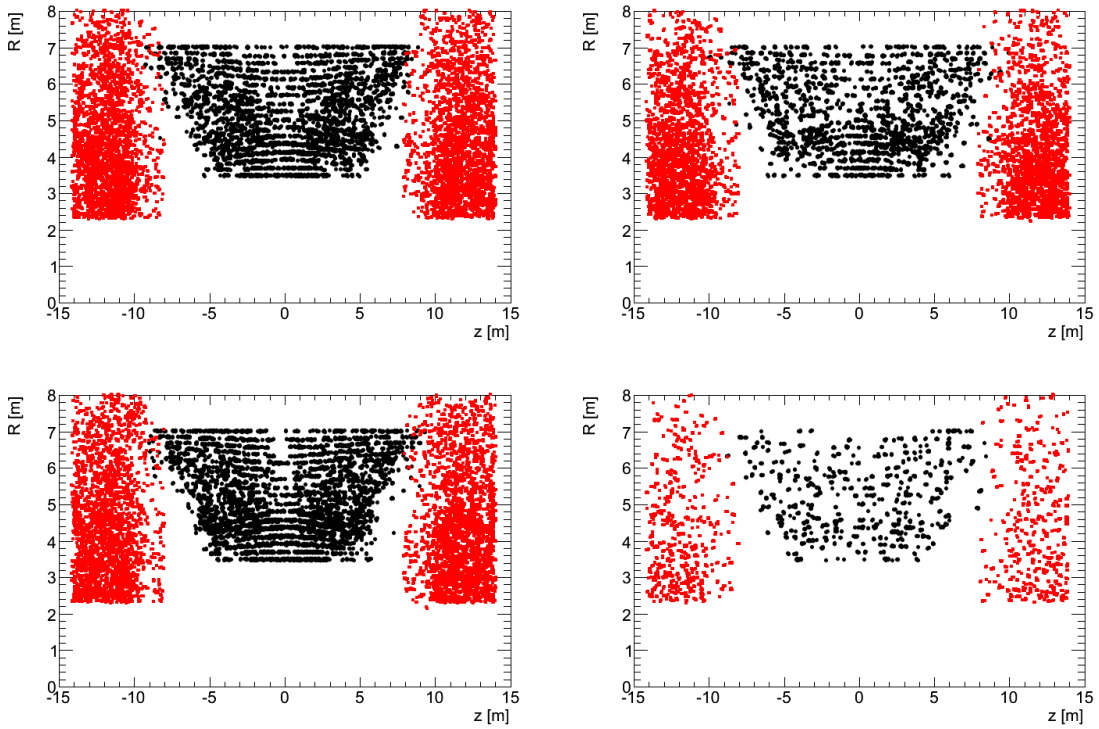

Figure 6.30: Position of the found vertices in the ATLAS global coordinate system, (R,z), in π_v Monte Carlo events. Black points show the vertices reconstructed in the barrel and the Red squares show those reconstructed in the endcap. Top Left: m_h = 120 GeV, m_{π_v} = 20 GeV, Top Right: m_h = 120 GeV, m_{π_v} = 40 GeV, Bottom Left: m_h = 140 GeV, m_{π_v} = 20 GeV, Bottom Right:m_h = 140 GeV, m_{π_v} = 40 GeV

line of flight in θ and ϕ are calculated as in the barrel, except the TGC-phi measurements are used instead of the RPC-phi measurements. The resolution in the line of flight in both θ and ϕ are shown in Figure 6.32 and are comparable to the resolution achieved in the barrel.

The clustered tracklets provided constraining equations of the form b_i = -R tanθ_i + z, which are used in a least squares regression fit of the vertex, using the formulae:

$$R_{vertex} = \frac{(\sum \frac{tan\theta_i}{\sigma_i^2})(\sum \frac{b_i}{\sigma_i^2}) - (\sum \frac{tan\theta_i}{\sigma_i^2})(\sum \frac{b_i tan\theta_i}{\sigma_i^2})}{(\sum \frac{1}{\sigma_i^2})(\sum \frac{tan^2\theta_i}{\sigma_i}) - (\sum \frac{tan\theta_i}{\sigma_i^2})^2} \text{ and } z_{vertex} = \frac{(\sum \frac{tan\theta_i}{\sigma_i^2})(\sum \frac{b_i}{\sigma_i^2}) - (\sum \frac{1}{\sigma_i^2})(\sum \frac{b_i tan\theta_i}{\sigma_i^2})}{(\sum \frac{1}{\sigma_i^2})(\sum \frac{tan^2\theta_i}{\sigma_i}) - (\sum \frac{tan\theta_i}{\sigma_i^2})^2}$$

where θ is the polar angle of the single chamber tracklet, and b is the intercept. The vertex position is then iterated, dropping the tracklet that is farthest from the vertex until the farthest tracklet is

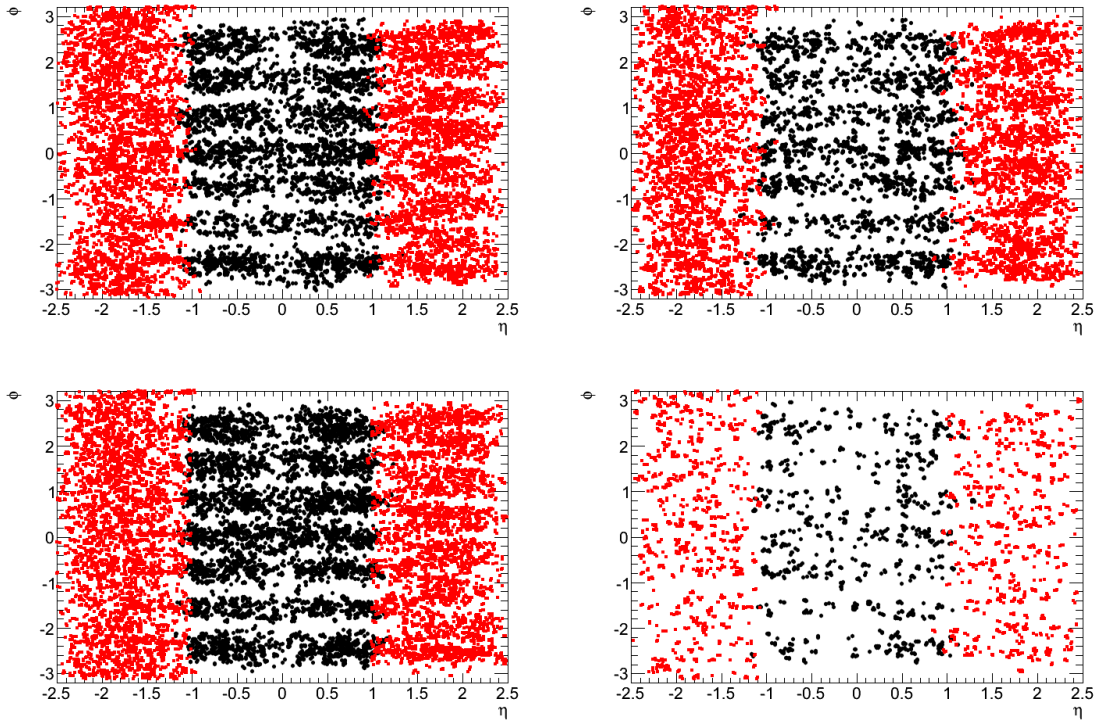

Figure 6.31: Position of the found vertices in the ATLAS global coordinate system, (η,ϕ), in π_v Monte Carlo events. Black points show the vertices reconstructed in the barrel and the Red squares show those reconstructed in the endcap. Top Left: m_h = 120 GeV, m_{π_v} = 20 GeV, Top Right: m_h = 120 GeV, m_{π_v} = 40 GeV, Bottom Left: m_h = 140 GeV, m_{π_v} = 20 GeV, Bottom Right:m_h = 140 GeV, m_{π_v} = 40 GeV

within 30 cm of the vertex. The position is taken to be a good vertex if it has been reconstructed using at least 3 tracklets and is within the endcap muon spectrometer, before the middle station (|z| = 14 m). Figure 6.33 shows the radial position of the reconstructed vertices with respect to the Monte Carlo true decay point. As noted early, because the tracklets are measured outside the magnetic field region and do not have momentum or charge measurements, the position of the vertex is systematically shifted toward larger values of R_{reco}.

Figures 6.30 and 6.31 (Red squares) shows the position of the reconstructed vertices in the ATLAS coordinate system for each of the signal samples.

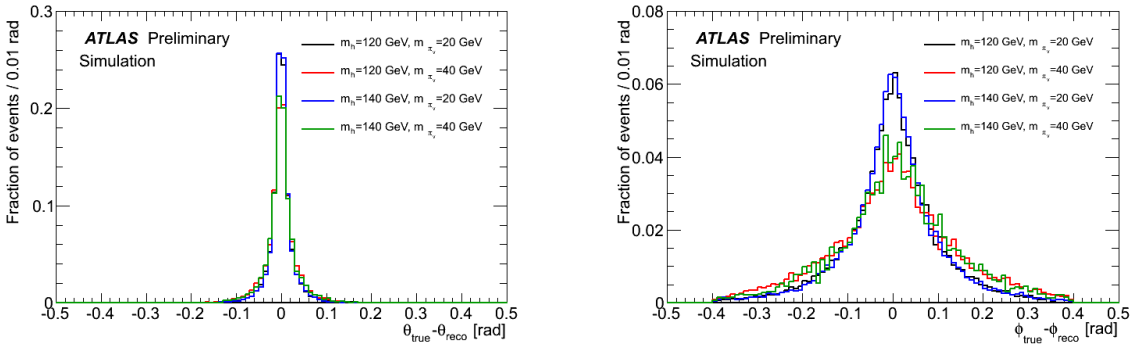

Figure 6.32: Angular difference between the π_v true line of flight and the reconstructed line of flight. Left: θ line of flight, Right: ϕ line of flight.

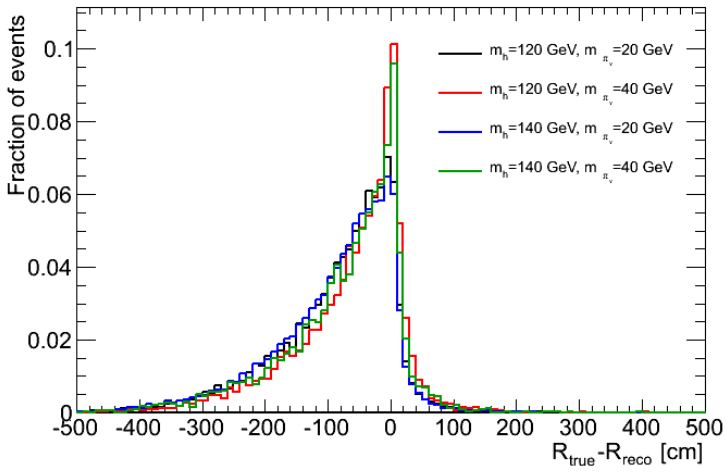

Figure 6.33: Difference between the R-coordinate of the reconstructed vertex and π_v true decay position.

6.5 Good Vertex Criteria

Events with vertices that originate from cosmic or punch-through events can be rejected by making a series of cuts once the vertex has been found. First, the found vertex is required to be consistent with the hypothesis that it was created from the decay of a particle that originated at the IP. To do this, the sum of the p_z for all tracklets used in the vertex fit is required to point toward the IP. Next, the vertices are required to be isolated with respect to high p_T tracklets ($p_T > 5$ GeV) in the inner

detector and isolated from jets ($E_{\mathrm{T}} > 15$ GeV) in the calorimeter. These isolation criteria remove vertices originating from Standard Model processes, all of which originate at the IP. The vertex is required to be in a busy region of the muon spectrometer, which is defined as a region with at least 200 MDT hits. To remove events with a noise burst in the MDTs, which causes coherent noise hits to be present in a large number of MDT chambers, the vertex is required to be in a region of the detector with less than 3000 MDT hits. To further remove noise events, the vertex is required to be in the region of the spectrometer that contains at least 100 RPC hits (or TGC hits if the vertex is in the endcap) since a noise burst in the MDT system should not be coherent with the trigger system. The values of these cuts have been selected to be the window of $\sim$100% acceptance for signal MC events that have a π_v decaying inside of the muon spectrometer, Figure 6.34.

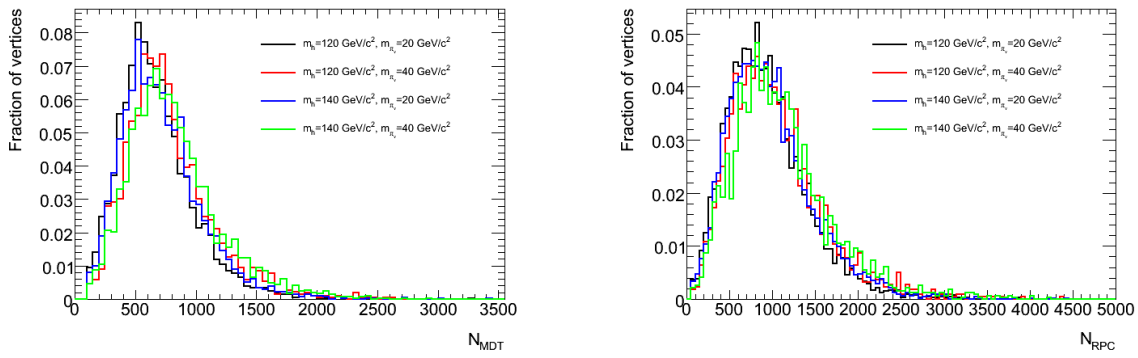

Figure 6.34: Left: Number of MDT hits in a cone of $\Delta R < 0.6$ around the reconstructed vertex. Right: Number of RPC (or TGC) hits in a cone of $\Delta R < 0.6$ around the reconstructed vertex.

In order to be considered a good vertex, the reconstructed muon spectrometer vertex must satisfy the following criteria:

- Vertex Pointing: The sum of the p_z of all tracklets used in the vertex fit is required to point toward the IP.

- N_{MDT}: The number of MDT hits contained in a cone of $\Delta R < 0.6$ around the vertex are required to be in the range $200 < N_{MDT} < 3000$

- N_{RPC}: The number of RPC hits contained in a cone of $\Delta R < 0.6$ around the vertex for π_v's decaying in the barrel spectrometer is required to be $N_{RPC} > 100$

- N_{TGC}: The number of TGC hits contained in a cone of $\Delta R < 0.6$ around the vertex for π_v's decaying in the endcap spectrometer is required to be $N_{TGC} < 100$

- η: The vertex is required to be in in the range $| \eta | < 2.2$, such that the vertex is within the ID tracking coverage

- Jet Isolation: ΔR between the vertex and the nearest jet in the calorimeter with $E_T > 15$ GeV and $\log_{10}(E_{HAD}/E_{EM}) < 0.5$ is required to be ΔR(jet,vertex) ¿> 0.7.

- Track Isolation: ΔR between the vertex and the nearest ID track with $p_T \geq 5$ GeV is required to be ΔR(ID track,vertex) > 0.4

To study the affects of pileup, the pileup in the Monte Carlo samples has been varied by removing the pileup reweighting tool, which effectively increases the amount of pileup in the signal samples. The trigger efficiencies were compared between the nominal pileup (which was reweighted to reflect the pileup seen in data) and the un-reweighted sample to measure the sensitivity of the good vertex criteria to pileup. This procedure yields an uncertainty on the efficiency to reconstruct a good vertex of 2% for each of the Monte Carlo samples. The JES uncertainty is determined by varying the isolation cut by 5%, the JES uncertainty at the jet energies of the cut value (15 GeV). The resulting change in the number of reconstructed good vertices is 4%.

The position of the found vertices in η and ϕ, after applying this good vertex criteria, are shown in Figure 6.35 for those vertices reconstructed from the 1.94 fb^{-1} of 2011 data. The peaks at $\eta \sim$ -0.8 and $\phi \sim$0 are due to beam halo, which is most prominent at $\phi \sim 0$. For comparison, the position of the found vertices from the Monte Carlo signal samples are shown in Figure 6.36. The vertex algorithm has a lower efficiency near the magnet coils, $\phi \sim \pm\frac{(2n+1)\pi}{4}$, because the number of shower MDT hits from photons and hadrons is higher in these regions due to the extra material of the magnet coil. Further, the momentum resolution is worse near the coils, due to the rapidly changing

magnetic field. These effects lead to a lower overall efficiency for vertex reconstruction.

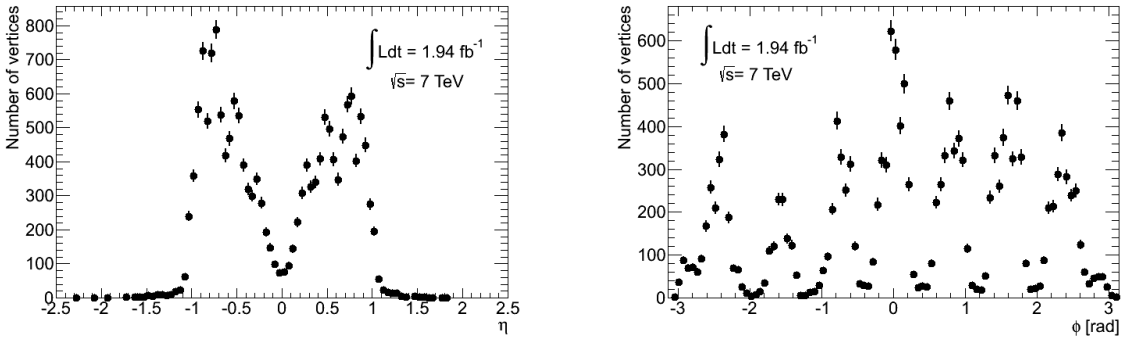

Figure 6.35: Left: The η position of the reconstructed, good vertices found in data. Right: The ϕ position of the reconstructed, good vertices found in data.

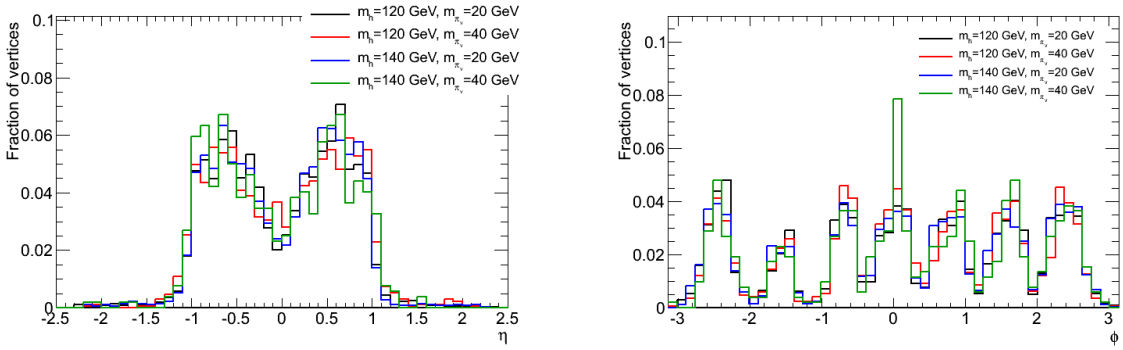

Figure 6.36: Left: The η position of the reconstructed, good vertices found in each of the four Monte Carlo signal samples. Right: The ϕ position of the reconstructed, good vertices found in each of the four Monte Carlo signal samples.

The position of the found vertices, in RZ, is shown in Figure 6.37, for the good vertices reconstructed in the 1.94 fb^{-1} of 2011 Data. The vertices tend to group around $|z| \sim 4$ m and R ~ 4 m, near the crack region between the Barrel and Extended Barrel calorimeters where particles can escape the calorimeter volume without depositing energy in the calorimeter.

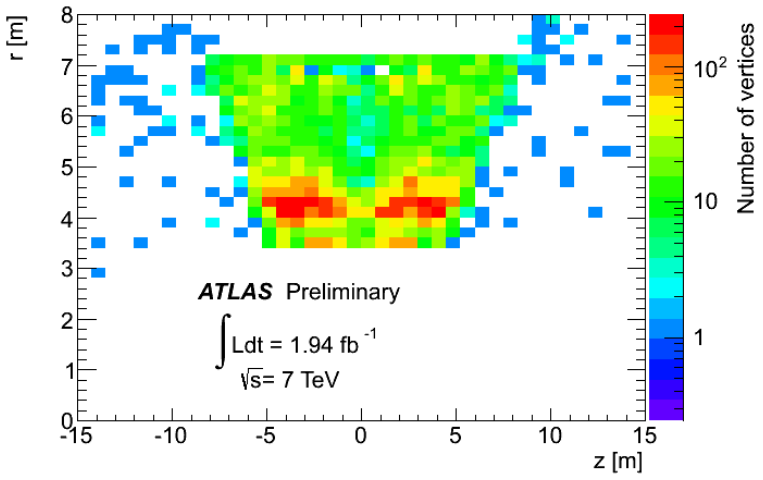

Figure 6.37: The position, in RZ, of the reconstructed vertices from 1.94 fb^{-1} of 2011 Data.

6.6 Data Monte Carlo Scale Factor

To validate the muon spectrometer vertex algorithm, its performance on MC must be verified to data. Therefore, the vertex routine has been run on a sample of events containing a jet that has punched-through the calorimeter. This sample of events is similar to the signal events as it contains both low-energy photons and charged hadrons in the muon spectrometer. The candidate punch-through jets are selected to be in the barrel region ($|\eta| < 1.5$) and contain a minimum of 300 MDT hits in a cone of $\Delta R = 0.6$, centered around the jet axis. To verify that the jet was produced in the collision and is not machine or cosmic related noise, the jet is required to contain at least four tracks with $p_T > 1$ GeV in the inner detector. Additionally, missing energy of at least 20 GeV is required to point in the direction of the jet, indicating that a significant portion of the jet has punched-through the calorimeter.

The total number of MDT hits in a cone of $\Delta R = 0.6$, centered around the jet axis is shown in Figure 6.38. For comparison, the total number of MDT hits in a cone of $\Delta R = 0.6$, centered around the reconstructed vertex, in signal MC events is shown in Figure 6.34 (Left). More important than the total number of hits, is the way in which the MDT hits are distributed. Figure 6.39 shows the

average multilayer occupancy near the punch-through jet in the QCD Monte Carlo, where only multilayers with at least three MDT hit have been counted.

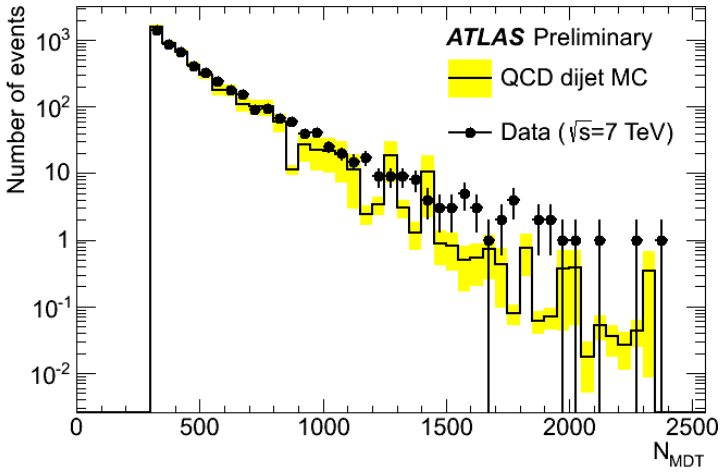

Figure 6.38: The total number of MDT hits contained in a cone of $\Delta R = 0.6$, centered around the jet axis, for punch-through jets in Data and QCD Monte Carlo.

For comparison, a single MC signal curve, from Figure 6.5 (Right), has been overlaid. As can be seen, the average multilayer occupancy around the punch-through jets is similar to that found around the π_v in signal MC events. Therefore, by using the punch-through jets, the tracking and vertex routines are run in environments similar to those produced in the signal events.

The track reconstruction routine is run on both the punch-through jets and the signal MC. Figure 6.40 shows the comparison of the Δb between the punch-through jets, measured in data, and one of the MC signal samples. As expected, due to the similar multilayer occupancies, the distribution of Δb is also very similar between the punch-through jets and the MC signal sample. The fraction of fake tracks reconstructed can be estimated by extrapolating the side bands ($|\Delta b| > 5$ mm) into the signal region ($|\Delta b| < 3$ mm). Taking the ratio of the number of tracks under the background fit to the total number of tracks in the peak yields a fake rate of $\sim$20% for both the MC signal sample and the punch-through jets. Figure 6.41 shows the total number of tracks reconstructed in

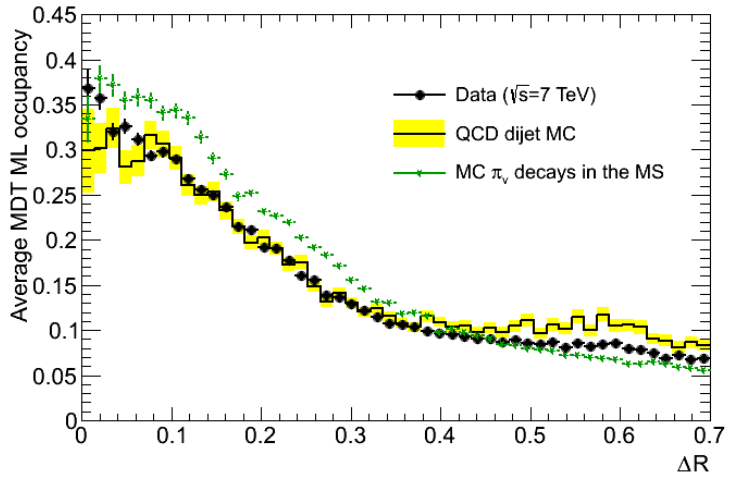

Figure 6.39: Average occupancy of MDT multilayer as a function of ΔR between the center of the MDT chamber and the jet axis for the MC QCD sample and average occupancy of MDT multilayer as a function of ΔR between the center of the MDT chamber and the π_v line of flight.

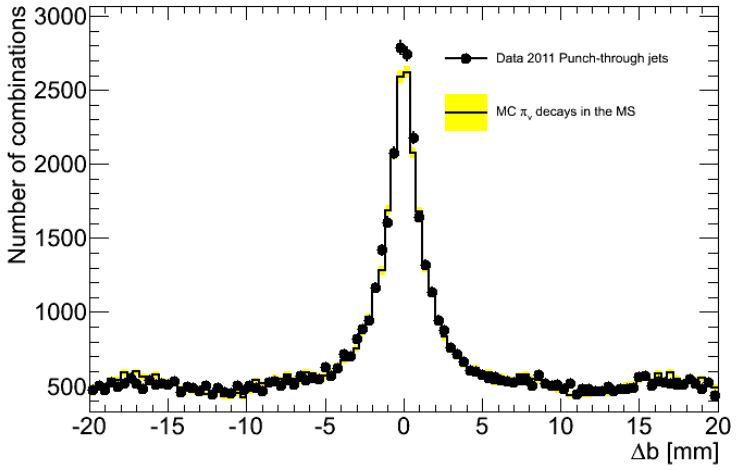

Figure 6.40: Distribution of Δb for all combinations of single multilayer segments found in punch-through jets from data (data points) and MC π_v decays in the muon spectrometer (histogram).

punch-through jets (Left) and signal Monte Carlo (Right). The punch-through jets have a fewer number of reconstructed tracks, with respect to the signal, which will lead to a lower efficiency in reconstructing vertices in the punch-through sample. As can be seen in Figure 6.42, both the tracks

from punch-through jets (Left) and the signal Monte Carlo (Right) have momentum peaked at relatively low values, ∼1 GeV. Figure 6.43 shows the angle, α (see Figure 6.10), of the reconstructed

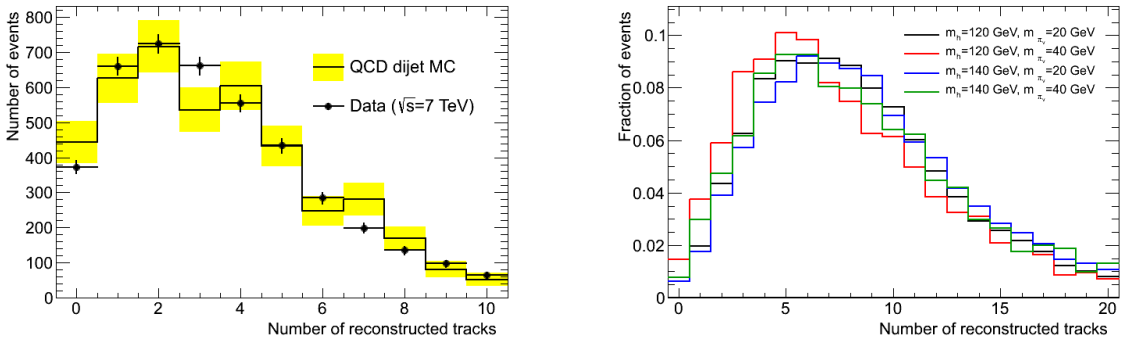

Figure 6.41: The total number of tracks reconstructed by the specialized tracking algorithm. Left: Tracks from punch-through jets. Right: Tracks from signal Monte Carlo with a π_v decay inside the spectrometer.

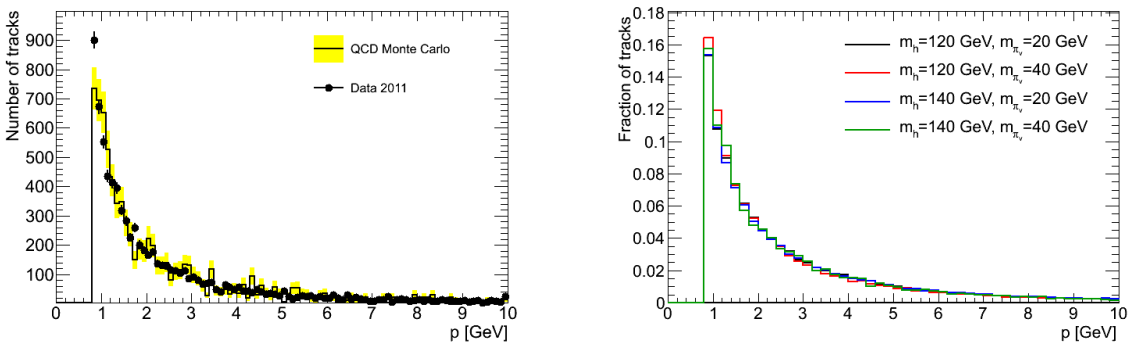

Figure 6.42: The total momentum of the reconstructed tracks. Left: Tracks from punch-through jets. Right: Tracks from signal Monte Carlo with a π_v decay inside the spectrometer.

tracks from punch-through jets (Left) and the signal Monte Carlo samples (Right). The angle of the tracks produced by the punch-through jets reproduces well, the entire range of the angles present in the signal samples. There are no tracks reconstructed with $\alpha \sim 0$ or $\alpha \sim \pi$ due to the tracking method, which requires a single multilayer segment to be reconstructed in both multilayers of the MDT chamber.

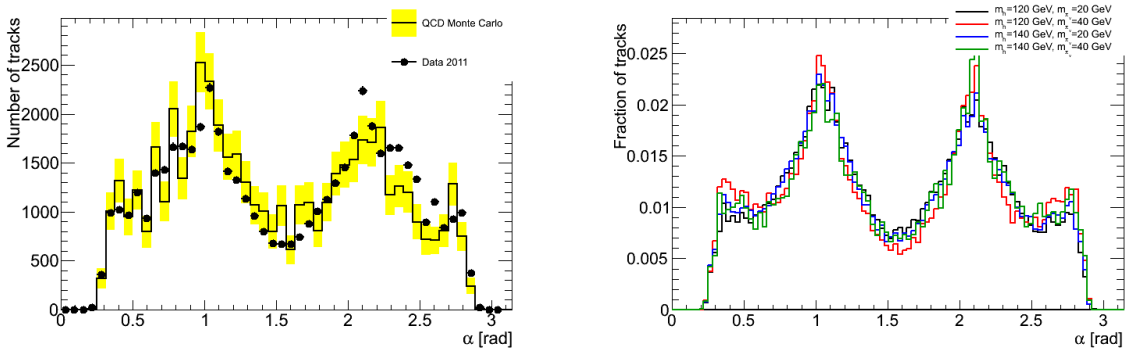

Figure 6.43: The angle, α, the of the reconstructed tracks in the local chamber reference frame (see Figure 6.10). Left: Tracks from punch-through jets. Right: Tracks from π_v decays in the muon spectrometer.

The vertex routine is then run on these events and the results from data and QCD Monte Carlo are compared to ensure that the Monte Carlo is correctly reproducing the environment that is present when both charged hadrons and photons are present in the muon spectrometer. Table 6.1 gives the number of events that have a punch-through (PT) jet and the number of events that have a reconstructed MS vertex as a function of the number of MDT hits contained inside the jet cone. In the Monte Carlo, only the samples J3,J4 and J5 have been used because the J0, J1 and J2 samples did not contribute any events, while the J6 cross section (0.033 nb) makes its contributions below the one percent level.

By weighting the Monte Carlo samples by their respective cross sections, the fraction of jets that satisfy the punch-through criteria and produce a vertex can be calculated. Table 6.2 gives the fraction of punch-through jets that have a good vertex for each of the values of MDT hits for both data and Monte Carlo. Figure 6.44 shows the ratio of data and Monte Carlo for punch-through jets that have a good vertex. As can be seen, the ratio, within uncertainty, is constant for all values of MDT hits in the jet cone. A fit of these data points to a straight line yields 1 ± 0.15. Therefore, the scale factor between data and Monte Carlo is taken to be 1 and the 15% statistical uncertainty is assigned as a systematic uncertainty to the vertex routine. The total systematic uncertainty on

Sample	MC cross section	$300 \leq N_{MDT} < 400$ N. PT jets	$300 \leq N_{MDT} < 400$ N. reco vertices	$400 \leq N_{MDT} < 500$ N. PT jets	$400 \leq N_{MDT} < 500$ N. reco vertices	$500 \leq N_{MDT} < 600$ N. PT jets	$500 \leq N_{MDT} < 600$ N. reco vertices	$N_{MDT} \geq 600$ N. PT jets	$N_{MDT} \geq 600$ N. reco vertices
MC QCD J3	2192.9 nb	135	13	67	5	30	4	49	7
MC QCD J4	87.701 nb	774	91	400	63	204	24	350	80
MC QCD J5	2.3501 nb	3482	433	1837	260	1071	191	2184	534
2011 Data	–	3855	352	2531	267	1734	226	3704	617

Table 6.1: Number of punch-through (PT) jets that have a reconstructed vertex in the muon spectrometer for data and Monte Carlo.

Number of MDT hits	QCD Monte Carlo	2011 Data
$300 \leq N_{MDT} < 400$	10.1 ± 2.2 %	9.1 ± 0.5 %
$400 \leq N_{MDT} < 500$	9.2 ± 2.8 %	10.5 ± 0.7 %
$500 \leq N_{MDT} < 600$	13.1 ± 5.4 %	13.0 ± 0.9 %
$N_{MDT} \geq 600$	16.5 ± 4.5 %	16.7 ± 0.7 %

Table 6.2: Fraction of punch-through jets that have a reconstructed vertex in the muon spectrometer for each of the MDT selections.

the muon spectrometer vertex is the sum (in quadrature) of the uncertainties from the JES on the isolation (4%), the uncertainty in the ISR on isolation (4%), the uncertainty from pile up (2%) and the comparison of MC to data (15%), which yields a total systematic uncertainty of 16%.

Figure 6.45 shows the separation, in ΔR, between the reconstructed vertices and the center of the punch-through jet. As can be seen, the vertex is very well aligned with the jet axis. Of the 1462 reconstructed vertices, zero were reconstructed with $\Delta R > 0.7$ from the jet axis, and only 8 vertices were reconstructed with $\Delta R > 0.5$. Fitting the falling edge of the distribution and integrating the tail ($\Delta R > 0.7$), the probability a vertex from a punch-through jet will be isolated can be calculated to be $\sim(4 \pm 1)\times10^{-5}$, where the uncertainty is taken from varying the region of the histogram which was fit.

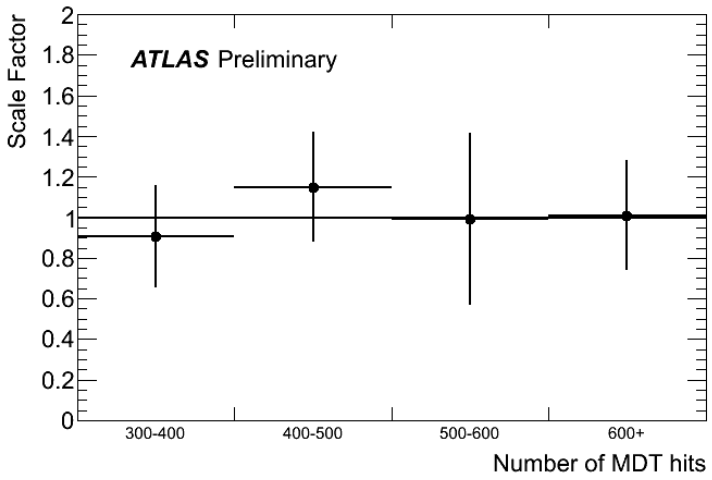

Figure 6.44: The scale factor (the ratio of data to Monte Carlo) for the fraction of punch-through jets that produce a vertex in the muon spectrometer.

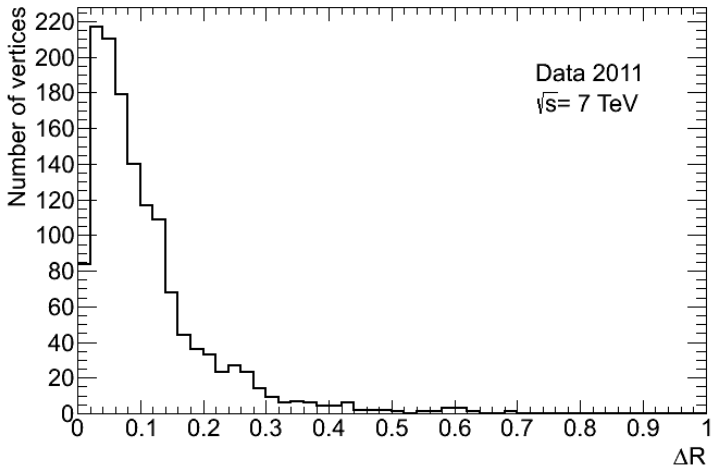

Figure 6.45: ΔR between the axis of the punch-through jet and the position of the reconstructed vertex.

6.7 Vertex Finding Efficiency and Expected Number of Events

The efficiency for vertex reconstruction is defined as the fraction of π_v's that decay in at a distance L from the IP that have a reconstructed vertex which satisfies all the criteria to be considered a good, isolated vertex as described in Section 6.5. The efficiency is divided into two sub cases: those events that pass the Muon RoI Cluster trigger and those events that do not pass the trigger. Figures 6.46 show the efficiency to reconstruct a vertex in the barrel muon spectrometer for events that pass the Muon RoI Cluster trigger (Left), and those that do not pass the trigger (Right). For events that pass the trigger, the vertex Reconstruction routine is ∼50% efficient throughout the sensitive region.

The efficiency for reconstructing a π_v in the endcap region is shown as a function of z in Figure 6.47,

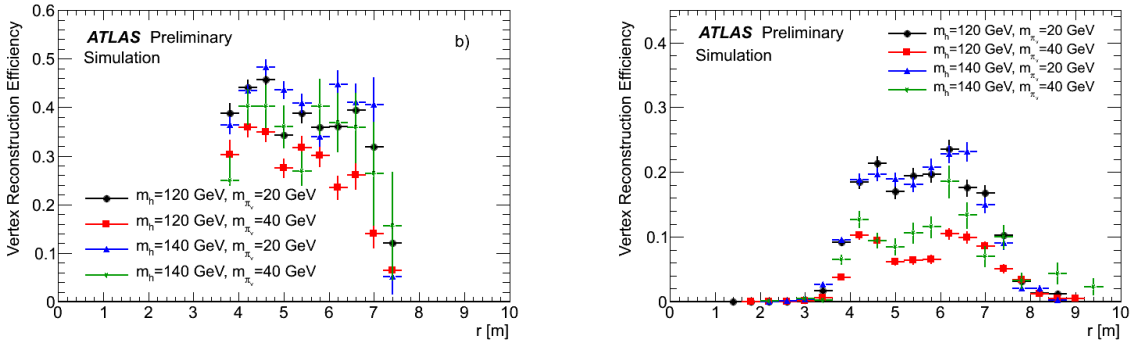

Figure 6.46: Efficiency for reconstructing a vertex for π_v decays in the barrel muon spectrometer for events that pass the RoI Cluster trigger (Left) and events that do not pass the RoI Cluster trigger (Right) as a function of the radial decay position of the π_v.

which shows the efficiency is roughly constant from 7 m to 14 m.

6.7.1 Expected Number of Signal Events

From the trigger efficiency (Figures 5.11, 5.24,and 5.31), and the vertex reconstruction efficiency (Figures 6.46 and 6.47), it is possible to predict the number of events that pass the trigger selection and have a reconstructed vertex in the muon spectrometer as a function of the π_v proper lifetime. In making this prediction, a branching fraction of 100% is assumed for the process $h^0 \rightarrow \pi_v\pi_v$. The expected number of events is found by simulating one million $h^0 \rightarrow \pi_v\pi_v$, at the generator level, for

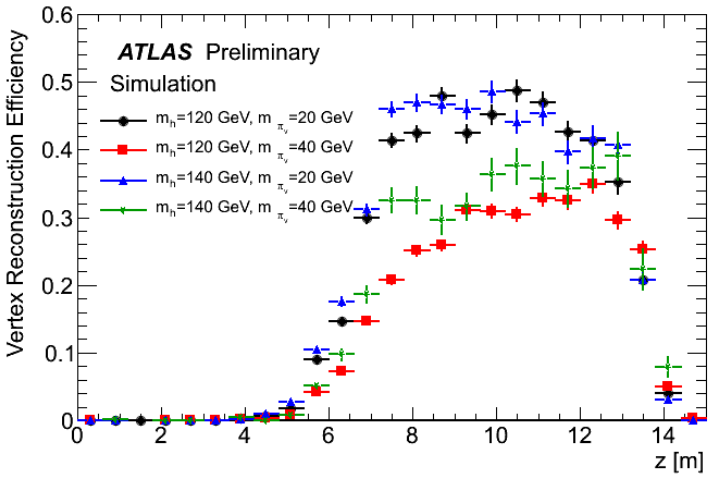

Figure 6.47: Efficiency for reconstructing a vertex for a π_v decaying in the endcap muon spectrometer as a function of the z decay position of the π_v.

a range of lifetimes (from 0 - 35 m, in steps of 50 mm). For each event, the trigger probability is determined based upon the π_v's decay positions and the corresponding trigger efficiencies for those regions. If the event is simulated to pass the trigger, then the probability to reconstruct a vertex in the muon spectrometer is applied to the π_v's. Using this method, the fraction of events that are expected to be on tape and have a reconstructed vertex in the muon spectrometer. Figure 6.48 shows the expected number of events with at least one reconstructed vertex as a function of the π_v proper lifetime for a dataset of 1 fb^{-1} for each of the four Monte Carlo signal samples. The error band is determined by combining in quadrature the uncertainties corresponding to the trigger efficiency and vertex reconstruction efficiency including the systematic uncertainties and the Higgs cross section uncertainty.

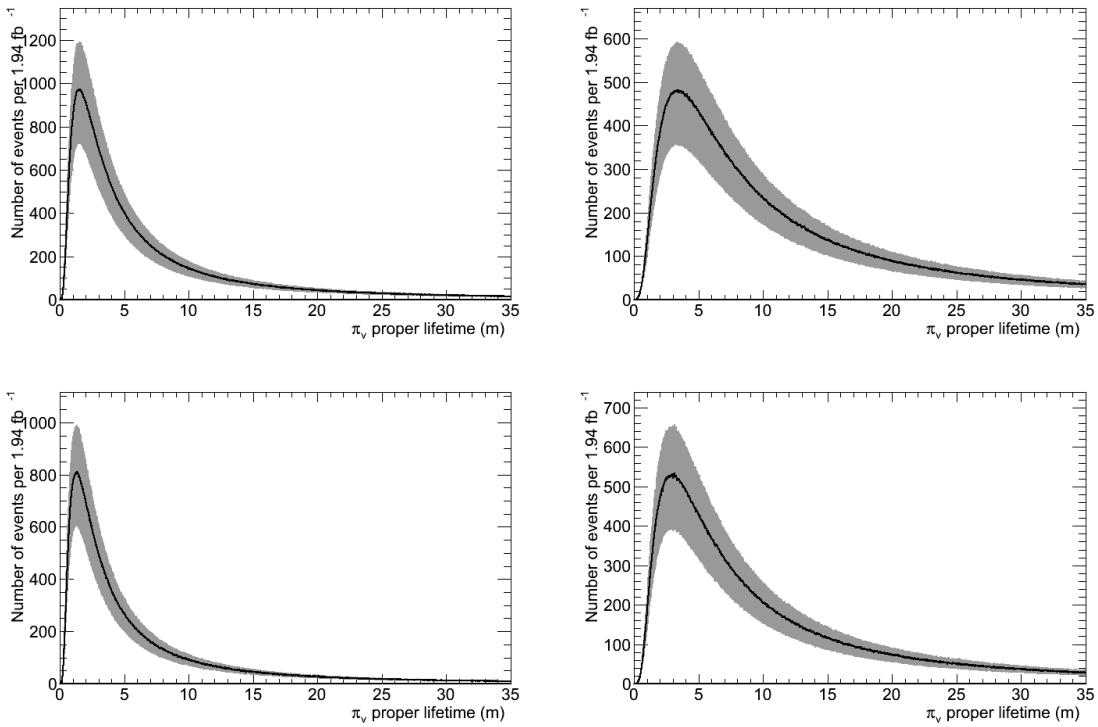

Figure 6.48: The expected number of $h^0 \rightarrow \pi_v \pi_v$ that pass one of the Hidden Valley triggers and have a reconstructed vertex in the muon spectrometer as a function of the π_v proper lifetime for each of the four signal samples, assuming a dataset of 1 fb^{-1} . The Error bands represent the 1 σ uncertainty for the number of events. Top Left: m_h = 120 GeV, m_{π_v} = 20 GeV, Top Right: m_h = 120 GeV, m_{π_v} = 40 GeV, Bottom Left: m_h = 140 GeV, m_{π_v} = 20 GeV, Bottom Right:m_h = 140 GeV, m_{π_v} = 40 GeV

Chapter 7

ANALYSIS

The analyses presented here require that all events pass the Muon RoI Cluster trigger. The events are required to have a primary vertex which consists of three or more tracks, each with at least one pixel and two SCT hits associated and p_{T} >0.5 GeV. The events are further required to have a vertex in the muon spectrometer which satisfies the good vertex criteria from Section 6.5.

7.1 Overlapping Signatures

In order to reduce backgrounds, the second π_v is also required to decay within the volume of the ATLAS detector. The analyses are split depending on the decay position of the second π_v, as the signature of the displaced decay depends on the decay position. The first analysis searches for events in which the second π_v has also decayed inside the volume of the muon spectrometer. The other analysis searches for events where the second π_v decayed in the region between the end of the pixel detector to the end of the hadronic calorimeter. Figure 7.1 shows the fraction of events that have both π_v decays in the muon spectrometer (Left) and the fraction of events with one π_v decay in the spectrometer and the second contained in the fiducial volume[1], as a function of π_v proper lifetime.

The decay position of the second π_v determines signature combination used in the search. In searching for events with two π_v's decays in the spectrometer, the signature is two vertices in the spectrometer. The search for events with a π_v decay in the spectrometer and the second before the end of the hadronic calorimeter, the signature is a vertex in the spectrometer and a jet with no reconstructed tracks in the ID. For both analyses, the objects (MS vertex or jet) are required to be separated by $\Delta \mathrm{R} \geq 2$.

[1]The fiducial volume of the detector is the region bounded by the middle plane of the MS and $|\eta| \leq 2.5$.

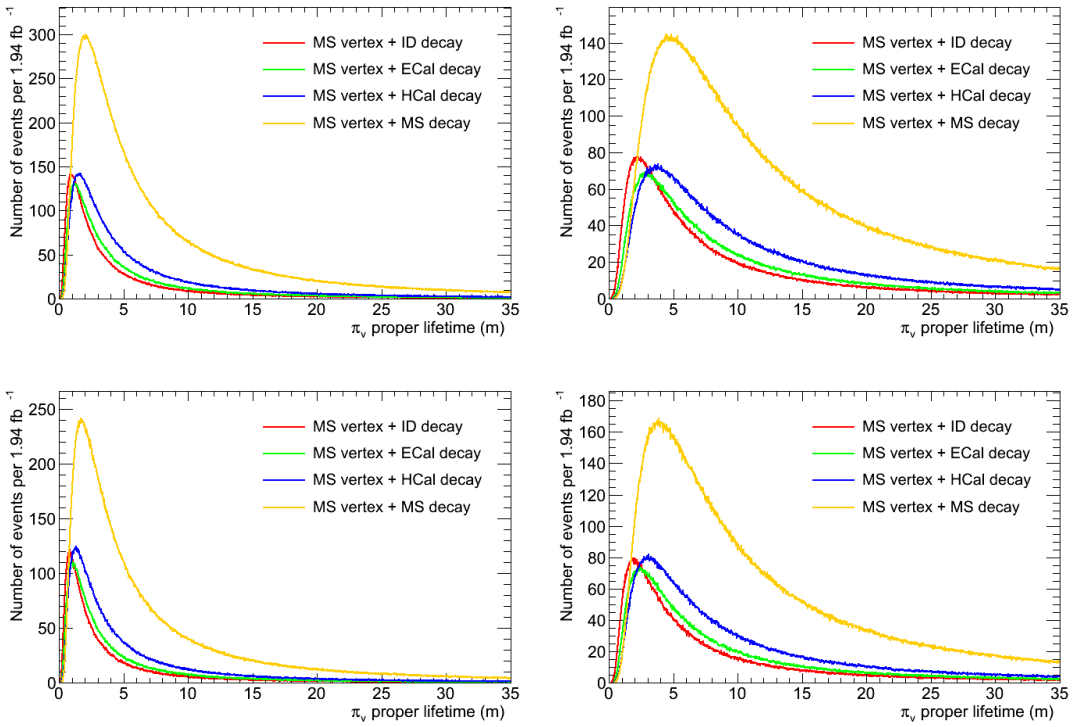

Figure 7.1: Expected number of events with a reconstructed MS vertex and a π_v decay in one of four regions of the detector. Each curve shows the number of events as a function of the π_v's proper lifetime where one π_v is reconstructed as a MS vertex and the second one decays in the inner detector (ID decay), or decays after the tracking system (ECal decay), or decays after the LAr calorimeter (HCal decay) or decays in the muon spectrometer. Top Left: m_h = 120 GeV, m_{π_v} = 20 GeV, Top Right: m_h = 120 GeV, m_{π_v} = 40 GeV, Bottom Left: m_h = 140 GeV, m_{π_v} = 20 GeV, Bottom Right:m_h = 140 GeV, m_{π_v} = 40 GeV

7.2 Two Vertices in the Muon Spectrometer

As can be seen in Figure 7.1, over a wide range of lifetimes, there are a significant number of events with a vertex in the muon spectrometer in which the second π_v has also decayed inside the muon spectrometer. In this event topology, the analysis strategy is to select events with two vertices in the muon spectrometer.

7.2.1 Event Selection

The final event selection requires two good MS vertices, separated by $\Delta R > 2$. See section 6.5 for the definition of a good MS vertex. As stated earlier, the requirement of two good MS vertices significantly reduces backgrounds.

7.2.2 Expected Background

The backgrounds to events with two vertices in the muon spectrometer can be calculated using data driven techniques. To calculate the background, it is necessary to measure the following quantities:

- N(MS vertex, 1 trig): Number of events which have one muon RoI cluster trigger and a vertex in the spectrometer.

- P_{vertex}: Probability to reconstruct a vertex in the spectrometer for events that do not pass the RoI cluster trigger.

- N(MS vertex, 2 trig): Number of events with a vertex in the spectrometer and have two distinct muon RoI clusters

- P_{reco}: Probability to reconstruct a vertex in the spectrometer for events that passed the RoI cluster trigger.

The number of background events with two vertices in the spectrometer can be calculated as

$$N_{Fake}(\text{2 MS vertex}) = \text{N(MS vertex, 1 trig)*}P_{vertex} + \text{N(MS vertex,2 trig)*}P_{reco} \quad (7.1)$$

P_{vertex} is the probability that a random event contains a vertex in the muon spectrometer; therefore, the first term in equation 7.1 is the expected number of background events which had one vertex and will randomly contain a second vertex. P_{reco} is the probability to reconstruct a vertex given there was an RoI cluster trigger; thus, the second term of equation 7.1 is the expected number of events which had two RoI clusters, that will have two vertices in the spectrometer.

To measure P_{vertex}, a random sample of events, from the Zero Bias stream[2], was used and the fraction of events that contained a vertex is 2/2055062 = $(9.7\pm6.9)\times10^{-7}$. The number of events that passed the RoI cluster with two acceptable clusters and have a reconstructed vertex, 1, is counted from the data. The probability to reconstruct a vertex in events that pass the RoI cluster trigger is calculated from data to be the fraction of triggered events that have a reconstructed vertex, $15543/(1.3571\times10^{6}) = (1.11\pm0.01)\times10^{-2}$. It should be noted that in calculating P_{reco}, all the found vertices are considered to be background, which will give a conservative estimate when calculating the expected background. The expected signal would contribute, at most, $\sim$100 events to the calculation of P_{reco} which would cause a relative change in P_{reco} of $\sim$1%. P_{reco} was also measured on data taken during the empty and unpaired bunch crossings, which provides a sample of events which are known to be non-collision backgrounds. On this sample of non-collision background events, P_{reco} was measured to be $(7.0\pm0.6)\times10^{-3}$. In calculating the background, the larger value of P_{reco} (1.11×10^{-2}) is taken, which provides a conservative estimate of the background. These numbers are summarized in Table 7.1. There is also a background from events with a punch-

Quantity	Number of Events	Value
N(MS vertex, 1 trig)	15543	15543
N(MS vertex, 2 trig)	1	1
P_{vertex}	2/2055062	$(9.7\pm6.9)\times10^{-7}$
P_{reco}	$15543/(1.3571\times10^{6})$	$(1.11\pm0.01)\times10^{-2}$

Table 7.1: The number of events and probabilities needed to compute the background to events having two vertices in the muon spectrometer.

through jet recoiling against the good MS vertex. This background can be calculated by removing the jet isolation criteria on the second vertex which measures how many punch-through jets with an associated vertex are in the signal sample. After removing this cut, there were no events with a non-isolated MS vertex in the sample of 15543 events that contain a good MS vertex. Therefore, at

[2]The Zero Bias stream contains events selected at random by a dedicated Level 1 trigger, which provides an unbiased sample of events.

the 95% CL, 3 events contain a vertex originating from a punch-through jet. This number is then multiplied by the probability a vertex from a punch-through jet will be isolated (see Section 6.6, which yields an expected number of background events, at the 95% CL, of $\sim 1 \times 10^{-4}$. Thus, the expected background is taken from equation 7.1, and is calculated to be 0.03 ± 0.02.

7.2.3 Systematic Uncertainties

The analysis is a cut based counting experiment, as a result all systematic uncertainties are on the normalization of the number of events. The Higgs production cross sections and uncertainties [26] are: $\sigma(m_{h^0}=120\ \text{GeV}) = 16.6^{+3.3}_{-2.5}$ pb and $\sigma(m_{h^0}=140\ \text{GeV}) = 12.1^{+2.3}_{-1.8}$ pb. Event selection requires the muon RoI cluster trigger, which has a systematic uncertainty of 14% as discussed in Section 5.1.6. The MS vertex requirement has a systematic uncertainty of 16% per vertex, see Section 6.6. The systematic uncertainties are summarized in Table 7.2.

Quantity	Systematic uncertainty
Higgs cross section	
m_{h^0} = 140 GeV	+18.8% -14.9%
m_{h^0} = 120 GeV	+19.7% -15.1%
RoI cluster trigger	14%
MS vertex (per vertex)	16%
Luminosity	3.7%

Table 7.2: List of the systematic uncertainties.

7.2.4 Results and Limits

Given that no excess over background is observed, exclusion limits are set for $\sigma \times \text{BR}(h^0 \to \pi_v \pi_v)$ by rejecting the signal hypothesis at the 95% confidence level applying the Markov Chain MC (MCMC) procedure [63]. Table 7.3 summarizes the number of events observed in data and the expected background for the two muon vertex analysis. Figure 7.2 shows the total number of expected

events for each of the Monte Carlo samples as a function of the π_v proper lifetime.

Analysis	Expected Background	Measured Number
MS vertex	0.03±0.02	0

Table 7.3: Expected number of background events and measured number of events for the two muon vertex channel. The expected background uncertainty contains the full systematic uncertainties.

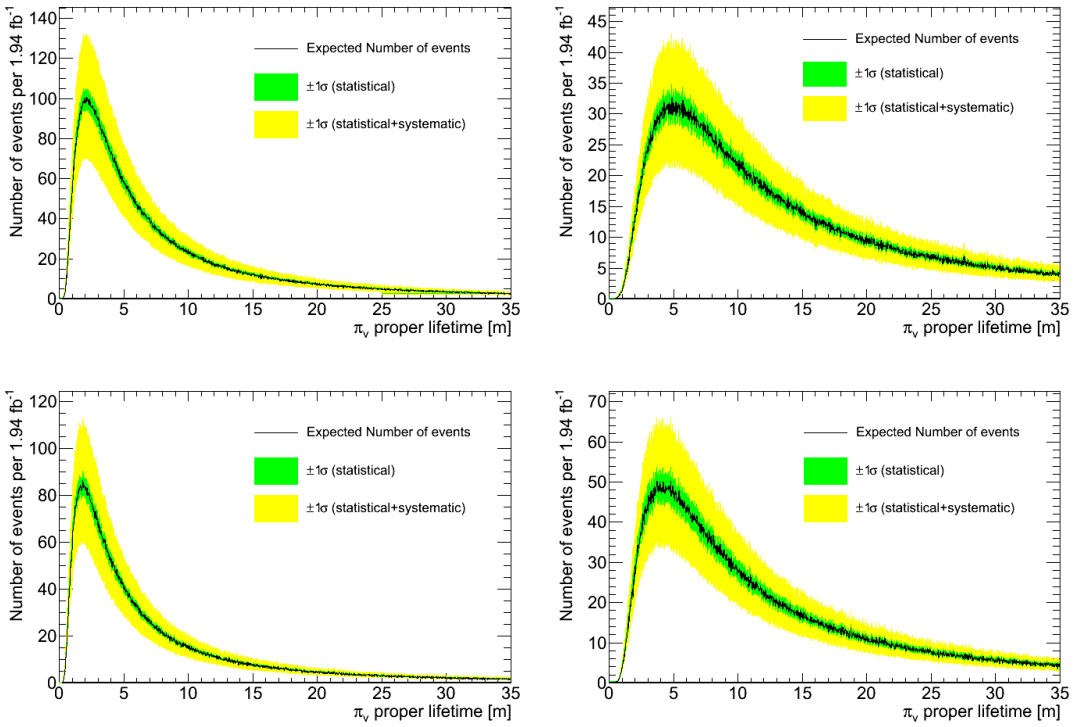

Figure 7.2: Expected yields for a two-object analysis for each of the four models. Each curve shows the number of events as a function of the π_v's proper lifetime where both π_v's are reconstructed as MS vertices. Top Left: m_h = 120 GeV, m_{π_v} = 20 GeV, Top Right: m_h = 120 GeV, m_{π_v} = 40 GeV, Bottom Left: m_h = 140 GeV, m_{π_v} = 20 GeV, Bottom Right:m_h = 140 GeV, m_{π_v} = 40 GeV

The MCMC procedure is run to calculate the 95% credible upper limit at each π_v proper lifetime

for the four Monte Carlo samples. The result is shown in Figure 7.3. The expected limits are the same as the observed limits in this case because the expected background is less than 1, therefore the 95% CL on the background is 3 for both the expected and observed limit. The dashed horizontal line represents 100% branching fraction for the decay mode, $h^0 \rightarrow \pi_v\pi_v$, and any proper lifetime below this line can be excluded at the 95% CL. As can be seen, for each of the signal samples studied, a wide range of π_v lifetimes can be excluded, assuming 100% branching fraction.

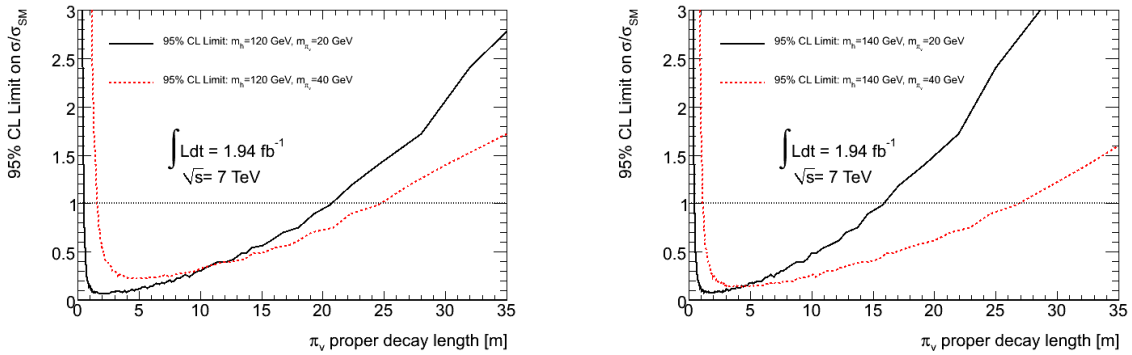

Figure 7.3: The observed limits for the search for $h^0 \rightarrow \pi_v\pi_v$. The dashed horizontal line represents the 100% branching fraction for this decay channel. Left: Limits for m_{h^0} = 120 GeV. Right: Limits for m_{h^0} = 140 GeV

7.3 Events that have a Jet with No Reconstructed Tracks

In the absence of specialized track reconstruction in the inner detector, which is able to reconstruct tracks originating far from the IP, the main signature of displaced decays occurring beyond the pixel tracker is jets with no reconstructed tracks (JNRT). For the purposes of this analysis, the term "reconstructed track" refers to a track with p$T > 1$ GeV that has at least one hit in the pixel detector and two hits in the SCT associated to it. The jets are required to be in the barrel, $\mid \eta \mid < 1$, and have $p_{\mathrm{T}} > 30$ GeV. Using this definition of a track, π_v's that decay beyond the pixel detector will not have any reconstructed tracks. Figure 7.4 shows the efficiency for reconstructing jets with no tracks as a function of the π_v decay position.

The probability that a π_v will produce a jet with no reconstructed tracks increases as the π_v decays closer to the calorimeter face, R=1.1 m, because the decay products from the π_v begin to merge and

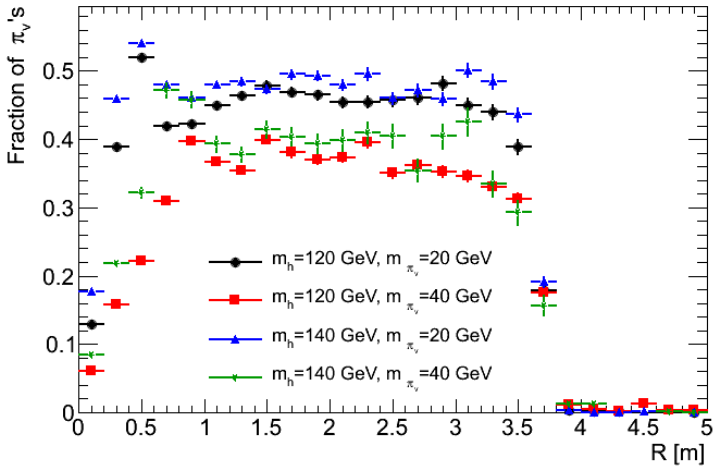

Figure 7.4: Fraction of π_v's that produce a jet with $\mid \eta \mid < 1$ and zero reconstructed tracks as a function of the π_v radial decay position.

form a single, more energetic jet as the π_v approaches the calorimeter. Once the π_v has entered the calorimeter, the probability it produces a jet with no tracks is roughly constant until the decay occurs toward the end of the hadronic calorimeter, R=4m, when there is no longer enough calorimeter volume to accurately measure the jet energy.

7.3.1 Event Selection

There is no dedicated trigger algorithm that selects jets with no reconstructed tracks, therefore events are required to pass the RoI Cluster trigger and subsequently contain a vertex in the spectrometer. The jet with no reconstructed tracks is required to be recoiling against the spectrometer vertex. In searching for this decay configuration, a missing energy (MET) requirement is added to the good vertex criteria. In signal events, one π_v has escaped the calorimeter volume, thus leaving no energy in the calorimeter and the second π_v has decayed before the end of the hadronic calorimeter. Therefore, missing energy is expected to point in the direction of the π_v which has decayed in the MS. Figure 7.5 shows the total missing energy in this type of signal event (Left) and the $\Delta\phi$ between the MET and the MS vertex (Right). By requiring missing energy of at least 20 GeV to be aligned with the MS vertex, within $\Delta\phi \leq 1$, the signal can be selected with high efficiency while the background

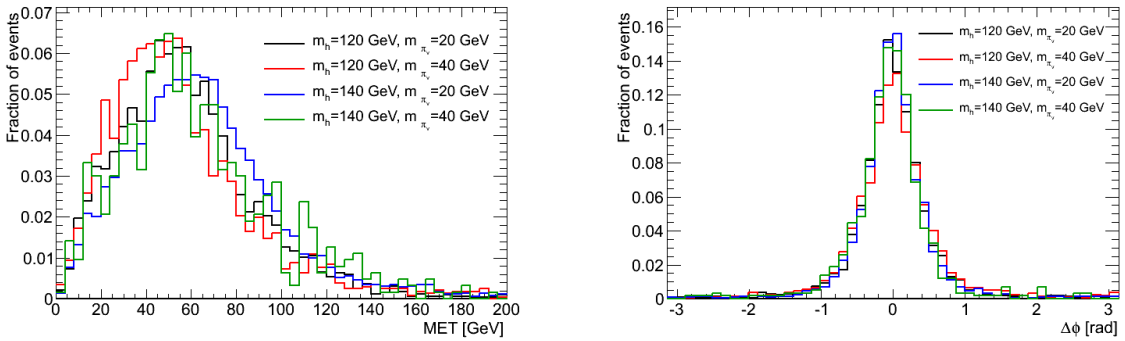

Figure 7.5: Left: Total missing energy in MC signal events with one π_v decay occurring inside the barrel muon spectrometer and the second π_v decay occurring before the end of the hadronic calorimeter. Right: $\Delta\phi$ between the MET direction and the reconstructed MS vertex position.

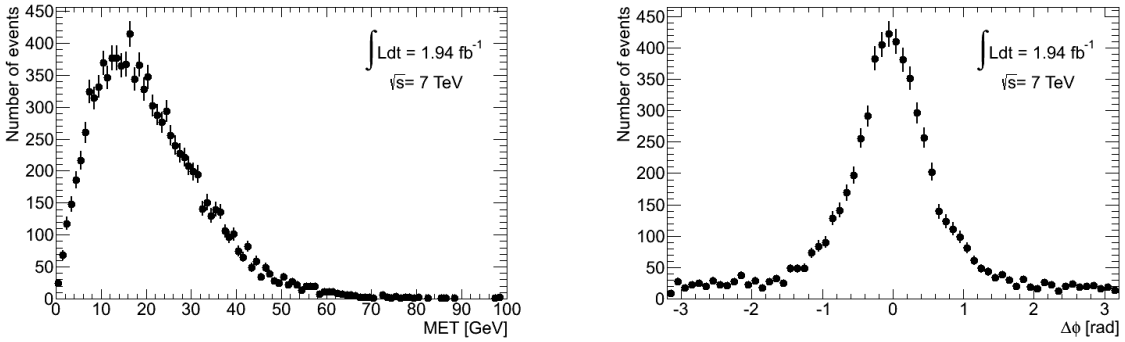

Figure 7.6: Left: The total missing energy in data events with a vertex in the barrel MS. Right: $\Delta\phi$ between the MET direction and the reconstructed MS vertex position.

is significantly reduced. Figure 7.6 shows the total missing energy (Left) and $\Delta\phi$ between the MET and the MS vertex in collision data.

After requiring 20 GeV of missing energy aligned with the MS vertex, the efficiency for reconstructing a good vertex in the MS is recomputed. The efficiency for reconstructing a good vertex with MET in the barrel for π_v's which pass the RoI cluster trigger is shown in Figure 7.7. The efficiency for reconstructing a vertex with the additional MET requirement is $\sim$90% the efficiency when the standard good vertex criteria is applied. The final event selection requires one good MS

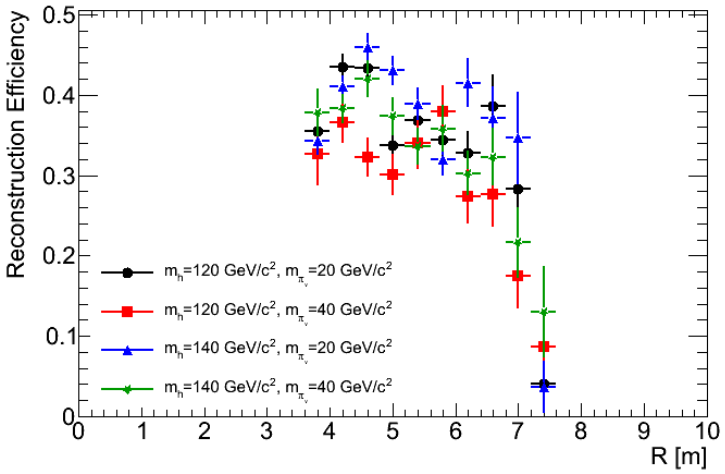

Figure 7.7: The efficiency to reconstruct a good MS vertex including the missing energy requirement for π_v's in the barrel ($\mid \eta \mid < 1$) region.

vertex separated by $\Delta R \geq 2$ from the jet with no reconstructed tracks.

7.3.2 Expected Background

The probability that a QCD jet has no reconstructed tracks is found using a tag and probe analysis. The tag-and-probe analysis selects events that have passed a single jet trigger. Using this trigger selection provides an unbiased sample of events which contain jets. Events are required to contain exactly two jets, with $p_{\mathrm{T}} \geq 20$ GeV and which pass the good jet criteria (Section 3.6), in the range $\mid \eta \mid \leq 2.5$ and have less than 20 GeV of missing energy. For jet pairs that pass this selection, one of the jets is randomly chosen to be the tag jet. The tag jet is further required to have at least 10% of the jet energy deposited in the EM calorimeter. This additional requirement on the tag jet ensures that jet originates at the IP and the event is consistent with QCD dijet production. The number of tracks, with $p_{\mathrm{T}} > 1$ GeV and at least one pixel and two SCT hits associated to the track is counted in the probe jet (the second jet in the event). Figure 7.8 shows the fraction of jets, as a function of jet p_{T}, that have no reconstructed tracks.

To measure the expected background, for every event with a vertex in the spectrometer, the

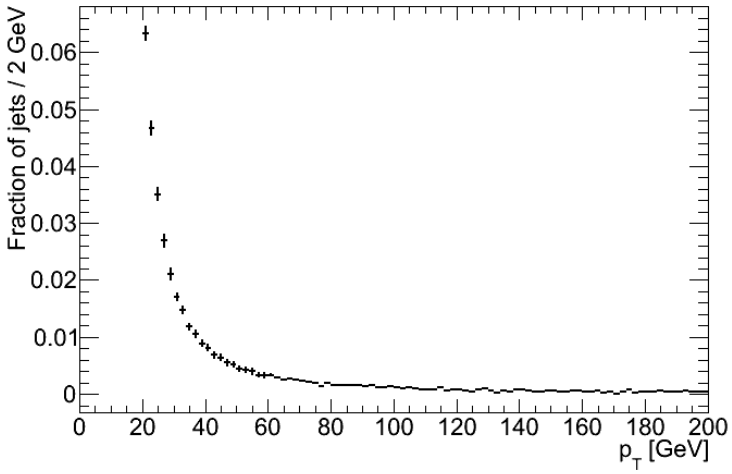

Figure 7.8: The probability that a QCD jet has no reconstructed tracks as a function of the jet p_{T}, for jets with $\mid \eta \mid < 1$.

probability that the event contain at least one jet with zero reconstructed tracks is computed. The probability that an event does not contain a jet with no tracks (P_{Event}(0 No Track)) can be computed as:

$$P_{Event}(0 \text{ No Track}) = \prod_{i=1}^{N_{jets}} (1 - P_{NoTracks}(p_T^{jet_i})) \tag{7.2}$$

Therefore, the probability an event contains at least one jet with no tracks is 1 - P_{Event}(0 No Track). The uncertainty on P_{Event}(0 No Track) is derived using the binomial variance.

$$\delta P_{Event}(0 \text{ No Track})^2 = \sum_{i=1}^{N_{jets}} (1 - P_{NoTracks}(p_T^{jet_i})) * P_{NoTracks}(p_T^{jet_i}) \tag{7.3}$$

This probability and uncertainty are then summed over all events that contain an isolated, good vertex in the spectrometer.

$$N_{Fake}(\text{JNRT, MS vertex}) = \sum_{Events} (1 - P_{Event}(0 \text{ No Track})) \tag{7.4}$$

$$\delta N_{Fake} = \sqrt{\sum_{Events} \delta P_{Event}(0 \text{ No Track})^2} \tag{7.5}$$

The probability for a QCD jet to be reconstructed with no tracks was cross-checked on a sample of events with a jet recoiling against a photon. These events are selected by triggering on the photon,

which provides an unbiased sample of recoil jets. The events are required to have only a single photon and a single jet, each with $p_{\mathrm{T}} \geq 20$ GeV, in the region $|\eta| \leq 2.5$ and have less than 20 GeV of missing energy. For each event, the probability that the jet will have no tracks is computed and the total number of events that contain a jet with no reconstructed tracks are counted. The ratio of the measured number of events containing no reconstructed tracks is compared to the expected number for each run[3], Figure 7.9. The ratio is fit to a straight line, which yields a constant of 0.93 ± 0.03. The systematic uncertainty on the probability for a jet to be reconstructed with no tracks is taken to be the difference from one, 7%.

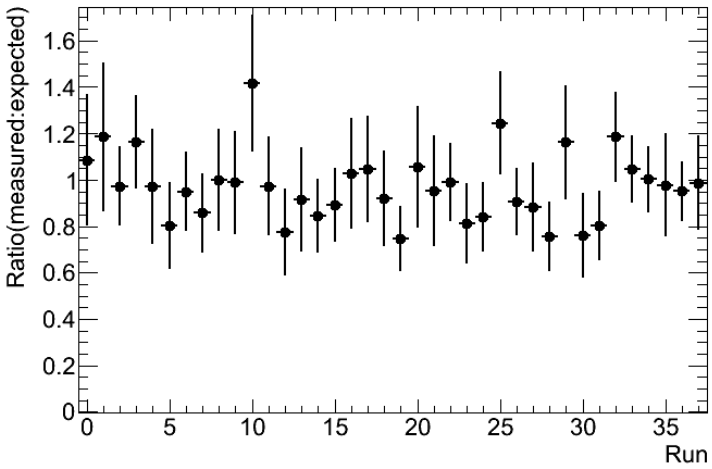

Figure 7.9: The ratio of the number of measured to expected events containing a jet with no reconstructed jets for the photon plus jet control sample, as a function of the run number.

Using this procedure, the expected number of background events, containing a jet with no reconstructed tracks and vertex in the spectrometer is $3.9 \pm 2.3(\mathrm{stat}) \pm 0.3(\mathrm{syst})$.

Another source of background events is due to beam halo[4]. In beam halo events, a proton has struck a collimator upstream from the detector. This creates a spray of low momentum particles

[3]Each LHC fill is referred to as a *run*.

[4]See Section 5.2.5

which can traverse the MS and high energy muons. If the high energy muon enters the calorimeter, it can bremsstrahlung inside the calorimeter, which fakes a jet. The particles that enter the MS can, depending on their configuration, be reconstructed as a vertex. These events can be separated into two distinct sources of background, based upon which calorimeter the high energy muon traverses: the hadronic or electromagnetic calorimeter.

If the muon enters the hadronic calorimeter, then these events can be identified using the techniques described in Section 5.2.5. Using these techniques to remove the beam halo events, the residual number of events is 11200$\pm$2500. The vertex routine is then run on a sample of events known to contain a jet from a beam halo muon. This gives an efficiency to reconstruct a vertex in beam halo events of 35/623758 = 5.6×10^{-5}. Thus the expected background contribution from this event topology is 0.6$\pm$0.1 events.

In the case where the muon traverses the electromagnetic calorimeter, there are currently no techniques developed to identify the events; therefore, the contribution to the total background from this event topology cannot be estimated. However, due to the good jet criteria[5], which requires a jet to have at least 10% of it's energy in the hadronic calorimeter, this background is expected to be small.

Therefore the total background is expected to be 4.5$\pm$2.4(stat)$\pm$0.3(syst).

7.3.3 Systematic Uncertainties

The analysis is a cut based counting experiment, therefore all systematic uncertainties are on the normalization of the number of events. The Higgs production cross sections and uncertainties are: $\sigma(m_{h^0}$=120 GeV) = $16.6^{+3.3}_{-2.5}$ pb and $\sigma(m_{h^0}$=140 GeV) = $12.1^{+2.3}_{-1.8}$ pb. Event selection requires the muon RoI cluster trigger, which has a systematic uncertainty of 14% as discussed in Section 5.1.6. The MS vertex requirement has a systematic uncertainty of 16% per vertex, see Section 6.6. The systematic uncertainties are summarized in Table 7.4. Additional systematic uncertainties in MC

[5]See Section 3.6.1

Quantity	Systematic Uncertainty
Higgs Cross Section	
m_{h^0} = 140 GeV	+18.8% -14.9%
m_{h^0} = 120 GeV	+19.7% -15.1%
RoI Cluster Trigger	14%
MS Vertex	16%
Luminosity	3.7%
No Track Probability (Background only)	7%

Table 7.4: List of the systematic uncertainties.

events to produce a jet with no tracks due to the JES, pileup and ISR have not been included. Another source of potential systematic uncertainty is the dependence on the MET cut for both the signal events and the probability for a jet to have no tracks. Only the sources of systematic uncertainty listed in Table 7.4 have been considered in the analysis.

7.3.4 Results and Limits

Performing the analysis on 1.94 fb^{-1} of data, 5 events are found that pass the selection cuts, with an expected background of 4.5$\pm$2.4(stat)$\pm$0.3(syst). Therefore, given no significant excess over background is observed and limits are set on $\sigma_{h^0} \times \mathrm{BR}(h^0 \rightarrow \pi_v \pi_v)$ by rejecting the signal hypothesis at the 95% credible level applying the Markov Chain MC procedure. Figure 7.10 shows the mean number of signal events expected to contain a both a vertex in the spectrometer and jet with no reconstructed tracks as a function of the π_v proper lifetime. The MCMC procedure is run to calculate the 95% credible upper limit at each π_v proper lifetime for the four Monte Carlo samples. The result is shown in Figure 7.11. A wide range of π_v lifetimes can be excluded assuming 100% branching ratio for $h^0 \rightarrow \pi_v \pi_v$; however, this event topology does not have comparable sensitivity to very long-lived ($c\tau \gtrsim 20$ m) because the analysis is restricted to $|\eta| < 1$ for both π_v's. Instead, in the case of the two MS vertex search, only one of the π_v's is required to be in the barrel ($|\eta| < 1$)

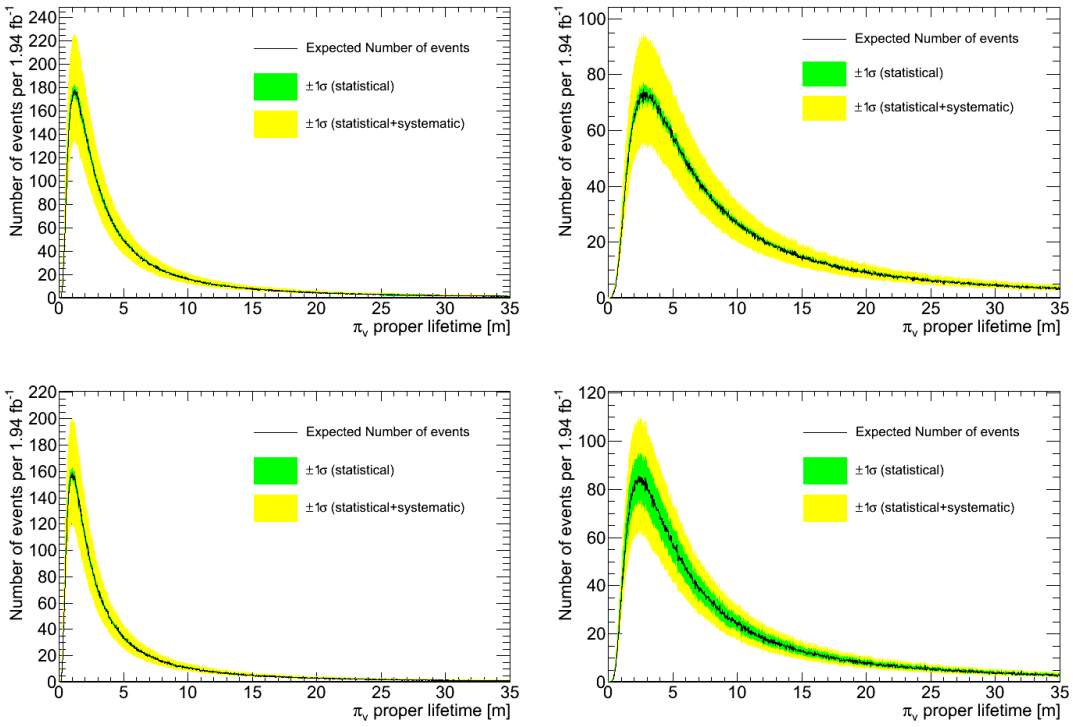

Figure 7.10: Expected yields for a two-object analysis for each of the four models. Each curve shows the number of events as a function of the π_v's proper lifetime where one π_v is reconstructed as an MS vertex and the second π_v is reconstructed as jet with no reconstructed tracks. Top Left: m_h = 120 GeV, m_{π_v} = 20 GeV, Top Right: m_h = 120 GeV, m_{π_v} = 40 GeV, Bottom Left: m_h = 140 GeV, m_{π_v} = 20 GeV, Bottom Right:m_h = 140 GeV, m_{π_v} = 40 GeV

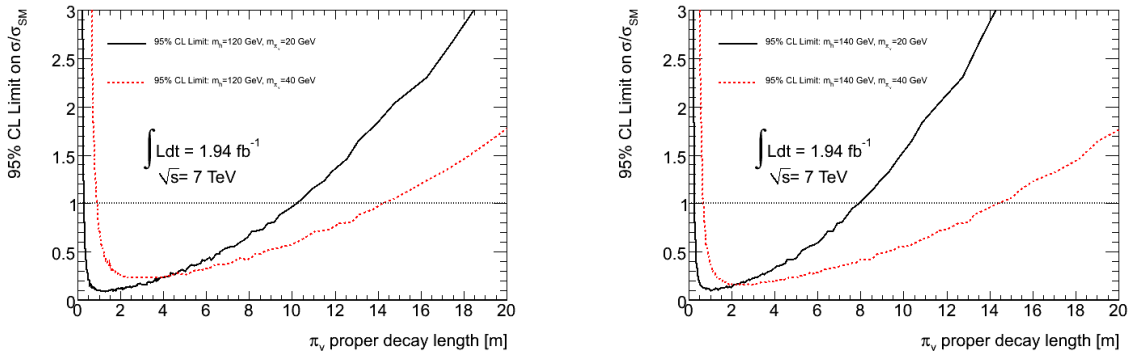

Figure 7.11: The observed limits for the search for $h^0 \rightarrow \pi_v\pi_v$. The dashed horizontal line represents the 100% branching fraction for this decay channel. Left: Limits for m_{h^0} = 120 GeV. Right: Limits for m_{h^0} = 140 GeV

Chapter 8

RESULTS AND CONCLUSION

A search has been performed for a pair of long-lived, weakly-interacting particles which decay to jet pairs far from the interaction point. Using the ATLAS detector, the search was performed for two event topologies: both particles decaying inside the volume of the ATLAS muon spectrometer and one particle decaying inside the muon spectrometer with the second particle decaying before the end of the hadronic calorimeter. The results of both searches are consistent with the background only prediction and limits were set using a model of the Higgs boson decaying to two long-lived, weakly-interacting pseudoscalars. Figure 8.1 shows the limits which are set on the pseudoscalar proper decay length. Table 8.1 shows the broad range of proper decay lengths which are excluded at

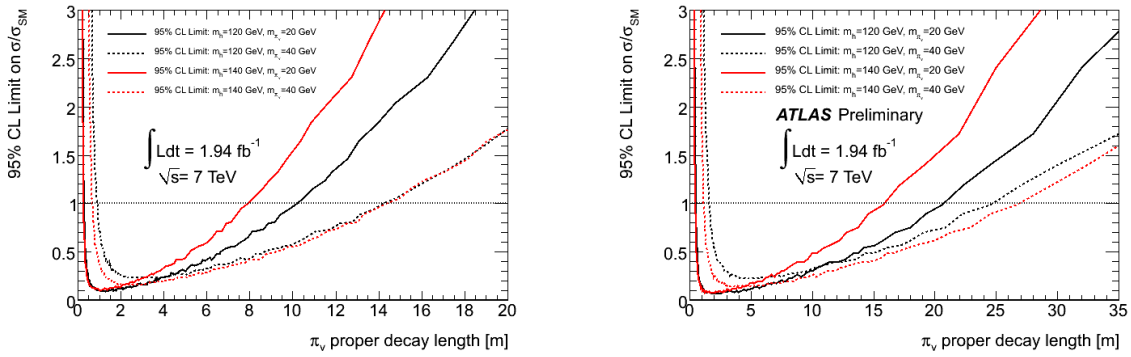

Figure 8.1: The observed limits for the search for $h^0 \rightarrow \pi_v\pi_v$. The dashed horizontal line represents 100% branching ratio for this decay channel. Left: The search for a vertex in the MS plus a jet with no reconstructed tracks. Right: The search for two vertices in the muon spectrometer.

the 95% CL assuming 100% branching ratio for the decay channel $h^0 \rightarrow \pi_v\pi_v$. The upper limits on the π_v proper lifetime are derived from the search for two vertices in the MS while the lower limits are from the search for a vertex in the MS plus a jet with no reconstructed tracks. Combined, these analyses are able to exclude π_v proper lifetimes from a few tens of centimeters to $\sim$20 meters.

m_{h^0} (GeV)	m_{π_v} (GeV)	Excluded Region
120	20	0.25 m $< c\tau <$ 20.65 m
120	40	0.90 m $< c\tau <$ 24.65 m
140	20	0.25 m $< c\tau <$ 15.8 m
140	40	0.65 m $< c\tau <$ 26.75 m

Table 8.1: The excluded proper decay lengths ($c\tau$), at 95% CL, of the π_v for each of the signal samples, assuming 100% branching ratio for the channel $h^0 \rightarrow \pi_v\pi_v$.

In addition to setting limits on the π_v proper lifetime in the context of the Higgs model, general limits can be placed on the maximum allowed cross section for these event topologies. Because no excess of events was seen, a 95% confidence-level upper limit of 8.3 fb is placed on the cross section times trigger efficiency times reconstruction efficiency times detector acceptance for events with a vertex in the muon spectrometer recoiling against a jet with no reconstructed tracks. For events with two vertices reconstructed in the muon spectrometer, a 95% confidence-level upper limit of 3.6 fb is placed on the cross section times trigger efficiency times reconstruction efficiency times detector acceptance. These cross section limits are valid for any model predicting long-lived, weakly-interacting particles.

BIBLIOGRAPHY

[1] G. Alteralli, hep-ph/0204179 (2002).

[2] M. Mangano, Phys.-Usp. **53** 109 (2010).

[3] K. Nakamura et al. (Particle Data Group), J. Phys. G **37** 075021 (2010).

[4] M. E. Peskin and D. V. Schroeder, *An Introduction to Quantum Field Theory*, (1995).

[5] D. Griffiths, *Introduction to Elementary Particles*, (1987).

[6] V. A. Rubakov, in *Proceeding from the 2008 European School of High-Energy Physics*, edited by N. Ellis and R. Fleischer (2010).

[7] F. Englert and R. Brout, Phys. Rev. Lett. **13**, 321 (1964).

[8] P. Higgs, Phys. Lett. **12**, 132 (1964).

[9] C. H. G.S. Guralnik and T. Kibble, Phys. Rev. Lett. **13**, 585 (1964).

[10] The LEP Higgs Working Group, hep-ex/0107034 (2001).

[11] The D0 Collaboration, D0 Note 6229-CONF (2011).

[12] The CDF Collaboration, CDF Note 10609 (2011).

[13] The ATLAS Collaboration, ATLAS-CONF-2011-163 (2011).

[14] The CMS Collaboration, CMS-PAS-HIG-11-032 (2011).

[15] A. D. Martin, et al., Eur. Phys. J. C **63**, 189 (2009).

[16] H. L. Lai, et al., Phys. Rev. D **82**, 074024 (2010).

[17] S. Dimopoulos et al., Phys.Rev.Lett. **76**, 3494 (1996).

[18] R. Barbier et al., Phys. Rept. **420**, 1 (2005).

[19] D. Tucker-Smith and N. Weiner, Phys. Rev. D **64**, 043502 (2001).

[20] M. J. Strassler and K. M. Zurek, Phys. Lett. B 651 374 (2007).

[21] M. J. Strassler and K. M. Zurek, Phys. Lett. B 661 263 (2008).

[22] M. J. Strassler, arXiv:hep-ph/0607160.

[23] ALEPH and DELPHI and L3 and OPAL and SLD and LEP Electroweak Working Group and SLD Electroweak Group and SLD Heavy Flavour Group Collaborations, Phys. Rept. **427**, 257 (2006).

[24] S. Chang, et al., Ann. Rev. Nucl. Part. Sci. **58**, 75 (2008).

[25] S. Chang, P.J. Fox and N. Weiner, JHEP 0608 068 (2006).

[26] LHC Higgs Cross Section Working Group, S. Dittmaier, C. Mariotti, G. Passarino, and R. Tanaka (Eds.), *Handbook of LHC Higgs Cross Sections: 1. Inclusive Observables*, CERN-2011-002 (CERN, Geneva, 2011), `arXiv:1101.0593 [hep-ph]`.

[27] L. Evans and P. Bryant, JINST **3** S08001.

[28] O. Bruning, et al., *LHC Design Report*, (2004).

[29] L. Evans, Annu. Rev. Nucl. Part. Sci. **61** 435 (2011).

[30] The ATLAS Collaboration, *ATLAS detector and physics performance: Technical Design Report*, (1999).

[31] The ATLAS Collaboration, JINST **3** S08003.

[32] T. Cornelissen et. al., ATL-SOFT-PUB-2007-007, (2007).

[33] The ATLAS Collaboration, arXiv:0901.0512 (2008).

[34] P.V.C. Hough, in *Proceedings from 2nd International Conference on High-Energy Accelerators (HEACC 59)*, (1959).

[35] The ATLAS Collaboration, ATLAS-CONF-2010-069, (2010).

[36] R. Fruhwirth, W. Waltenberger and P. Vanlaer, J. Phys. G **34**, N343 (2007).

[37] The ATLAS Collaboration, ATLAS-CONF-2010-005, (2010).

[38] The ATLAS Collaboration, ATLAS-CONF-2010-077, (2010).

[39] The ATLAS Collaboration, ATLAS-CONF-2010-073, (2010).

[40] The ATLAS Collaboration, ATLAS-CONF-2010-015, (2010).

[41] The ATLAS Collaboration, ATLAS-CONF-2010-001, (2010).

[42] The ATLAS Collaboration, ATLAS-CONF-2010-016, (2010).

[43] M. Cacciari, et al., JHEP **04**, 063 (2008).

[44] The ATLAS Collaboration, ATLAS-CONF-2010-038, (2010).

[45] The ATLAS Collaboration, ATLAS-CONF-2010-012, (2010).

[46] The ATLAS Collaboration, ATLAS-CONF-2010-059, (2010).

[47] The ATLAS Collaboration, ATLAS-CONF-2010-040, (2010).

[48] The ATLAS Collaboration, ATLAS-CONF-2011-116, (2011).

[49] The ATLAS Collaboration, Eur. Phys. J. C**71**, 1630 (2011).

[50] S. van der Meer, CERN-ISR-PO-68-31, (1968).

[51] S. M. T. Sjostrand and P. Z. Skands, JHEP **05**, 026 (2006).

[52] S. Agostinelli et al., Nuclear Instruments and Methods, 506 250 (2003).

[53] The ATLAS Collaboration, ATL-PHYS-PUB-2009-082, (2009).

[54] C. Adorisio et al., Nucl. Inst. and Meth. A593 400 (2008).

[55] The ATLAS Collaboration, ATLAS-CONF-2010-094, (2010).

[56] The ATLAS Collaboration, ATLAS-CONF-2011-031, (2010)

[57] D. de Florian, et al., arXiv:1109.2109

[58] ATLAS Muon Collaboration, ATLAS Muon Spectrometer Technical Design Report, CERN/LHCC/96-40, 1997.

[59] The ATLAS Collaboration, ATL-PHYS-PUB-2009-082, (2009).

[60] D. Adams,K. Assamagan, et al, ATL-SOFT-2003-007, (2003).

[61] S. Hassani et al., Nuclear Instrumentation and Methods A572 77 (2007).

[62] M. Woudstra, CERN-THESIS-2003-015 (2003).

[63] Tools used for limit setting: HistFactory from ROOT version 5.29 and the MCMC limit calculator from ATLAS StatForum
https://svnweb.cern.ch/trac/atlasgrp/browser/Physics/StatForum/RooStatsTools.

VITA

Daniel Ventura was born in San Diego, California, in 1980. He graduated from Escondido High School in 1999, after which he attended Palomar Junior College for two years and then transferred to the University of California, San Diego, where he earned a Bachelor of Science in Physics in 2005. After receiving a Masters of Science from the University of Washington, Seattle, in 2007 he moved to Geneva, Switzerland and joined the ATLAS experiment at CERN. Based on his research, in 2012, Daniel earned his Doctor of Philosophy at the University of Washington in Physics. He looks forward to continuing his research in high-energy physics as a member of the ATLAS Collaboration.